ABSTRACT

Title of Dissertation: NON-LOCAL TRANSPORT SIGNATURES AND QUALITY FACTORS IN THE REALISTIC MAJORANA NANOWIRE

Yi-Hua Lai
Doctor of Philosophy, 2022

Dissertation Directed by: Professor Jay Deep Sau
Department of Physics

Majorana zero modes (MZMs) can be fault-tolerant topological qubits due to their topological protection property and non-Abelian statistics. Over the last two decades, a deluge of theoretical predictions and experimental observations has been actively ongoing in the hope of implementing topological quantum computation upon MZMs. Among several solid-state systems, the most promising platform to realize MZMs is the one-dimensional semiconductor-superconductor nanowire (called "Majorana nanowire" in short), which is the focused system in this thesis. It is fundamental to identify MZMs as qubits to construct topological quantum computers. Therefore, the signatures of MZMs become highly crucial for verification. However, the earlier theoretical works demonstrate that topologically-trivial Andreev bound states (ABSs) can mimic the hallmarks of MZMs in various aspects but do not carry topological properties. As a result, distinguishing MZMs from ABSs becomes significantly pivotal in the study of Majorana nanowire.

One of the signatures the author studied is the robustness of the quantized zero-bias con-

ductance peak (ZBCP) in the realistic Majorana nanowire. The importance of this signature becomes further enhanced, particularly after the 2018 Nature paper, which displayed the quantized Majorana conductance, got retracted. In Chapter 2, the proposed quality factors quantify the robustness of quantized ZBCPs. By comparing the numerical results between different scenarios, this study shows that the quality factor F can help distinguish topological MZMs from trivial subgap bound states in the low-temperature limit.

Another necessary signature of MZMs is the non-local correlation. In Chapter 3, the conductance correlation is demonstrated by modeling the comparing quantum-point-contact (QPC) conductance from each end. Both the pristine nanowire and the quantum-dot-hybrid-nanowire system are modeled and compared, which shows the significance of non-local end-to-end correlation for the existence of MZMs. The other approach to simultaneously examining the localization of states at both ends of the nanowire is through the Coulomb blockade (CB) measurement. The lack of sensitivity to the localized state at only one end makes the CB spectroscopy able to capture the non-local correlation feature of MZMs. However, CB transport in the Majorana nanowire is much more complicated to analyze than QPC transport because (a) Coulomb interaction is treated as equal to MZM physics without perturbation, and (b) there are many energy levels in the nanowire, which gives rise to an exponential complexity to solve the rate equations. In Chapter 4, a generalized version of Meir-Wingreen formula for the tunneling conductance of a two-terminal system is derived. This formula reduces the exponential complexity of the rate equations to as low as the linear complexity of QPC tunneling, thus allowing multiple energy levels to be included in the calculation. With dominant realistic effects in the model, the experimental features, such as the bright-dark-bright CB conductance pattern and decreasing oscillation conductance peak spacings (OCPSs) with the Zeeman field, will be simulated and explained the-

oretically.

In short, the theoretical methods proposed in this thesis, including the quality factors, non-local correlation ZBCPs, and CB spectroscopy, are intended to distinguish MZMs from other topologically-trivial bound states. Further investigations on the robustness of quantized conductance and non-local correlation analysis can clarify the ambiguous signals in the experiments and push the realization of topological quantum computation to the frontier.

NON-LOCAL TRANSPORT SIGNATURES AND QUALITY FACTORS IN THE REALISTIC MAJORANA NANOWIRE

by

Yi-Hua Lai

Dissertation submitted to the Faculty of the Graduate School of the
University of Maryland, College Park in partial fulfillment
of the requirements for the degree of
Doctor of Philosophy
2022

Advisory Committee:
Professor Jay D. Sau, Chair/Advisor
Professor Sankar Das Sarma, Co-Advisor
Professor Maissam Barkeshli
Professor Johnpierre Paglione
Professor John Cumings

Acknowledgments

The completion of my Ph.D. does not come easy. Therefore, I would like to express my gratitude to the people who helped me during my Ph.D. journey. First and foremost, I would like to thank my advisor, Professor Jay Deep Sau, for his guidance on my research and support on my career path. As a theoretical physicist who is very familiar with experiments, Prof. Sau can always reduce a complicated physics problem to a simple formalism through his physics intuition. I especially gained a lot of knowledge from his fruitful perspectives on condensed matter experiments and his magic numerical tricks that can always help me avoid potential numerical loopholes. Most importantly, I am indebted to Prof. Sau's patience with me. He is always amiable in answering my questions of different levels. I cannot accomplish my Ph.D. without his down-to-earth support.

I also owe gratitude to my co-advisor, Professor Sankar Das Sarma, who always gives me clever suggestions for critical problems. Prof. Das Sarma has a unique and sharp taste for selecting important problems in condensed matter physics. I always get some physics insights through working with him on joint projects or watching him ask crucial questions to seminar speakers. My learning progress benefited a lot from Prof. Das Sarma's input.

I want to thank Professors Maissam Barkeshli, Johnpierre Paglione, and John Cumings for making the time and effort to serve as my dissertation committee members.

I feel grateful to have plenty of physics discussions and career suggestions from many

CMTC postdoctoral researchers, including but not limited to Ching-Kai Chiu, Junhyun Lee, Yi-Ting Hsu, Yang-Zhi Chou, Yunxiang Liao, Sheng-Jie Huang, and Yu-An Chen. They are always more than willing to share their physics knowledge and valuable experiences. I also feel thankful for the support I get from many past UMD senior students, including but not limited to Setiawan, Hoi-Yin Hui, Chun-Xiao Liu, Amit Nag, Yingyi Huang, Yidan Wang, Chiao-Hsuan Wang, Wan-Ting Liao, and I-Lin Liu. They are always more than happy to follow up with my status in my Ph.D. and give me practical advice accordingly.

My time at the University of Maryland would not be well-rounded without the accompany of my Ph.D. peers, including but not limited to Haining Pan, Huan-Kuang Wu, Tomoghna Barik, DinhDuy Vu, Donovan Buterakos, Subhayan Sahu, Naren Manjunath, Ali Lavasani, Shuyang Wang, Yong-Chan Yoo, Stuart Thomas, and Navya Gupta from CMTC. I especially thank Haining Pan and Huan-Kuang Wu for their extra non-physics interactions to help me conquer various obstacles in my life. I also cherish those fun days with Wen-Chen Lin, Peiyin Lee, Sun-Ting Tsai, Su-Kuan Chu, Tung-An Wei, Tamin Tai, Jwo-Sy Chen, Chien-Ming Huang, Chih-Yu Lee, Lauren Lan, Yue Tsao, Chen-Yu Chen, Eugene Yang, and many others. They all give me some wisdom in my life in different ways.

I am particularly indebted to my lifelong mentor, Professor Ite A. Yu, from my alma mater, National Tsing Hua University. He has supported my Ph.D. studies virtually since I obtained my master's degree under his guidance. Specifically, I want to thank him for writing recommendation letters for my postdoctoral applications and accomodating the deadlines for me without any hesitation. Whenever I visited him in Taiwan, I could still feel his lasting passion for physics, smartness in tackling problems, wisdom towards life, and kindness to all the people. The model he has set always motivates me to become a better person. I feel lucky and grateful that Prof. Yu

gave me many opportunities, encouraged me, and supported my career path.

Last but not least, I want to thank my parents, my sister, and my husband, who have been supporting me throughout my Ph.D. years. Particularly, I owe most to my husband, Farhan Augustine, who always supported me and encouraged me to stay positive when I was in the valleys of my Ph.D. years. I cannot grow so much and feel fulfilled during my Ph.D. journey without him accompanying me to pass through every delightful and stressful moment.

Table of Contents

List of Figures

List of Abbreviations

ABS	Andreev Bound state
BdG	Bogoliubov-de Gennes
BTK	Blonder Tinkham-Klapwijk
CB	Coulomb Blockade
DOS	Density of States
H.c.	Hermitian Conjugation
MF	Majorana Fermion
MBS	Majorana Bound State
MZM	Majorana Zero Mode
NS	Normal Metal-Superconductor
OCPS	Oscillation Conductance Peak Spacing
QD	Quantum Dot
QPC	Quantum Point Contact
SC	Superconducting / Superconductor / Superconductivity
SM	Semiconducting / Semiconductor
SOC	Spin-Orbit Coupling / Spin-Orbit Coupled
TQC	Topological Quantum Computing
TQPT	Topological Quantum Phase Transition
TSC	Topological Superconductor
ZBP	Zero-Bias Peak
ZBCP	Zero-Bias Conductance Peak

Chapter 1: **Introduction**

In 1937, the charge-neutral Majorana fermion, which is its own anti-particle, was proposed by Ettore Majorana as an elementary particle that stands as a real solution to the Dirac equation [1]. This notion has made an impact on several subfields of physics, such as high-energy physics and condensed matter physics. In high-energy physics, neutrino is the only candidate that could be a Majorana fermion. Unfortunately, Majorana fermions have not been detected through the conventional high-energy approach over the past 80 years. On the other hand, in condensed matter physics, several theoretical models that can host Majorana fermions have been attracting physicists' attention over the last 20 years. It is not only because of the likelihood to discover this elementary particle but also because of the potential to construct the non-Abelian topological quantum computer based on Majorana fermions' unique properties [2–15]. Since Majorana fermions in solid-state systems appear as zero-energy quasi-particle excitations that are bound to defects [16] and are not fermions, they are often dubbed as "Majorana zero modes" (MZMs) or "Majorana bound states" (MBSs).

Earlier works for MZMs in condensed matter physics focus on fractional quantum Hall states [17–19], and p-wave superconductors [2, 19–24] that can support the existence of MZMs either at the ends of one-dimensional topological superconductors [2] or at the vortices of two-dimensional topological superconductors [19, 23]. An esssential component of these proposed

systems is the exotic p-wave superconducting pairing potential, which is quite scarce in the nature. Therefore, the experimental progress of these exotic systems is slow-paced.

Around 2010, the idea of heterastructure enabled scientists to adapt devices proximitized by the conventional s-wave superconductor to topological superconductors [25–30]. These experimentally applicable proposals brought a new phase to the field of Majorana fermions in condensed matter physics. A significant amount of groundbreaking experiments have been carried out in the past 10 years [31–52]. Among these proposals, the most promising candidate is the spin-orbit-coupled semiconducting nanowire proximitized by an s-wave superconductor with an external magnetic field parallel to the axis of the nanowire [26–29]. We call it "Majorana nanowire" in short. This system can be tuned into the topological regime, where the MZMs are supposed to appear at both ends of the nanowire, simply by increasing the magnetic field strength to be above the topological quantum phase transition (TQPT) field. One of the most essential features of the MZMs is the zero-bias conductance peak (ZBCP) quantized at $2e^2/h$ at zero temperature, which can be explained by the perfect Andreev reflection facilitated by MZMs [53–57]. While several quantized ZBCPs were observed in several experiments [38, 44, 52], the existence of MZMs remains elusive because topologically-trivial Andreev bound states (ABSs) or disorder-induced bound states can exhibit quantized ZBCPs similar to the ones from MZMs [58–69]. In fact, topologically-trivial subgap bound states can mimic the signatures of MZMs in various way, making MZMs hard to be distinguished.

In this thesis, we aim to distinguish between the topological MZMs and trivial subgap bound states by using various signatures of MZMs. The approaches we use to identify MZMs include: (a) the quality factors to gauge the robustness of quantized ZBCPs [Chapter 2], (b) the non-local end-to-end conductance correlation [Chapter 3], and (c) the Coulomb blockade

spectroscopy [Chapter 4]. In each of the theoretical study, we analyze and simulate the one-dimensional Majorana nanowire with all the important realistic effects. The first two approaches provide experiments new directions to search for the elusive MZMs, while the last one explains the experimental results of the Coulomb blockaded nanowire. The conclusion of the above works will be provided in Chapter 5.

Before the reader jumps to our core contributed works [Chapter 2- Chapter 4], the author wants to give the reader a review in this chapter on the theoretical development and understanding of MZMs, the famous Kitaev chain model, the Majorana nanowire model, several characteristic signatures of MZMs, and the pioneering experiments related to our theoretical studies. This chapter should offer the research background for the reader to stay engaged with the problems the author tries to solve in the following chapters.

1.1 Majorana zero mode (MZM)

Majorana zero mode (MZM), the condensed-matter version of Majorana fermion, has been vigorously discussed recently mainly because of its special exchange statistics: They are non-Abelian anyons [70] that do not commute when particles exchanges, unlike bosons and fermions. MZMs are mixtures of electrons and holes in equal weight because MZMs are their own anti-particles. Since the Bogoliubov quasi-particles in superconductors can be represented as superpositions of electrons and holes, MZMs should be able to exist as zero-energy subgap bound states in superconductors. From the particle-hole symmetry of the Bogoliubov quasi-particle operators, which satisfy

$$\gamma^{\dagger}(\epsilon) = \gamma(-\epsilon), \tag{1.1}$$

the MZMs should appear at the Fermi energy (i.e., $\epsilon = 0$) such that the self-conjugate relation $\gamma^\dagger = \gamma$ is satisfied. Note that $\gamma^\dagger$ and γ are Majorana creation and annihilation operators that satisfy the following anti-commutation relation

$$\{\gamma_n, \gamma_m\} = 2\delta_{nm}. \tag{1.2}$$

Moreover, Majorana operators are required to commute with the Hamiltonian, i.e.,

$$[H, \gamma_n] = 0. \tag{1.3}$$

This relation suggests that there is ground-state degeneracy due to the presence of MZMs. It is because the ground state $|\text{GS}\rangle$ and the excited states $\gamma_i|\text{GS}\rangle$ correspond to the same energy. In general, a system that host $2N$ MZMs $\gamma_1, \gamma_2, \ldots . \gamma_{2N}$ has 2^N degenerate ground states. We can understand this further by writing the fermion operators c_i in terms of Majorana operators,

$$c_i = \frac{1}{2}\left(\gamma_{2i-1} + i\gamma_{2i}\right), \tag{1.4}$$

for $n = 1, \ldots, N$. Note that the fermion operators c_i satisfy the conventional fermionic anti-commutation relation:

$$\{c_i, c_j^\dagger\} = \delta_{ij}, \tag{1.5}$$

$$\{c_i, c_j\} = 0. \tag{1.6}$$

The fermionic number operator

$$n_i \equiv c_i^\dagger c_i = \frac{1}{2}\left(1 + i\gamma_{2i-1}\gamma_{2i}\right) \tag{1.7}$$

can take either 0 or 1, which means the degeneracy of the ground state is 2^N-fold for a system of N fermions. However, since the fermion parity is conserved for an isolated system, this constraint puts the physical degeneracy to be 2^{N-1}.

Eq. (1.4) also indicates one fermionic operator is composed of two MZMs. One can simply separate a fermionic operator into a real part and an imaginary part, and claim each part a MZM. However, it is just a mathemetical concept rather than a physical operation because the two MZMs close to each other spatially cannot be addressed individually. The MZMs we pay attention to here are from a delocalized fermionic operator that is composed of two spatially-separated MZMs. The fermionic state associated with this delocalized fermionic operator can be protected from most of decoherence because local perturbations that affect only one MZM component cannot change the whole state. On the other hand, the state can be manipulated by exchanging MZMs due to their non-Abelian statistics, which leads to the idea of fault-tolerant topological quantum computer [6].

1.1.1 Fermion Parity of the Ground State

As illustrated as above, there is two-fold degeneracy for the topological ground state, where the two MZMs are localized separately. One is unoccupied state

$$|0\rangle \equiv |\mathrm{GS}\rangle, \tag{1.8}$$

and the other is occupied state

$$|1\rangle \equiv \gamma_i|\text{GS}\rangle. \tag{1.9}$$

These two states can be characterized by the fermion parity. The fermion parity of site i with fermion number n_i is

$$P_i = (-1)^{n_i}. \tag{1.10}$$

Since $n_i = c_i^\dagger c_i$ in the language of operators,

$$\begin{aligned} (-1)^{n_i} &= 1 - 2n_i & (1.11)\\ &= -i\gamma_{2i-1}\gamma_{2i}. & (1.12) \end{aligned}$$

The fermion parity operator for the whole system can be thus defined as

$$\begin{aligned} P_F &= \prod_{i=1}^{N}\left(1 - 2c_i^\dagger c_i\right) & (1.13)\\ &= \prod_{i=1}^{N}\left(-i\gamma_{2i-1}\gamma_{2i}\right), & (1.14) \end{aligned}$$

with $(P_F)^2 = 1$. So its eigenvalues can only be ± 1. For the trivial phase, P_F is always $+1$ because $c_i|\text{GS}\rangle = 0$. For the topological phase, P_F can be either $+1$ or -1, as explained below.

In the ideal case of the Kitaev chain model [see Sec. 1.2], a pair of well-separated edge MZMs (γ_1 and γ_{2N}) can be defined as a non-local fermion,

$$\begin{aligned} f &= \frac{1}{2}\left(\gamma_1 + i\gamma_{2N}\right), & (1.15)\\ f^\dagger &= \frac{1}{2}\left(\gamma_1 - i\gamma_{2N}\right). & (1.16) \end{aligned}$$

Similar to the protocol of Eqs. (1.4)-(1.7), the eigenvalues of the fermion number operator can be 0 when the eigenstate is the unoccupied ground state $|0_+\rangle$, or 1 when the eigenstate is the occupied ground state $|0_-\rangle$. That is to say,

$$f^\dagger f|0_+\rangle = 0, \tag{1.17}$$

$$f^\dagger f|0_-\rangle = |0_-\rangle. \tag{1.18}$$

Moreover,

$$-i\gamma_1\gamma_{2N} = 1 - 2f^\dagger f. \tag{1.19}$$

On the other hand, the fermionic bulk states (in the ideal Kitaev chain model), which are composed of two MZMs next to each other, can be expressed as

$$d_i = \frac{1}{2}\left(\gamma_{2i} + i\gamma_{2i+1}\right), \tag{1.20}$$

$$d_i^\dagger = \frac{1}{2}\left(\gamma_{2i} - i\gamma_{2i+1}\right). \tag{1.21}$$

So similarly, $-i\gamma_{2i}\gamma_{2i+1} = 1 - 2d_i^\dagger d_i$. The fermion parity operator becomes

$$P_F = -i\gamma_1 \prod_{i=1}^{N-1}(-i\gamma_{2i}\gamma_{2i+1})\gamma_{2N} \tag{1.22}$$

$$= -i\gamma_1\gamma_{2N} \prod_{i=1}^{N-1}\left(1 - 2d_i^\dagger d_i\right). \tag{1.23}$$

Since the bulk states are in the trivial phase, $d_i|\text{GS}\rangle = 0$ and thus we have

$$P_F|\text{GS}\rangle = (-i\gamma_1\gamma_{2N})|\text{GS}\rangle. \tag{1.24}$$

By combining Eqs. (1.17)-(1.19) into Eq. (1.24), we can obtain

$$P_F|0_\pm\rangle = (-i\gamma_1\gamma_{2N})|0_\pm\rangle \tag{1.25}$$

$$= (1-2f^\dagger f)|0_\pm\rangle \tag{1.26}$$

$$= \pm|0_\pm\rangle. \tag{1.27}$$

Therefore, the ground states of the topological phase in the ideal Kitaev chain model [Fig. 1.1(b)] are 2-fold degenerate that can be categorized by the fermion parity. One can call the ground state $|0_+\rangle$ even-parity state, and the other state $|0_-\rangle$ odd-parity state.

1.2 1D Spinless p-wave Superconductor

We want to introduce the first condensed-matter model that can host unpaired MZMs in a one-dimensional system. In 2001, a toy model of a one-dimensional spinless p-wave superconductor was proposed by Alexei Y. Kitaev [2]. It is also typically named as "Kitaev Chain" model. The Hamiltonian is given by

$$H = -\mu\sum_{j=1}^{N}\left(c_j^\dagger c_j - \frac{1}{2}\right) - \sum_{j=1}^{N-1}\left(tc_j^\dagger c_{j+1} + \Delta_p e^{i\phi}c_j c_{j+1} + \text{H.c.}\right), \tag{1.28}$$

where μ is the chemical potential, $t \geq 0$ is the nearest-neighbor hopping, $\Delta_p e^{i\phi}$ is the p-wave superconducting gap, $c_j^\dagger$ and c_j are the electron creation and annihilation operators at site j. Note that H.c. means Hermitian conjugation.

The Hamiltonian in Eq. (1.28) can be expressed in terms of Majorana operators by canoni-

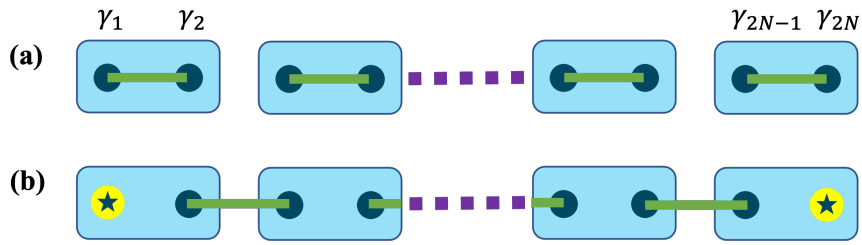

Figure 1.1: Schematic plots of the Kitaev chain with two distinct phases: The black dot represents the Majorana fermion, while the blue square represents the electron site. (a) Trivial phase: $\Delta_p = t = 0$ and $\mu < 0$. Two Majorana fermions from the same site are paired up. (b) Topological phase: $\Delta_p = t > 0$ and $\mu = 0$. Two Majorana fermions from different sites next to each other are paired up, leaving two isolated Majorana fermions (denoted by the star sign) at the ends.

cally transforming the electron creation and annihilation operators as follows:

$$c_j^\dagger = \frac{e^{i\phi/2}}{2}\left(\gamma_{2j-1} - i\gamma_{2j}\right), \tag{1.29}$$

$$c_j = \frac{e^{-i\phi/2}}{2}\left(\gamma_{2j-1} + i\gamma_{2j}\right), \tag{1.30}$$

where γ_{2j-1} and γ_{2j} are the Majorana operators at the j-th site. In this basis, the Hamiltonian becomes

$$H = \frac{i}{2}\sum_{j=1}^{N-1}\left[-\mu\gamma_{2j-1}\gamma_{2j} + (\Delta_p + t)\,\gamma_{2j}\gamma_{2j+1} + (\Delta_p - t)\,\gamma_{2j-1}\gamma_{2j+2}\right] \tag{1.31}$$

There are two interesting cases worth of discussion:

(a) The trivial phase: $\Delta_p = t = 0$ and $\mu < 0$. Then

$$H = -\mu\sum_{j=1}^{N}\left(c_j^\dagger c_j - \frac{1}{2}\right), \tag{1.32}$$

where the Majorana operators are paired up at the same lattice site [see Fig. 1.1(a)]. The

system is gapped by $2|\mu|$with no zero-energy state. So this phase is an insulator.

(b) $\Delta_p = t > 0$ and $\mu = 0$. In this case,

$$H = it \sum_{j=1}^{N-1} \gamma_{2j}\gamma_{2j+1}. \tag{1.33}$$

Now the Majorana operators γ_{2j} and γ_{2j+1} from different adjacent sites are paired up except for the Majorana operators at the ends [see Fig. 1.1(b)]. By writing the Majorana operators into new-defined fermion operator in the bulk, i.e., $\tilde{c}_j = (\gamma_{2j} + i\gamma_{2j+1})$, the Hamiltonian becomes

$$H = t \sum_{j=1}^{N-1} \left(\tilde{c}_j^\dagger \tilde{c}_j - \frac{1}{2} \right). \tag{1.34}$$

The ground states satisfy the condition $\tilde{c}_j|\text{GS}\rangle = 0$ for $j = 1, \ldots, (N-1)$. On the other hand, since the two unpaired Majorana modes at each end can form non-local fermionic states, the phase in this parameter regime is topological. The two degenerate ground states $|0_\pm\rangle$ composed of the two unpaired Majorana end modes also satisfy the fermion parity relations Eqs. (1.17)-(1.27).

As above, we analyzed the two distinct phases in two special parameter limits. Each phase has its own finite parameter space demarcated by SC gap-closure. Generally, the system represented by the two Hamiltonians are said to be in two distinct topological phases if these two Hamiltonians cannot be continuously deformed into each other without crossing a gap closure. Interestingly, both phases have the same bulk properties—the site index of Majorana operators just need to be shifted by 1 than the other. However, the edge properties of both phases are different. Clearly, phase (b) has unpaired Majoranas at both ends. So it is important for us to analyze

the parameter space where the bulk quasi-particle energy spectrum has bulk gap closing.

One can set a periodic boundary condition $c_{N+1} = c_1$ to the Kitaev Hamiltonian as in Eq. (1.28) to dig into the phase boundary further. Through the Fourier transformation, the Hamiltonian in momentum space can be expressed as

$$H = \sum_k \left[-2t\cos(k) - \mu\right] c_k^\dagger c_k + 2\Delta_p \left[i\sin(k) c_k c_{-k} + \text{H.c.}\right]. \tag{1.35}$$

In the form of BdG Hamiltonian H_{BdG} defined as

$$H = \frac{1}{2} \sum_{k \in BZ} C_k^\dagger H_{\text{BdG}}(k) C_k, \tag{1.36}$$

where $C_k^\dagger = \left[c_k^\dagger, c_{-k}\right]$, BdG Hamltonian is

$$H_{\text{BdG}}(k) = \begin{pmatrix} -2t\cos(k) - \mu & 2i\Delta_p^* \sin(k) \\ -2i\Delta_p \sin(k) & 2t\cos(k) + \mu \end{pmatrix}. \tag{1.37}$$

By diagonalizing H_{BdG}, the bulk energy spectrum is therefore

$$E(k) = \pm\sqrt{\left[2t\cos(k) + \mu\right]^2 + 4|\Delta_p|^2 \sin^2(k)}. \tag{1.38}$$

We can see the bulk gap closes at $\mu = -2t$ when $k = 0$, and at $\mu = 2t$ when $k = \pi$. For the regime where $|\mu| > 2t$, there will always be a bulk gap, which will never host MZMs. So for $|\mu| > 2t$, it is the topologically-trivial phase. In constrast, the regime $|\mu| < 2t$ is topologically-non-trivial such that MZMs can exist.

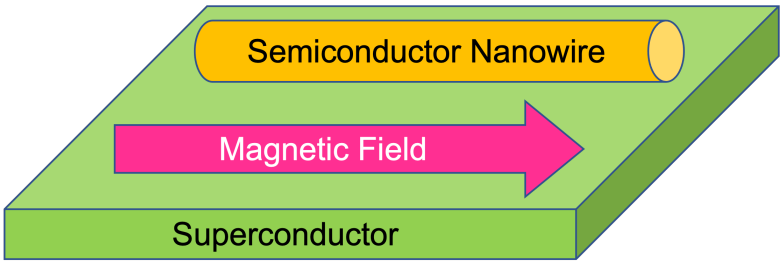

Figure 1.2: Schematic illustration of the 1D SOC semiconducting nanowire proximitized by the s-wave SC. The external magnetic field is applied parallel to the axis of the nanowire.

While this Kitaev chain model is theoretically simple, spinless p-wave SC actually does not exist in nature intrinsically due to the fact that electrons are spinful. Nevertheless, one can artificially remove the spin degree of freedom by lifting the Kramer's degeneracy of the electrons. With this idea, many theoretical models that can realize topological superconductor with s-wave SC in different types of heterostructures are proposed [25–30, 69, 71–79]. The most promising proposal to realize topological superconductor is the one-dimensional superconductor-semiconductor (SC-SM) hybrid nanowire, which will be discussed in the next section.

1.3 1D Superconductor-Semiconductor Nanowire

In 2010, a two-dimensional hybrid structure that can generate MZMs with only conventional SCs and SMs was propose by Sau *et al.* [26, 27] Later on, Lutchyn *et al.* [28] and Oreg *et al.* [29] proposed a one-dimensional spin-orbit-coupled (SOC) semiconducting nanowire proximitized by the s-wave SC in the presence of a magnetic field parallel to the axis of the nanowire [see Fig. 1.2]. Majority of the experimental groups working on solid-state systems to realize MZMs are using this heterostructure recently because the materials are easily accessible in the

lab. The Hamiltonian of this SC-SM nanowire is

$$H_{\text{NW}} = \frac{1}{2}\int dx \Psi^{\dagger}(x) H_{\text{BdG}}(x) \Psi(x), \tag{1.39}$$

$$H_{\text{BdG}} = \left(-\frac{\hbar^2}{2m^*}\partial_x^2 - i\alpha_R \partial_x \sigma_y - \mu\right)\tau_z + V_z\sigma_x + \Delta\tau_x, \tag{1.40}$$

where m^* is the effective electron mass, α_R is the SOC constant, μ is the chemical potential, $V_z = g\mu_B B$ is the spin-splitting Zeeman field due to magnetic field B applied perpendicular to SOC, and Δ is the proximity-induced s-wave SC gap. H_{BdG} is expressed in the basis of Nambu spinor $\Psi(x) = [c_\uparrow(x), c_\downarrow, c_\downarrow^\dagger(x), -c_\uparrow^\dagger(x)]^T$. $\sigma_{x,y,z}$ are spin Pauli matrices, and $\tau_{x,y,z}$ are particle-hole Pauli matrices.

One can understand the physics of this SOC semiconducting nanowire further by analytically solve the energy spectrum firstly in the limit where the proximitized SC gap is absent, i.e., setting $\Delta = 0$ in Eq. (1.40). The analytical energy solution will be

$$E_{\pm}(k_x) = \frac{\hbar^2 k_x^2}{2m^*} - \mu \pm \sqrt{V_z^2 + (\alpha_R k_x)^2}, \tag{1.41}$$

where $E_+(k_x)$ and $E_-(k_x)$ correspond to the upper band and lower band, respectively [see Fig. 1.3 (a)-(c)]. Firstly, at $V_z = 0$, the SOC term shifts the parabolic bands towards the positive and negative momentum directions depending on their spin polarization, as in Fig. 1.3(a). As soon as the Zeeman field is turned on, the band crossing at $k_x = 0$ turns into band anti-crossing, resulting a band gap opening, as in Fig. 1.3(b). If μ is set inside the gap, there is only one effective spin direction even though this direction depends on momentum. In this case, spinless SC can be induced by the proximity effect. Stronger magnetic field can increase the gap

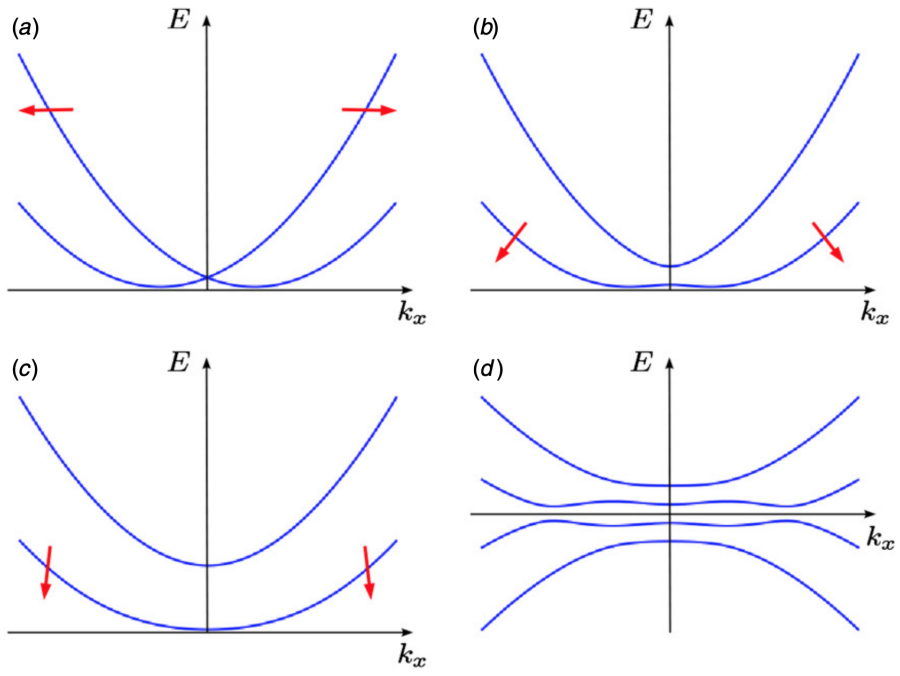

Figure 1.3: Energy spectrum $E(k_x)$ of the SOC semiconducting nanowire. The spin polarizations are denoted by the red arrows. (a) $\Delta = 0$ and $V_z = 0$. (b) $\Delta = 0$ and small $V_z > 0$. (c) $\Delta = 0$ and large $V_z > 0$. (d) $\Delta > 0$ and large $V_z > 0$. This figure is adapted from Ref. [80].

and make the spins aligned to the same direction such that the spin polarization is independent of momentum, as in Fig. 1.3(c). However, it will be hard for the SC-proximity effect to kick in because the SC pairing term only couples electrons with anti-parallel spins. Finally, if the s-wave SC gap is switched on, i.e., $\Delta > 0$, as in Fig. 1.3(d) the nanowire becomes topological. Focusing on the lower band and writing the Hamiltonian in the basis of the lower band, i.e., $\psi_-^\dagger(k_x)$ and $\psi_-(k_x)$, we can get the Hamiltonian describing the occupied band as [30]

$$H_{\text{occupied}} = \int dk_x \left[E_-(k_x)\psi_-^\dagger(k_x)\psi_-(k_x) + \Delta_-(k_x)\psi_-^\dagger(k_x)\psi_-^\dagger(-k_x) + \text{H.c.} \right], \tag{1.42}$$

where

$$\Delta_- = \frac{i\alpha_R k_x}{2\sqrt{V_z^2 + (\alpha_R k_x)^2}}\Delta \tag{1.43}$$

is p-wave symmetry. Here the inter-band pairing terms are ignored because Δ is assumed to be small. Therefore, this one-dimensional SC-SM heterostructure, in the limit of small Δ, can effectively turn into a spinless p-wave superconductor if μ is placed within the band gap, i.e., only the lower band is occupied. Using an analysis of the spectrum of the superconductor at $k = 0$, one can show the topological regime satisfies [28, 29]

$$V_z > \sqrt{\Delta^2 + \mu^2}. \tag{1.44}$$

A pair of MZMs should appear at each end of the nanowire when the Zeeman field V_z is larger than the TQPT field $V_{\text{TQPT}} = \sqrt{\Delta^2 + \mu^2}$.

1.4 MZM Signatures

In this section, we want to understand the physics behind the experimental signatures of Majorana zero modes (MZMs) in this one-dimensional SC-SM nanowire. There are several signatures of MZMs theoretically predicted, including

(a) Zero-bias Conductance Peak (ZBCP) [54]

Since Majorana operator is its own anti-particle, it should be a zero-energy mode in the SC system. The differential conductance should show a peak at zero-bias voltage.

(b) Quantized Conductance [54–56]

The ZBCP probed by a single-channel lead should be quantized at $2e^2/h$ at zero temperature.

(c) Non-local Correlation [81–83]

The ZBCPs for a pair of MZMs should show up at each end at once.

(d) Gap Closing and Reopening [84, 85]

The bulk gap closes as the system approaches the TQPT field from below, and the bulk gap reopens as the system goes away from the TQPT field to further above.

(e) Majorana Oscillations [81]

For a finite length of the nanowire, the overlap of wave functions result in zero-energy mode splitting, whose amplitude increases as the magnetic field increases.

However, topologically-trivial Andreev bound states (ABSs) can mimic several signatures of MZMs, such as the above (a)-(c) [62, 83, 86]. Also, the experimental signal from gap closing

Figure 1.4: Schematic plot of the normal metal-superconductor (NS) junction. A bias voltage is applied to the normal metal, with the superconductor grounded.

and reopening is usually too weak to identify TQPT field [87]. Thus, the path to verify the existence of MZMs becomes harder in the presence of these experimental complexities. Since these hallmarks that MZMs exhibit as above are mostly based on conductance measurements through a normal metal-superconductor (NS) junction [see Fig. 1.4], it is essential to understand the quantum transport across the NS junction, which will be discuss in Sec. 1.4.1.

1.4.1 Resonant Andreev Reflection

To understand the differential conductance measured across a NS junction, we need to analyze the electron/hole scattering problem so as to count the net flowing charge per unit time. Realistically, a tunnel barrier is usually produced at the interface of normal metal and superconductor. This tunnel barrier can therefore affect the scattering results as well. There can be three situations when an electron is incident from the normal metal to the SC:

(a) Normal reflection: reflected back as a regular electron, as in Fig. 1.5(a)

(b) Andreev reflection: reflected back as a hole, generating one Cooper pair in the SC, as in Fig. 1.5(b)

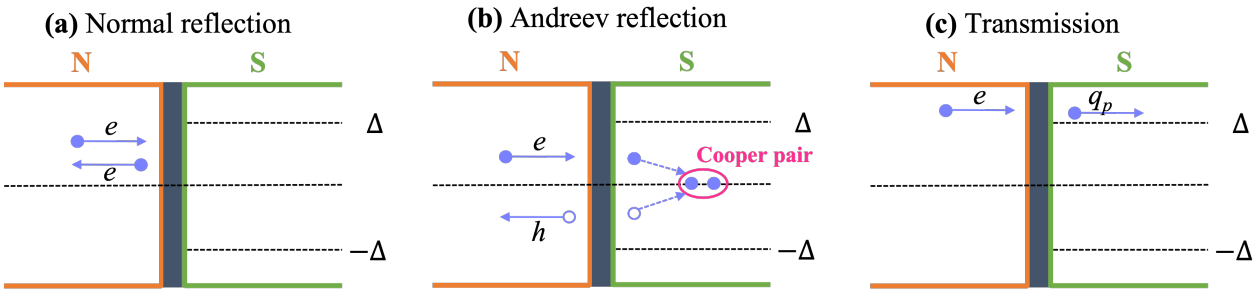

Figure 1.5: Schematic plots of the scattering processes in an NS junction: (a) Normal reflection. (b) Andreev reflection. (c) Quasi-particle transmission.

(c) Transmission: transmitted as a propagating quasi-particle in the SC, as in Fig. 1.5(c)

When the incident electron holds the energy smaller than the SC gap (i.e., $E < \Delta$), only normal reflection [case (a)] and Andreev reflection [case (b)] can happen. Only when the energy of the incident electron is larger than the SC gap (i.e., $E > \Delta$) can the transmission [case (c)] happen and quasi-particles are allowed to propogate in the SC. Normal reflection does not contribute any charged particle to the current in the SC [see Fig. 1.5(a)]. On the other hand, for each electron going through Andreev reflection, it contributes a Cooper pair of charge $2e$ to the SC [see Fig. 1.5(b)]. We can understand that Andreev reflection is a transmission process for an incoming particle from the electron channel to the hole channel in the normal-metal lead [see Fig. 1.6]. In generic case, the transmission is less than one due to the tunnel barrier. However, in a special case where the zero-energy Majorana bound state (i.e., MZM) is produced in the SC, the resonant transmission happens such that an electron is completely transmitted into a hole in the normal lead. Therefore, Majorana zero modes can induce the perfect resonant Andreev reflection. More rigorous theoretical arguments regarding this can be found from Ref. [54–57].

Here we provide a simple way via S-matrix to show the resonant Andreev reflection. Af-

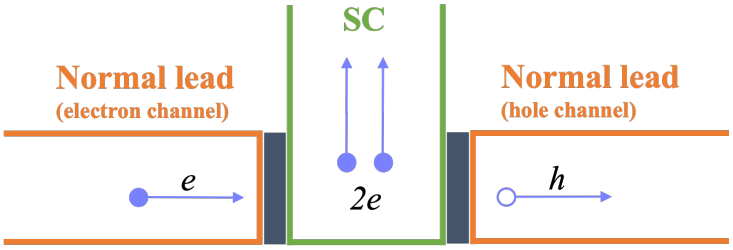

Figure 1.6: Schematic plot of Andreev reflection viewd as a transmission phenomenon from an electron channel to a hold channel of the normal-metal lead.

ter all, it is efficient and standard to introduce the S-matrix method for the quantum transport problem. Suppose the incident wave function with energy within the SC gap (i.e., $E < \Delta$) is $\Psi_{\text{in}} = [\psi(0^-), \psi^\dagger(0^-)]^T$ and the reflected output wave function is $\Psi_{\text{out}} = [\psi(0^+), \psi^\dagger(0^+)]^T$, where $x = 0$ represents the position where the scattering occurs. In our case, NS junction is the scattering region. By matching the wave functions from both sides of the scattering region with the boundary conditions, the particle-hole reflection coefficients can be summarized into the reflection matrix

$$R(E) = \begin{pmatrix} r_{ee} & r_{eh} \\ r_{he} & r_{hh} \end{pmatrix} \tag{1.45}$$

such that

$$\Psi_{\text{out}} = R(E)\Psi_{\text{in}}. \tag{1.46}$$

r_{ee} and r_{he} are the normal and Andreev reflection coefficients based on an incoming electron, while r_{hh} and r_{eh} are the normal and Andreev reflection coefficients based on an incoming hole. Since our system is SC, particle-hole symmetry constrains the reflection matrices by the relation

$$\tau_x R^*(-E)\tau_x = R(E). \tag{1.47}$$

Let's take $E = 0$ in Eq. (1.47) because we want to analyze the case of Majorana zero modes. Then Eq. (1.47) becomes

$$\tau_x R_0^* \tau_x = R_0, \tag{1.48}$$

where $R_0 = R(E = 0)$. By taking the determinant of Eq. (1.47), we get

$$\det(R_0) = \det(\tau_x R_0^* \tau_x) = \det(R_0^*) = [\det(R_0)]^*, \tag{1.49}$$

which implies $\det(R_0)$ to be real.

With the energy conservation condition (i.e., the sum of the normal reflected energy and the Andreev reflected energy is constant), the reflection matrix requires to be unitary $R^\dagger(E)R(E) = 1$, or

$$|r_{ee}|^2 + |r_{he}|^2 = |r_{eh}|^2 + |r_{hh}|^2 = 1 \tag{1.50}$$

in the single-channel lead case. The unitarity condition of reflected matrices indicates

$$1 = \det(R_0^\dagger R_0) = |\det(R_0)|^2. \tag{1.51}$$

So the quantity $Q \equiv \det(R_0)$ has two solutions

$$Q = |r_{ee}|^2 - |r_{he}|^2 = \pm 1. \tag{1.52}$$

Together with Eq. (1.50), one can find out there are only two situations in the case of a single-channel lead when the energy is zero:

(a) Perfect normal reflection: $|r_{ee}| = 1$, $|r_{he}| = 0$, and $Q = 1$.

(b) Perfect Andreev reflection: $|r_{ee}| = 0$, $|r_{he}| = 1$, and $Q = -1$.

The differential conductance measured across a NS junction is defined as

$$G = \frac{\partial I}{\partial V}, \tag{1.53}$$

where I is the current passing through the normal lead and V is the bias voltage of the normal lead relative to the grounded SC. Since the perfect resonant Andreev reflection corresponds to the existence of MZMs in the topological SC, the ZBCP introduced by the MZM is

$$G = \frac{e^2}{h}\left(1 - |r_{ee}|^2 + |r_{eh}|^2\right) = \frac{2e^2}{h} \tag{1.54}$$

based on BTK formalism [88]. Therefore, the presence of MZMs should exhibit a quantized ZBCP at $2e^2/h$ at zero temperature in the case of a single-channel lead.

1.5 Experiment Review

1.5.1 The Earliest observed ZBCP

There has been a deluge of experimental works [31–38, 41–46, 48–50, 52, 89] trying to detect MZMs in the 1D SC-SM nanowire following the theoretical proposals in 2010 [26–29]. Here we intend to review one of the first experimental transport studies done by Mourik *et al.* in 2012 [31].

In this experiment, the indium-antimonide (InSb) semiconducting nanowire of strong SOC is deposited on the niobium-titanium-nitride (NbTiN) superconductor [see Fig. 1.7(a)]. A normal

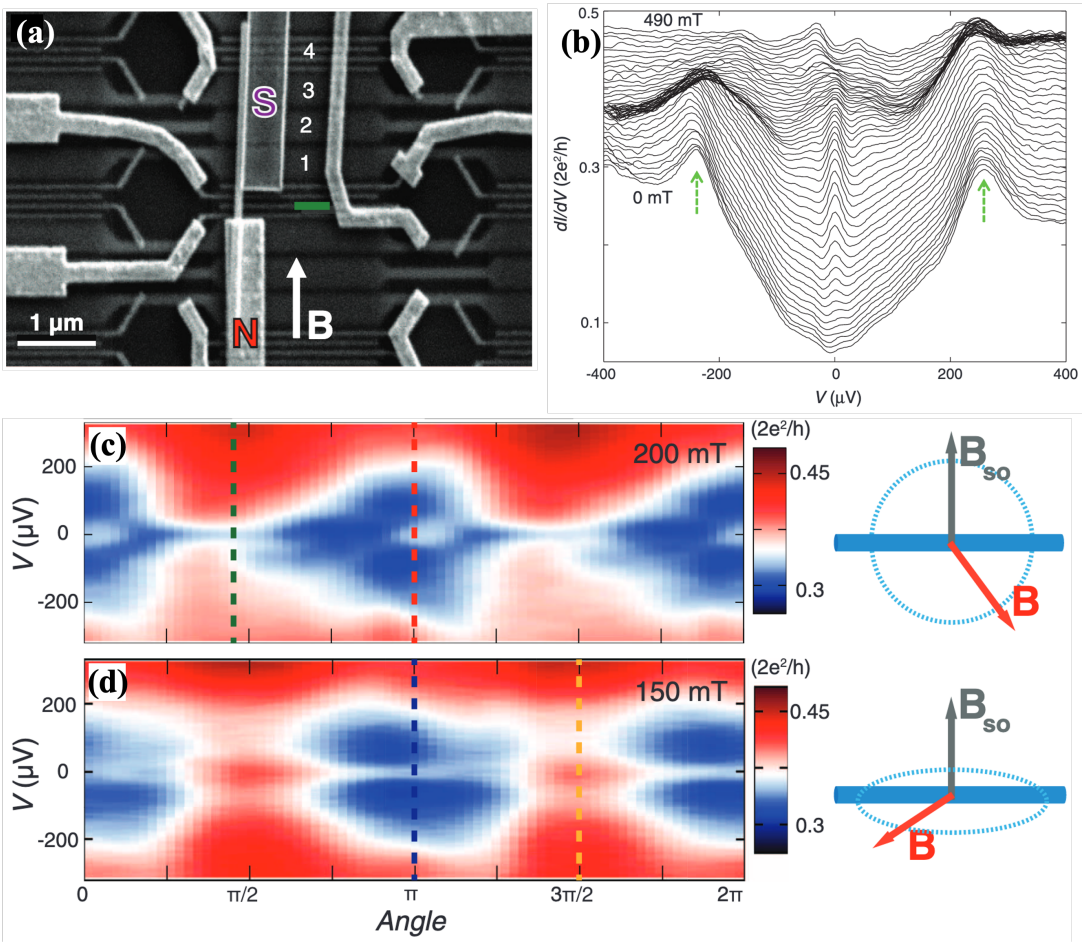

Figure 1.7: 2012 Delft experiment on the 1D superconductor-semiconductor nanowire. (a) The scanning electron microscope image of the setup. A semiconducting nanowire made of InSb is in contact with a normal lead (N) and a superconductor (S). Four gates (marked by numbers 1-4) underneath the nanowire are for tuning the chemical potential of the nanowire. A gate (marked in green) is used to tune the tunnel barrier across the tunnel junction. (b) Differential conductance dI/dV as a function of bias voltage V for different strengths of magnetic field ranging from 0 to 490 mT (in steps of 10 mT). The traces are offset for clarity. (c) Differential conductance dI/dV as a function of bias voltage V and angle of the magnetic field. When the angle is 0 or π, the magnetic fields are perpendicular to the SOC direction. When the angle is $\pi/2$ or $3\pi/2$, the magnetic fields are parallel to the SOC direction. (d) Differential conductance dI/dV as a function of bias voltage V and angle of the magnetic field. The magnetic field is always perpendicular to the SOC direction. This figure is adapted from Ref. [31].

lead, which is attached to the end of the nanowire, is used to measure the current across the tunnel junction (N-SM-SC). A tunnel barrier between the normal lead and the nanowire can be adjusted by a gate at the interface. An external magnetic field, whose strength and direction can be controlled, is applied parallel to the surface of the superconductor.

The key results that show the ZBCP emerges as the magnetic field increases are in Fig. 1.7(b). Since the theoretical proposal suggests the ZBCP induced from the topological MZM only appears above the TQPT field, this experimentally observed ZBCP was seen as a breakthrough in search of MZMs in the nanowire system. Another theoretically-consistent evidence is shown in Fig. 1.7 (c)(d), where the conductance is measured with a variation of the magnetic field angle. The ZBCP is the most pronounced when the magnetic field is perpendicular to the SOC direction, which is when the angle is 0 and π in Fig. 1.7(c) and for all angles in Fig. 1.7(d). The ZBCP vanishes as the magnetic field approaches parallel to the SOC direction, which is when the angle is $\pi/2$ and $3\pi/2$ in Fig. 1.7(c). These experimental features are in line with the theory, which strongly suggests this ZBCP is a clear sign of the existence of MZMs.

However, there are still several defects in these results compared to the ideal theoretical prediction. First of all, after calibrated by the offset, the observed ZBCP is at most 0.1 times of the predicted quantized value ($2e^2/h$). Secondly, the induced SC gaps (marked by the green arrows in Fig. 1.7(b)) are not as obvious as required to facilitate the appearance of topological MZMs. This is the so-called "soft gap" issue. Recent experiments made a lot of efforts to consolidate a hard gap in the nanowire, mostly by fabricating a better interfacial contact between the superconductor and the nanowire [36, 39].

1.5.2 The Quantized Conductance Experiment

While the fabrication of the Majorana nanowire device has improved a lot over the past 10 years and the quantized ZBCP has finally been observed [38, 44, 52], several theoretical works [58–69] show that trivial QD-induced ABSs, inhomogeneous potential, or disorder-induced random potential can produce quantized ZBCP very similar to the MZM-induced ZBCP. So the quantized ZBCP is not a sufficient indication for the existence of MZMs. Nonetheless, MZM should exhibit a robust quantized plateau near zero temperature. This idea becomes more emphasized especially after the 2018 Nature paper [44], which showed the quantized conductance, got retracted in part because of a calibration error. Fig. 1.8 demonstrates the recalibrated version of the quantized conductance experiment conducted by Zhang *et al.* [52] Fig. 1.8(a)(b) show the schemes of the 1D nanowire device with the tunnel gate controlling the tunnel barrier height and the corresponding ZBCP [Fig. 1.8(e)] and normal-state conductance [Fig. 1.8(f)]. The ZBCP does not show robust quantization when the charge jump occurs near the white arrow. Moreover, the ZBCP in Fig. 1.8(c) can be tuned to be above or below the quantization value by the tunnel gate, which does not exhibit the robustness of the quantized ZBCP, either.

One may therefore be motivated to study the robustness of quantized ZBCPs quantitatively in both topological (pristine nanowire) and trivial scenarios (with QD, with smooth-varying potential, or with disorder-induced random potential). In Chapter 2, we propose the quality factors to quantify the robustness of ZBCPs. We also calculate the ZBCP as a function of the normal-state conductance in different scenarios, and use the quality factors to analyze these scenarios, aiming at distinguishing the topological MZMs from other trivial bound states. This project leads to the work of Ref. [90].

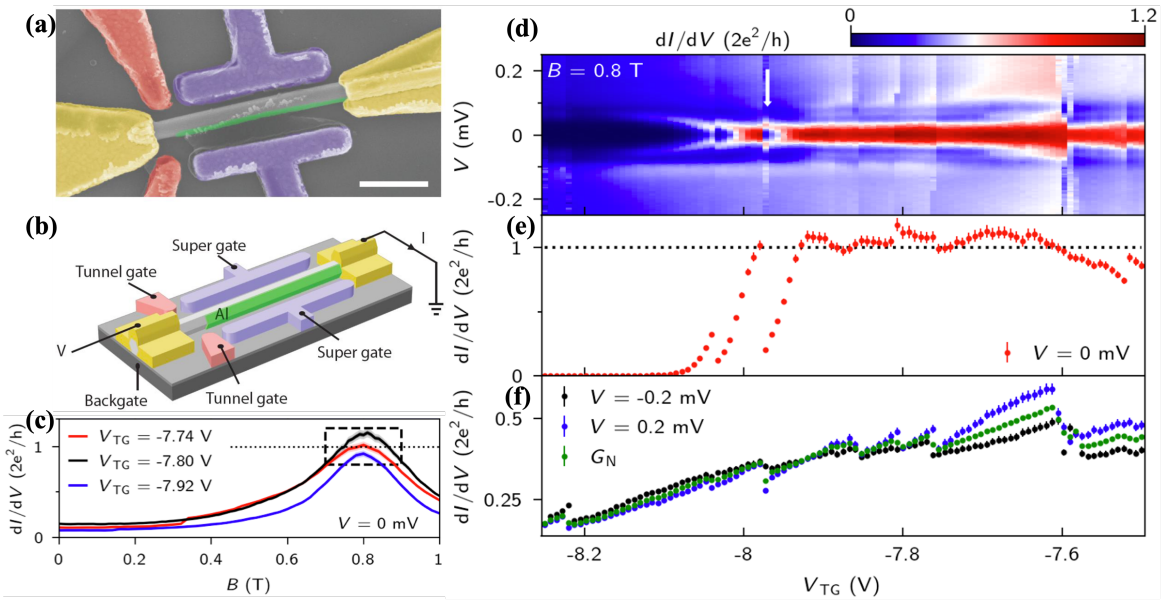

Figure 1.8: 2018 Delft experiment [44] showing the conductance on the order of $2e^2/h$ on the 1D nanowire device. The data here is the calibrated version [52]. (a) False color scanning electron micrograph of the nanowire device. (b) Schematic plot of the nanowire device. A InSb nanowire is covered by a thin superconducting Al shell on two sides. Side gates and contacts are Cr/Au. A bias voltage V is applied to the contact (yellow) on the left and a current I is drained from the contact on the right. (c) Differential conductance dI/dV as a function of the magentic field B for three different tunnel gate voltages. (d) Differential conductance dI/dV as a function of tunnel gate voltage V_{TG} and bias voltage V. White arrow indicates a charge jump with a large effect on the conductance. (e) Horizontal linecut from (d) at $V = 0$. (f) Horizontal linecuts at finite bias $V = \pm 0.2$ mV (black, blue), showing the out-of-gap conductance increasing over the same range in tunnel gate voltage. The normal conductance G_N (green) is taken as the average value of the other two out-of-gap linecuts (black, blue). This figure is adapted from Ref. [52].

Since a bare ZBCP probed as usual from one end does not prove the appearance of MZMs, detecting the non-local property of MZMs is highly encouraged. One may think if there is a way to measure the MZM wave function to analyze the its locality. However, there is no way to measure the wave functions in experiments though it is simple to calculate the wave function distribution in real space. The only way to check the non-local correlation of MZMs at the ends of the wire is through the QPC conductance measurement. Therefore, it is necessary to detect ZBCPs at both ends of the nanowire simultaneously. In the scenario where the unintentional QD exists only at one end of the wire, the QD-induced ZBCP should not show at both ends. In Chapter 3, we will provide detailed simulation results for these two scenarios to study the presence and absence of end-to-end non-local conductance correlations, which leads to the publication of Ref. [83].

1.5.3 Coulomb Blockade Experiment

The other way to probe the localization of states at both ends of the nanowire is through the Coulomb blockade spectroscopy because the CB conductance does not reflect the localized state only at one end. An experimental work [91] in 2016 shows the exponential decay of spin-splitting amplitude with the nanowire length increasing [see Fig. 1.11(d)], which seems to be an indication for the existence of MZMs. No matter if it is a correct interpretation or not, it is worth reviewing these experimental results [91] before the readers dig into our theoretical study on the CB Majorana nanowire.

The CB tunneling occurs when the scale of the device is small enough such that each tunneling electron needs to overcome the electrostatic charging potential carried by the device.

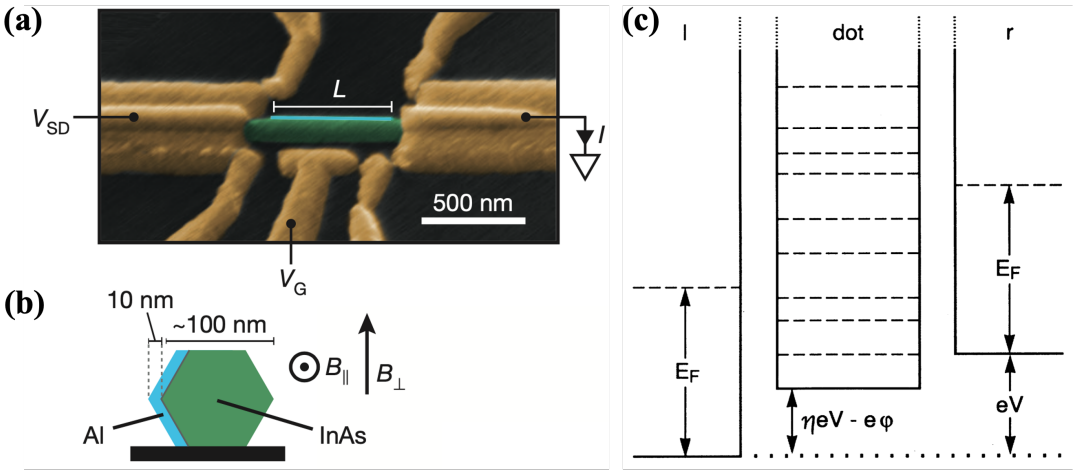

Figure 1.9: Majorana Coulomb Blockaded island device by Albretcht *et al.* (a) False color scanning electron micrograph of the InAs nanowire device. The source-to-drain voltage V_{SD} is applied on the left side of Ti/Au contact (yellow), whilte the gate voltage V_G is applied to change the chemical potential of the nanowire. Two-facet Al shell (light blue) of length L is covering the nanowire. (b) Cross-section of a hexagonal InAs nanowire showing the orientation of the Al shell and magnetic field directions $B_\parallel$ and $B_\perp$. (c) Profile of the electrostatic potential energy (solid curve) through the tunnel barriers. Ther Fermi levels in the left and right reservoirs, and the discrete energy levels in the quantum dot, are indicated (dashed lines). Panel (a)(b) is adapted from Ref. [91] and Panel (c) is adapted from Ref. [92].

The Majorana nanowire can easily fall into the CB regime when the wire is relatively short ($\sim$ 1 μm) and the transmission to the end of the wire is lowered by the tunnel barriers. Since the Majorana nanowire is isolated from normal-metal leads in this regime, we also called the nanowire "Majorana island" when the CB effect kicks in. A source-to-drain bias voltage V_{SD} is applied to one end of the nanowire relative to the other grounded end [Fig. 1.9(a)], which can change the Fermi levels of the source and drain terminals. The gate voltage V_G is applied to the nanowire to change its chemical potential. Only when the chemical potential of the nanowire is within the voltage window formed by the Fermi energies of source and drain terminals can the transport occurs [see Fig. 1.9(c)].

The simplest way to understand the CB conductance peaks is from the ground-state energy spectrum, as in Fig. 1.10. The spectrum can be described by

$$E_N(N_G) = E_C(N_G - N)^2 + p_N E_0, \tag{1.55}$$

where $N_G = CV_G/e$ is the gate-induced charge (with electron charge e and gate capacitance C) and N is the electron occupancy of the nanowire. It is easy to see that this charging energy is periodic in N_G as N is shifted equally from the formula when the ground-state quasi-particle energy $E_0 = 0$. Since the nanowire is proximitized by the superconductor, the ground-state energy is zero when the electron occupancy N is even, and equal to the lowest quasi-particle energy when N is odd. The CB transport happens at the intersection of the two parabolas. Therefore, for a SC system, the CB peaks are intrinsically $2e$-periodic due to the Cooper-pair transport [Fig. 1.10 (blue curve)]. The Majorana nanowire can contribute to $1e$-periodic transport when MZM appears and the lowest quasi-particle energy becomes zero [Fig. 1.10 (red curve)]. There can be a transitioning regime from $2e$-periodic transport to $1e$-periodic transport, which is expressed in green in Fig. 1.10. In Majorana nanowires, this transition is typically done by adjusting the magnetic field, as one can see in the experimental CB conductance in Fig. 1.11.

Fig. 1.11 (a)(e)(f)(g) show the CB conductance as a function of gate voltage V_G and magnetic field B. It is clear that the CB peaks change from $2e$ periodicity (below 0.1 T) to $1e$ periodicity (~ 0.2 T) as the magnetic field is increasing. One can see this CB conductance shows the "bright-dark-bright" pattern, especially in the long nanowire case [Fig. 1.11(g)]. Another way to analyze the CB conductance results is by tracking the CB peak positions in the parameter space and calculating the spacing difference between peaks, as in Fig. 1.11(b)(c). We call this quantity

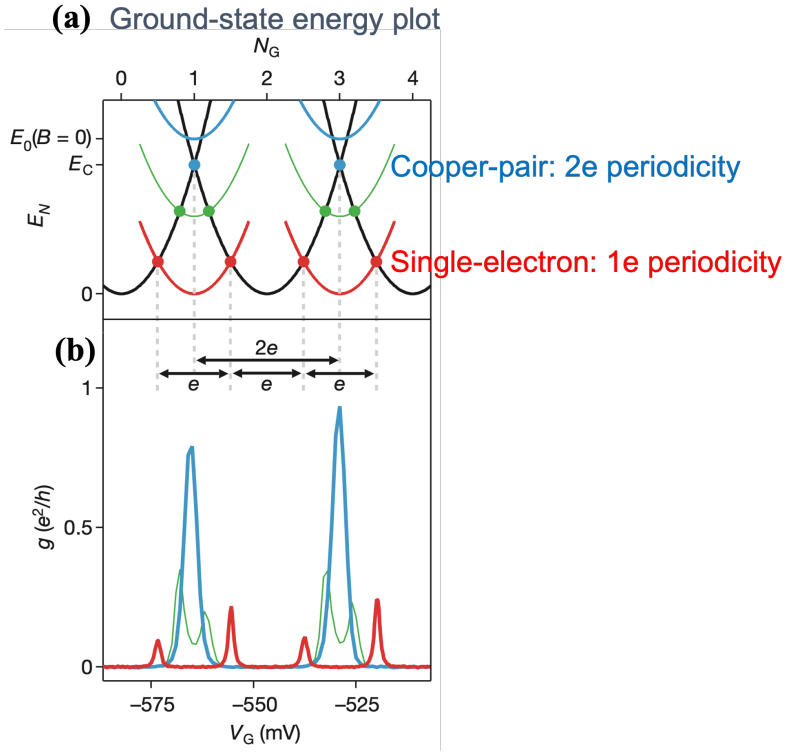

Figure 1.10: Coulomb blockade spectrum with single quasi-particle energy level. (a) The CB energy of the superconducting island, with or without sub-gap states: $E_N(N_G) = E_C(N_G - N)^2 + p_N E_0$, where $N_G = CV_G/e$ is the gate-induced charge (with electron charge e and gate capacitance C) and N is the electron occupancy. E_0 is the energy of the lowest quasiparticle state, which is filled for odd parity ($p_N = 1$ for odd N) and empty for even parity ($p_N = 0$, for even N). Ground-state energies for even (odd) N are shown in black (color). Transport occurs at the intersections of the parabolas, indicated by the filled circles. (b) Differential conductance $g = dI/dV_{\mathrm{SD}}$ versus gate voltage V_G at zero bias ($V_{\mathrm{SD}} = 0$) for magnetic fields $B_{\|} = \{0, 80, 220\}$ mT. The splitting of the $2e$-periodic peak (light blue light) reflects a transition from Cooper-pair tunneling to single-quasi-particle charging of the Coulomb island. Evenly spaced $1e$-periodic Coulomb peaks are characteristic of a zero-energy state. This figure is adapted from Ref. [91].

"oscillation conductance peak spacing" (OCPS). In Fig. 1.11(b)(c), OCPSs are decreasing as the magnefic field is increasing. Finally, Albrecht *et al.* also provides the first oscillation amplitude of OCPSs for five devices of different length, as in Fig. 1.11(d). The data in Fig. 1.11(d) is fitted well with an exponential function $A = A_0 \exp(-L/\xi)$ that characterizes the topological protection of MZMs. We would like to explain if these experimental features are tenable for the existence of MZMs, with solid theories and realistic simulations, as in Chapter 4. One can find the corresponding published work in Ref. [93].

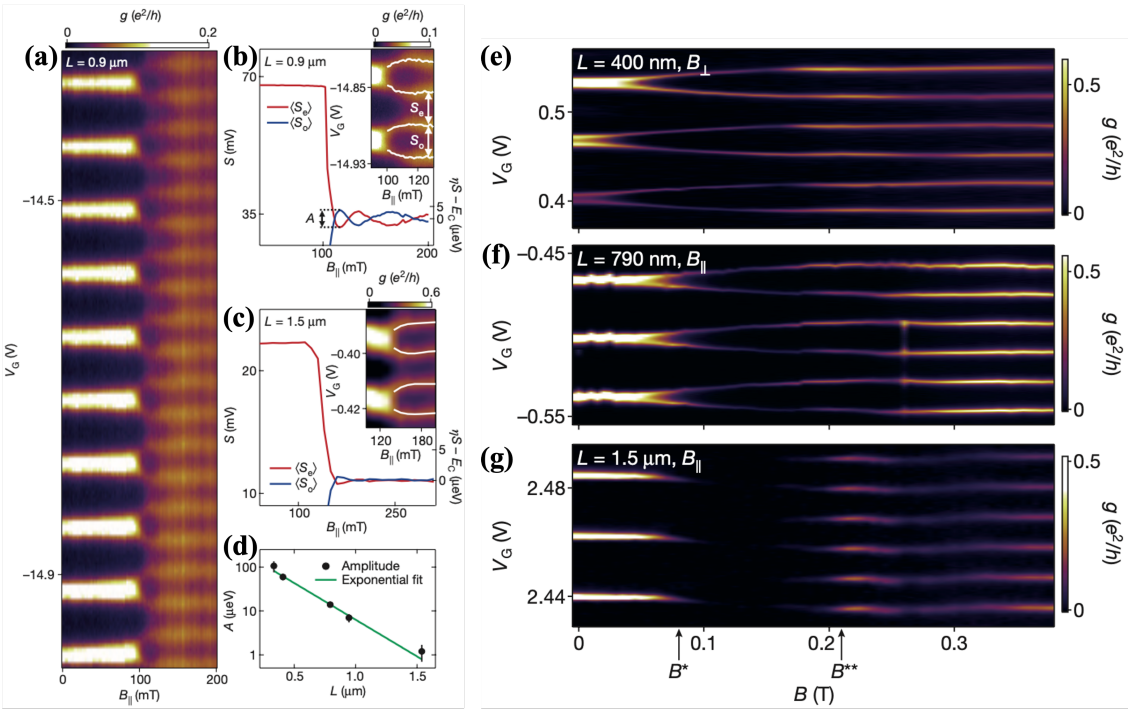

Figure 1.11: Coulomb blockade Peak splitting in magnetic field. **(a)** Zero-bias conductance g as a function of gate voltage V_G and parallel magnetic field $B_\parallel$ for the $L = 0.9$ μm device, showing a series of $2e$-periodic Coulomb peaks below about 100 mT and nearly $1e$-periodic peaks above about 100 mT. **(b)** $\langle S_{e,o} \rangle$: Average peak spacing as a function of magnetic field $B_\parallel$ for even and odd parities measured in a $L = 0.9$ μm device. The Coulomb peaks become evenly spaced at $B_\parallel = 110$ mT; at higher fields, their spacing oscillates around $\langle S_e \rangle = \langle S_0 \rangle$ **(c)** Similar to (b), but for a longer wire, $L = 1.5$ μm. **(d)** Oscillatory amplitude A plotted against the wire length for 5 devices (L ranging from 330 nm to 1.5 μm; black dots). The green line is an exponential fit to the data: $A = A_0 \exp(-L/\xi)$ with $A_0 = 300$ μeV and $\xi = 260$ nm. **(e)** Conductance g as a function of magnetic field $B_\perp$ and V_G for device length $L = 400$ nm. **(f)** Similar to (a), but for device length $L = 790$ nm. **(g)** Similar to (a), but for device length $L = 1.5$ μm. This figure is adapted from Ref. [91].

Chapter 2: **Quality Factors for Zero-bias Conductance Peaks**

As of the introduction in Chapter 1, particularly the sub-section 1.5.2 on Zhang *et al.* experiment [44, 52], the observation of ZBCPs quantized near $\sim 2e^2/h$ is insufficient to be the evidence of MZMs. Instead, the robustness of the quantized zero-bias conductance becomes a crucial feature of MZMs that could possibly help the ZBCPs associated with topological MZMs (which are called "good" ZBCPs [58]) stand out from other non-topological ZBCPs. In this chapter, we would like to introduce new quality factors that not only can quantify the robustness of quantization, but also can characterize the topological property of the ZBCP. These new quantities should be able to directly assess the quantized ZBCPs measured in the experiment, giving the experiments practical use. Since the reported ZBCPs so far, which are claimed to be from MZMs, do not exhibit the robustness of quantization, it is most likely that these experimentally-observed ZBCPs are either associated with ABSs induced from QDs or inhomogeneous potential (which are called "bad" ZBCPs [58]), or associated with disorder-induced fermionic bound states (which are called "ugly" ZBCPs [58]). While the MZM-based ZBCPs intrinsically show robust quantization of $2e^2/h$ at zero temperature when probed from a single-channel tunnel contact, ZBCPs coming from other non-topological sources can also possibly reach somewhat robust quantization with enough parameter fine-tuning [86, 94–97]. The main question we try to answer in this chapter is whether we can take advantages of the new quality factors, based on the robustness

of quantization, to distinguish topological "good" ZBCPs from trivial "bad" and "ugly" ZBCPs. In this sense, we would like to compare results of different models by calculating the conductance scanning through Zeeman field and tunnel barrier height, and even presenting the zero-bias conductance in terms of normal-state conductance G_N to simulate the experimentally-accessible data.

The quality factor F proposed here will be to gauge the robust quantized ZBCP to the changes of the tunnel barrier height because the Majorana quantization should be independent of the tunnel barrier height in the topological phase. To match the measurable quantity G_N, we will convert the tunnel barrier height to the corresponding G_N, and make the quality factor F dimensionless. The other proposed quality factor J will be to gauge the robust quantized ZBCP to the changes of Zeeman field. It is known that the parameter, Zeeman field, can change the system from topological phase to trivial phase, or vice versa. So the robustness over Zeeman field will be restricted by the boundaries of topological phase. However, we still want to introduce the quality factor J because the plot of conductance versus Zeeman field is the first step for searching MZMs. Using these two quality factors to analyze the simulated conductance of "good", "bad", and "ugly" scenarios, we can see if the quality factors work out to distinguish MZMs by verification of the calculated wave function.

2.1 Model

In this section, we will describe the 1D SC-SM nanowire [26–29] as in Fig. 2.1, which gives rise to "good", "bad", and "ugly" ZBCPs depending on the form of the potential in the real space [58].

We use the minimal single-band model to describe the 1D superconductor-proximitized semiconductor nanowire with intrinsic Rashba spin-orbit coupling and external Zeeman-field-induced spin splitting, in the form of a Bogoliubov-de Gennes (BdG) Hamiltonian

$$\hat{H} = \frac{1}{2}\int_0^L dx \hat{\Psi}^\dagger(x) H_{\text{NW}} \hat{\Psi}(x) \tag{2.1}$$

with

$$H_{\text{NW}}(\omega) = \left(-\frac{\hbar^2}{2m^*}\partial_x^2 - i\alpha_R \partial_x \sigma_y - \mu + V(x)\right)\tau_z + V_z\sigma_x + \Sigma(\omega, V_z) - i\Gamma, \tag{2.2}$$

where $m^* = 0.015m_e$ is the effective mass of an electron (m_e is the rest mass of an electron), μ is the chemical potential, and Γ is an infinitesimal dissipation parameter included to avoid singularities in $G_0(E)$ from resonant transmission. The Rashba spin-orbit coupling with strength α_R is perpendicular to the wire [98] and the magnetic field B is applied along the nanowire longitudinally such that the Zeeman term $V_z = \frac{1}{2}g\mu_B B$, where μ_B is Bohr magneton. The wave function in Eq. (2.1) is $\hat{\Psi}(x) = \left(\hat{\psi}_\uparrow(x), \hat{\psi}_\downarrow(x), \hat{\psi}_\downarrow^\dagger(x), -\hat{\psi}_\uparrow^\dagger(x)\right)^T$ in Nambu space, with $\sigma_{x,y,z}(\tau_{x,y,z})$ being Pauli matrices in spin (particle-hole) space. $\Sigma(\omega, V_z)$ is a superconducting self-energy

$$\Sigma(\omega, V_z) = -\lambda\frac{\omega\tau_0 + \Delta(V_z)\tau_x}{\sqrt{\Delta^2(V_z) - \omega^2}}\sigma_0, \tag{2.3}$$

where λ is the self-energy coupling strength with the parent SC. The self-energy is the effective renormalized energy introduced into the system when proximitized by the SC in the intermediate

regime [99, 100]. The Zeeman-field-varying SC gap is

$$\Delta(V_z) = \Delta_0\sqrt{1-(V_z/V_c)^2}\cdot\theta(V_c - V_z), \tag{2.4}$$

which hosts a bulk parent SC gap Δ_0 without Zeeman field and vanishes above the SC collapsing field V_c [1].The Heaviside-step function $\theta(V_c - V_z)$ indicates that the proximitized SC effect no longer exists in the nanowire when $V_z > V_c$, which is not the interest of this study. We will only numerically show the calculated conductance, energy spectrum, and wave functions below V_c. To implement the numerical calculation, we have to discretize the continuum Hamiltonian as in Eq. (2.2) into a lattice chain of tight-binding model [101] with the lattice constant $a = 10$ nm. Then the effective tight-binding tunneling strength is $t = \hbar^2/(2m^*a^2) \approx 25$ meV, the effective spin-orbit coupling strength is $\alpha = \alpha_R/(2a)$, and the wire length is given by $L = Na$, where N is the total number of the atoms constituting the nanowire.

The Hamiltonian in Eq. (2.2) becomes energy-dependent when the self-energy $\Sigma(\omega, V_z)$ is included. Thus, to get the energy spectrum, instead of diagonalizing $H_{NW}(\omega)$ directly, we can specify the peaks of the density of states (DOS) located at energies ω_0 from the Green's function, i.e.,

$$\rho_{\text{tot}}(\omega) = -\frac{1}{\pi} Im\left\{\text{Tr}\left[\tilde{G}(\omega)\right]\right\}, \tag{2.5}$$

and the Green's function is

$$\tilde{G}(\omega) = \frac{1}{\omega - H_{\text{NW}}(\omega)}, \tag{2.6}$$

[1]The reason for this gap collapse is unclear. One possiblity is a strong magnetic-field-induced orbital effect in the parent SC. It could also simply result from the parent SC reaching the Clogston limit with the Zeeman spin splitting becoming equal to the bulk SC gap.

where $\omega = \omega_0 + i\eta$ and η is an infinitesimal real number for DOS brodening. The trace function $\mathrm{Tr}(\dots)$ in Eq. (2.5) is over the spatial space and sub-space (i.e., particle-hole and spins) of the Green's function matrix $\tilde{G}(\omega)$. Note that all the numerical results in this study include the self-energy because this is close to the real experimental situations.

We use the minimal model to simulate the nanowire instead of a more complex 3D model because it is found that the minimal model gives results very similar to complex models [86,102]. In addition, a more complex model will have many more unknown parameters, making it less useful.

Besides the SC-SM nanowire itself, the normal lead attached to the end of the nanowire (as the left green block in Fig. 2.1) is where the tunneling conductance is measured. The Hamiltonian of the normal lead is

$$H_{\text{lead}}(\omega) = \left(-\frac{\hbar^2}{2m^*}\partial_x^2 - i\alpha_R \partial_x \sigma_y - \mu + E_{\text{lead}} \right) \tau_z + V_z \sigma_x \tag{2.7}$$

with the on-site energy $E_{\text{lead}} \approx -25$ meV in the lead controlled by the gate voltage. A tunnel barrier induced at the interface of the normal-superconductor (NS) junction can be described by replacing $V(x)$ in Eq. (2.2) with a boxlike potential

$$V_{\text{barrier}}(x) = E_{\text{barrier}} \Pi_{l_{\text{barrier}}}(x), \tag{2.8}$$

along with $\lambda(x) = 0$, i.e., uncovered by the SC, as the blue barrier potential at the left end of the nanowire in Fig. 2.1.

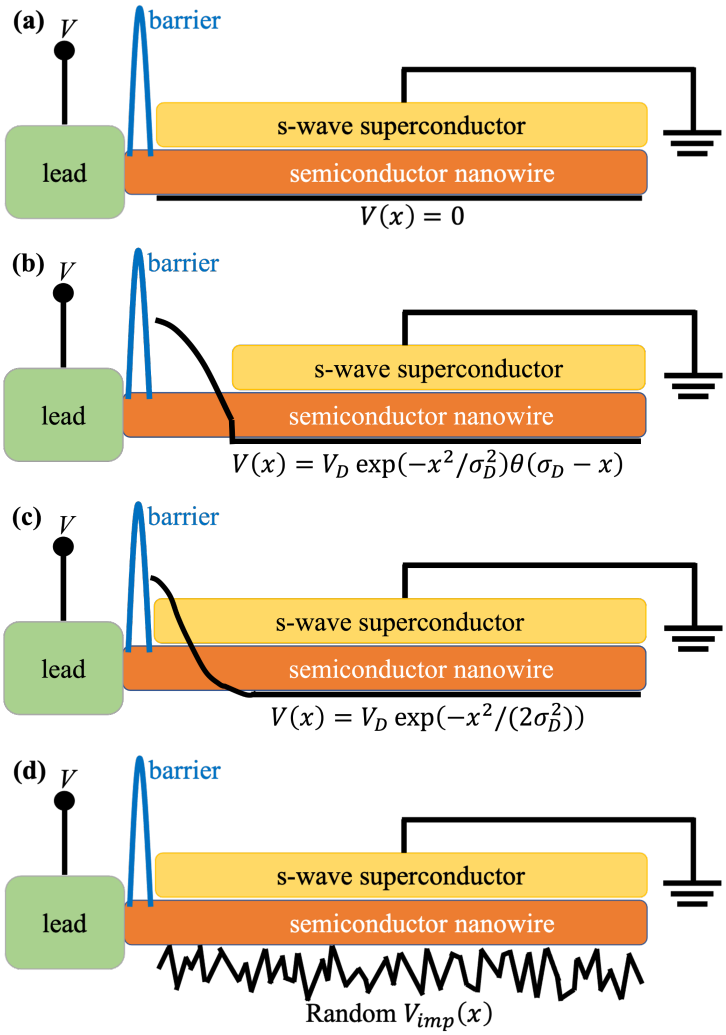

Figure 2.1: Schematic plots of the hybrid structures of a 1D superconductor-semiconductor nanowire and an attached lead, with different potentials. (a) Pristine nanowire: $V(x) = 0$. (b) Nanowire with a SC-uncovered quantum dot $V(x) = V_D \exp(-x^2/\sigma_D^2)$ with length σ_D. (c) Nanowire with an inhomogeneous potential $V(x) = V_D \exp(-x^2/(2\sigma_D^2))$. (d) Nanowire with random disorder $V(x)$.

2.1.1 Potential of Good/Bad/Ugly ZBCPs

The potential $V(x)$ in Eq. (2.2) determines whether the ZBCP belongs to "good", "bad" or "ugly" type [58]. There are four kinds of potentials we set up for numerical simulations to discuss the quality factor of quantization for different types of ZBCPs. First of all, Eq. (2.2) displays as a pristine nanowire that can produce "good" ZBCPs above TQPT field when $V(x) = 0$, as in Fig. 2.1(a). This Hamiltonian can definitely generates the genuine MZMs in the topological regime [26–29]. However, in the realistic experimental system, the unintentional potentials can produce "bad" and "ugly" ZBCPs.

The "bad" ZBCPs are defined as those ZBCPs appearing in the topologically-trivial regime, resulting from the deterministic spatially-varying potential. These "bad" ZBCPs are asscociated with so-called ABSs [59–69]. Such ABSs result from unintended quantum dots created when the lead is attached to the end of the nanowire. Such a quantum dot can arise either from mismatch of Fermi energies between the normal lead, semiconductor and the superconductor or from screened charged impurities or their combination [62, 64]. In our model, the quantum dot hosts a Gaussian potential at the end of the nanowire, part of which is not covered by the parent SC, as in Fig. 2.1(b). That is to say, the quantum dot potential is

$$V(x) = V_D \exp\left(-\frac{x^2}{\sigma_D^2}\right)\theta(\sigma_D - x), \tag{2.9}$$

where V_D is the dot barrier height and σ_D is the dot length. Also, the parent SC is mathematically expressed as

$$\Delta_{\text{SC}}(x, V_z) = \Delta(V_z) \cdot \theta(x - \sigma_D), \tag{2.10}$$

where $\Delta(V_z)$ is defined as Eq. (2.4). The Heaviside step function $\theta(x)$ describes that the SC only covers the nanowire outside of the quantum dot. A variation of the quantum dot model with $\sigma_D' = \sqrt{2}\sigma_D$ to replace σ_D in Eq. (2.9) can occur where the quantum dot potential extends into the superconductor as shown in Fig.2.1(c). This can be accomplished by dropping the factor $\Theta(x - \sigma_D)$ in both Eqs. (2.9) and (2.10). Results for the case of a "bad" potential that do not specify an σ_D should be understood as being obtained from calculations which use this variant of the "bad" potential.

The "ugly" ZBCPs are defined as those ZBCPs showing up in the trivial regime, induced by random strong disorder. The typical potential that accounts for "ugly" ZBCPs is the onsite disorder-induced random potential which follows an uncorrelated Gaussian distribution statistically with zero mean and standard deviation σ_μ, i.e.,

$$V(x) = V_{\text{imp}}(x), \tag{2.11}$$

$$\langle V_{\text{imp}}(x)\rangle = 0, \tag{2.12}$$

$$\langle V_{\text{imp}}(x)V_{\text{imp}}(x')\rangle = \sigma_\mu^2\delta(x - x'), \tag{2.13}$$

as in Fig. 2.1(d). Each set of "ugly" results in Sec. 2.3.3 is based on just one particular configuration of $V_{\text{imp}}(x)$, which is unpredictable contrary to the deterministic quantum dot potential in Eq. (2.9). This random impurity potential can induce trivial "ugly" ZBCPs which mimic "good" ZBCPs.

2.1.2 Differential Conductance Formalism

We numerically compute the local differential tunneling conductance $G_0 = dI_L/dV_L$ from the normal lead at the left end through the NS junction by the scattering matrix (S-matrix) method [Eq. (2.14)]. Specifically, we use Python package KWANT [103] to compute the differential conductance with the in-built scattering matrix derived from the known Hamiltonian. The conductance at zero temperature can be expressed and computed by the scattering matrix elements as follows:

$$G_0 = N - \text{Tr}(r_{ee} r_{ee}^\dagger - r_{eh} r_{eh}^\dagger) \tag{2.14}$$

in the unit of e^2/h, where N is the number of the conducting channels in the lead, r_{ee} is the normal reflection matrix, and r_{eh} is the Andreev reflection matrix. In our system with only one-subband lead, $N = 2$ counts the two spin modes. The conductance at finite temperature $G(V)$ can be further calculated by the convolution of the zero-temperature conductance $G_0(E)$ and the derivative of the Fermi-Dirac distribution $\partial f(E,T)/\partial E$, i.e.,

$$G(V) = -\int_{-\infty}^{\infty} G_0(E) \frac{\partial f(E-V,T)}{\partial E} dE \tag{2.15}$$

$$= -\int_{-\infty}^{\infty} G_0(E) \left[\frac{1}{4T} \text{sech}^2 \left(\frac{V-E}{2T} \right) \right] dE. \tag{2.16}$$

The above is the formalism for simulating the differential tunneling conductance in our results.

2.1.3 Wave Functions

To determine the topological superconducting characteristic of a one dimensional system, it is necessary to look at the structure of the Majorana modes. Specifically, a topological superconductor is characterized by spatially well-separated Majorana wave functions [65, 85, 104]. On the other hand, the ABSs display two overlapping wave functions at one end of the nanowire [83], even we construct their wave functions in the Majorana mode. The $4N$ component Nambu wave function $\Psi(x)$ for an N-site system, corresponding to any eigenenergy ω_0 obtained from peaks of $\rho(\omega)$ in Eq. (2.5) can be obtained as the eigenstate of $H_{\rm NW}(\omega_0)$ with eigenvalue ω_0. In a clean or weakly disordered system, one could determine the topological characteristic of the system by a straightforward calculation of the topological invariant [2, 101, 105]. However, this approach is not well-defined for systems without a spectral or transmission gap, e.g. short strongly disordered nanowires. The systems of interest here, shown in Fig. 2.1, are systems with a few sub-gap states. In this case, it is simpler to directly determine the topological character of the system by analyzing the low-energy wave functions directly as we describe below.

Majorana mode wave functions, even for a topological superconducting system of finite size, split into non-zero energy ($\omega_0 = \pm\epsilon$) eigenstates $\Psi_\epsilon(x)$ and $\Psi_{-\epsilon}(x)$ that are not themselves Majorana (i.e., particle-hole symmetric). For a low-energy eigen-wave function $\Psi_\epsilon(x)$ corresponding to a positive energy ϵ, one can use the particle-hole symmetry to define an orthogonal wave function $\Psi_{-\epsilon}(x) = \sigma_y\tau_y\Psi^*_\epsilon(x)$, which can be checked to be an eigenstate of $H_{\rm NW}(-\epsilon)$ with

eigenvalue $-\epsilon$. Then we can reconstruct the particle-hole symmetric Majorana wavefunctions as

$$\Phi_A(x) = \frac{1}{\sqrt{2}}\left[\Psi_\epsilon(x) + \Psi_{-\epsilon}(x)\right], \tag{2.17}$$

$$\Phi_B(x) = -\frac{i}{\sqrt{2}}\left[\Psi_\epsilon(x) - \Psi_{-\epsilon}(x)\right], \tag{2.18}$$

where $\Phi_{A,B}(x) = \left(\phi_\uparrow(x), \phi_\downarrow(x), \phi^*_\downarrow(x), -\phi^*_\uparrow(x)\right)^T$ are manifestly particle-hole symmetric. Note that this recipe suffers from a phase ambiguity of the eigenstate $\Psi_\epsilon(x)$ in the case of a general class D Hamiltonian, where it needs to be refined. This is not a problem for our case where the BdG Hamiltonian is real, which allows $\Psi_\epsilon(x)$ to be real. In general, $\Phi_{A,B}(x)$ are not the eigenfunctions of the BdG Hamiltonian, except when $\epsilon = 0$, they represent the MZMs. However, when ϵ is much smaller than the SC gap, the off-diagonal matrix element of the Hamiltonian $H_{\text{NW}}(\omega = 0)$ between $\Phi_{A,B}(x)$ is suppressed by a factor proportional to ϵ. The matrix elements of $H_{\text{NW}}(\omega = 0)$ between these states and any other excited states vanish as well. A system would be characterized as topological if the densities $|\Phi_\alpha(x)|^2$ corresponding to the state $\Phi_\alpha(x)$ are spatially separated.

If $|\Phi_A(x)|^2$ and $|\Phi_B(x)|^2$ are localized on the opposite ends of the nanowire without overlapping, then we have a pair of MZMs. On the contrary, if $|\Phi_A(x)|^2$ and $|\Phi_B(x)|^2$ are clearly overlapped with each other, then the system hosts ABSs. When one of $|\Phi_{A,B}(x)|^2$ is localized on one end of the wire, while the other one is localized in the middle of the wire, then this pair can be quasi-Majorana bound states when they are partially-overlapped with each other [65, 104, 106].

2.2 Quality Factor

The highlights of this work is the newly proposed quality factors to quantify the robustness of quantized conductance plateau. One of the most characteristic features of an MZM is quantized tunneling conductance [53–56]. To be precise, the ZBCP associated with an MZM is predicted to be exactly quantized at $T = 0$ for a sufficiently long topological wire, even when the transmission of the tunnel contact becomes vanishingly small [53–56]. One may feel this phenomenon counter-intuitive because the "normal"-state conductance G_N (for $V_{\text{bias}} \gg \Delta$) diverges as the transmission of the tunnel contact is reduced. We use quotation marks over "normal" here to emphasize that this quantity is close to the actual normal-state conductance only in the limit when the SC gap is the smallest energy scale in the problem. However, we will refer to this quantity as the normal-state conductance in the rest of the thesis because this is the most convenient quantity to measure. The large-series resistance that suppresses the transmission should decrease the conductance of the MZM, which contradicts the theoretical quantization. One can have insight into this counter-intuitive behavior by considering the analytic form of conductance

$$G_0(V) = \frac{2e^2}{h} \frac{(2V\Gamma)^2}{(V^2 - 4t^2)^2 + (2V\Gamma)^2} \tag{2.19}$$

that probes into a Majorana γ, which is weakly coupled to the Majorana γ' at the other end [55]. Note that t is the splitting of the Majorana modes and Γ is the tunnel broadening [55], which vanishes with the normal-state conductance, i.e., $G_N \sim (2e^2/h)\Gamma/\Delta$. As the Majorana splitting t vanishes, the above conductance takes the form of a Lorentzian with quantized height $(2e^2/h)$, but with a width Γ. However, following the finite-temperature modification as Eq. (2.15), the

quantized height is reduced as $T \geq \Gamma$ such that it approaches $G(V = 0) \sim (2e^2/h)\Gamma/T$. The latter form is more consistent with an expectation of a conductance limited by the normal-state conductance G_N.

The conductance G_z versus G_N plot for an ideal Majorana wire shown in Fig. 2.2(a) can further confirm the theoretically expected behavior for the ZBCP into an MZM described in the last paragraph. Ideally, the so-called normal-state conductance G_N is defined as the conductance without SC. Since it is often non-trivial to remove SC from a device without changing other factors, G_N is practically taken as an average of the conductance at $V_{\text{bias}} = \pm V_{\text{above}}$ where V_{above} is a large bias voltage above the SC gap. The variation of G_N in Fig. 2.2(a) is obtained by varying the barrier height, which can be implemented by tuning a tunnel gate voltage [44,52] or changing the tip-sample distance in STM [107] in the experiment. As a result of finite-temperature effect, the zero-bias conductance G_z in Fig. 2.2(a) shows a nearly quantized plateau when the normal-state conductance G_N is larger, but then decreases to zero linearly as G_N is reduced to zero, which is consistent with the theoretical analysis discussed in the last paragraph.

The quantized plateau independent of G_N is a phenomenal signatures of MZMs. While one can tune G_N and other parameters sufficiently to make the conductance into a SC quantized without the appearance of an MZM, this quantization is not expected to be robust. Nonetheless, the conductance into an MZM cannot be precisely quantized either due to the finite-temperature and finite-size effects. In this chapter, we aim to distinguish MZMs from other SC bound states by quantifying the robustness of the conductance plateau as shown in Fig. 2.2(a). To do this, we first identify the largest continuous interval $[G_{N,1}, G_{N,2}]$ on the x-axis over which the zero-bias conductance G_z is within a tolerance ϵ of quantization, i.e., $|G_z - 1| < \epsilon$ (in units of $2e^2/h$). Then, a quality factor $F = G_{N,2}/G_{N,1}$ that gauges the quantized degree of the conductance into

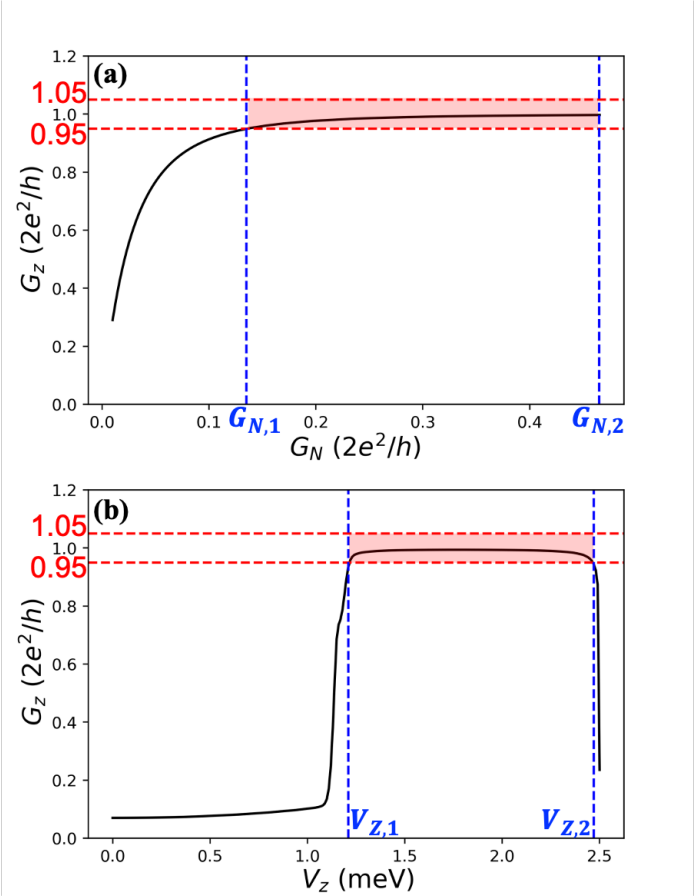

Figure 2.2: Schematic plots to show quality factors. The tolerance factor for quantized conductance is $\epsilon = 0.05$. (a) Black curve is the zero-bias conductance peak G_z versus normal-metal conductance (above SC gap) G_N. The quality factor $F \equiv G_{N,2}/G_{N,1}$, where $G_{N,1}$ and $G_{N,2}$ are defined by the consecutive normal-metal range for which the corresponding zero-bias peak is quantized within $[1-\epsilon, 1+\epsilon]$ in the unit of $2e^2/h$. (b) Black curve is the zero-bias conductance peak G_z versus Zeeman field V_z. The quality factor $J \equiv V_{Z,2}/V_{Z,1}$, where $V_{Z,1}$ and $V_{Z,2}$ are defined by the consecutive Zeeman field range for which the corresponding zero-bias peak is quantized within $[1-\epsilon, 1+\epsilon]$ in the unit of $2e^2/h$.

the MZM can be assigned. In Fig. 2.2(a), we set $\epsilon = 0.05$ as an example, meaning as long as the ZBCP is above 95% of $2e^2/h$ and below 105% of $2e^2/h$ [within pink region in Fig. 2.2(a)], then we take the ZBCP as a "well-quantized" ZBCP. In Sec. 2.3, we also demonstrate the numerical results of $\epsilon = 0.10$ and $\epsilon = 0.20$ for comparison. In some special cases, where the ZBCP over the visible range is sectioned into several parts [e.g. Fig. 2.4(f)], we take the largest consecutive normal-metal range to define $G_{N,1}$ and $G_{N,2}$.

The robustness of the topological phase should facilitate the quality factor to be applied to other parameters as well. The Zeeman splitting V_z controlled by tuning the applied magnetic field is one such parameter. As long as the topological gap is not destroyed, an MZM system associated with a reasonably large topological gap is expected to be robust to changes of V_z. Here, we will quantify the robustness of the MZM to the Zeeman field variations using a quality factor J defined in a similar way to the tunnel-gate quality factor F proposed in the last paragraph. Fig. 2.2(b) is the plot of zero-bias conductance peak G_z versus Zeeman field. This is the conductance linecut as in Fig. 2.3(e), which can be extracted from Fig. 2.3(a) with only $V_{\text{bias}} = 0$. The definition of quality factor J is similar to F as illustrated in the previous paragraph, except that we change the normal-metal conductance G_N part to Zeeman field V_z for the quality factor J. Formally, it is defined as $J \equiv V_{Z,2}/V_{Z,1}$, where $[V_{Z,1}, V_{Z,2}]$ is the range over which $|G_z - 1| < \epsilon$ in the unit of $2e^2/h$ and the tolerance factor for quantized conductance ϵ is a small number. Same as Fig. 2.2(a) as an example, we set $\epsilon = 0.05$, meaning 5% of the difference from the quantized value $2e^2/h$ as highlighted in the pink region in Fig. 2.2(b) are considered "well-quantized". All the explanations for F can also be applied to J as long as we replace $G_{N,1}$ and $G_{N,2}$ by $V_{Z,1}$ and $V_{Z,2}$, respectively.

So far, the definitions of F and J are not well-defined in cases where the zero-bias con-

ductance G_z does not lie in the quantized range (or as the pink regions in Fig. 2.2). In this case, we formally define F and J to be zero. In non-topological cases, where the zero-bias conductance G_z touches the quantized range slightly, F and J are just a bit higher but close to 1. In contrast, we will see from our numerical results in Sec. 2.3.1 that F and J can be much larger than 1 in the ideal MZM case at low temperature. The main goal of our work is to study F and J for various models to determine if they can be used to distinguish topological MZMs from other non-topological ZBCPs.

2.3 Numerical Results

In this section, we demonstrate simulated conductance plots for various tunnel gate strengths and magnetic field strengths to determine the robustness of quantized ZBCPs to the variety of parameter tuning. We will see that the quality factors F and J for the ideal MZM will be limited by temperature, topological gap and length. This section is mainly to compare the quality factors for the "good" ZBCP (i.e., ideal MZM) with other non-topological models for the ZBCP (i.e., "bad" and "ugly" ZBCPs). We believe that the quality factors F and J obtained from these numerical results can be directly applied to experiments because the quantities shown in this section are typically measured in most MZM experiments [38, 43, 44, 52, 107].

2.3.1 "Good" ZBCP

MZM-induced ZBCPs at the ends of topological superconducting nanowires are referred to as "good" ZBCPs [58]. Theoretically, they can be produced above the TQPT field in Majorana nanowire model as Fig. 2.1(a), which is the setup for the numerical results in Fig. 2.3. While this

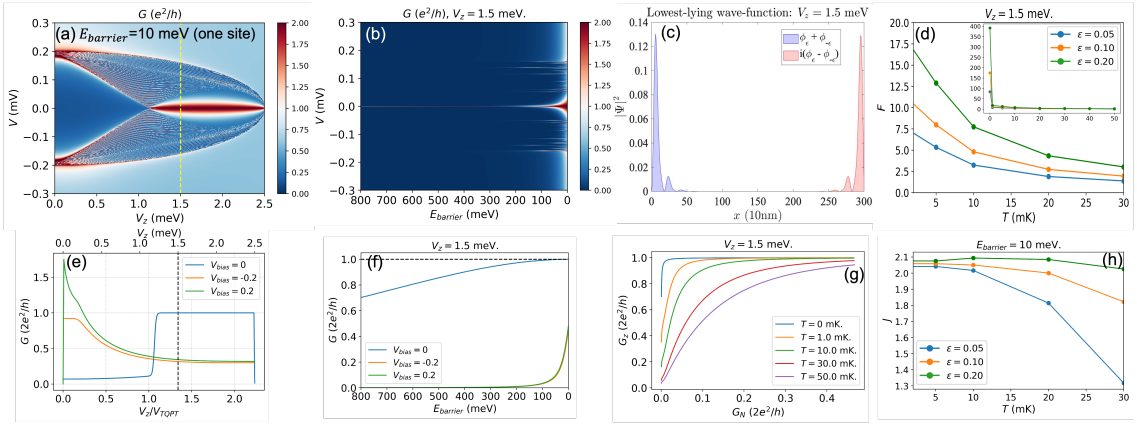

Figure 2.3: Numerical results for the "good" ZBCP. Parameters: $\alpha = 3.0$ meV, $\Delta_0 = 0.2$ meV, $V_c = 2.5$ meV, $L = 3.0$ μm, $\mu = 0.5$ meV, $\lambda = 1.0$ meV, and $\gamma = 10^{-4}$ meV. The TQPT field is at $V_{\text{TQPT}} = \sqrt{\lambda^2 + \mu^2} = 1.118$ meV. (a) Conductance false-color plot as a function of bias voltage V and Zeeman field V_z, with the fixed tunneling barrier height at $E_{\text{barrier}} = 10$ meV. (b) Conductance false-color plot as a function of bias voltage V and tunneling barrier height E_{barrier}, with the fixed Zeeman field at $V_z = 1.5$ meV. (c) Lowest-lying wave-function probability density $|\Psi|^2$ as a function of nanowire position x, with fixed $V_z = 1.5$ meV and $E_{\text{barrier}} = 10$ meV. (d) Quality factor F as a function of temperature T for three different tolerance factors ϵ, with the fixed $V_z = 1.5$ meV. The inset figure gives an overall trend starting from $T = 0$. At $T = 10$ mK, $F = 3.25$ for $\epsilon = 0.05$. At $T = 20$ mK, $F = 2.74$ for $\epsilon = 0.1$. (e) Conductance linecuts as a function of Zeeman field V_z for three different bias voltages V_{bias}, with the fixed $E_{\text{barrier}} = 10$ meV. The black dashed line marks $V_z = 1.5$ meV. (f) Conductance linecuts as a function of tunneling barrier height E_{barrier} for three different bias voltages V_{bias}, with the fixed $V_z = 1.5$ meV. (g) Zero-bias conductance G_z as a function of normal-metal conductance G_N for five different temperatures T, with the fixed $V_z = 1.5$ meV. (h) Quality factor J as a function of temperature T for three different tolerance factors ϵ, with the fixed $E_{\text{barrier}} = 10$ meV.

ideal model is possibly not realizable at current experimental stage, the results in this sub-section will serve as a reference for the signatures of a topological superconductor.

As expected from the literature [53–56], we observe a nearly quantized ZBCP appearing above the TQPT field $V_z > V_{\text{TQPT}} = 1.118$ meV in Fig. 2.3(a), which shows the conductance at zero temperature as a false-color plot versus the bias voltage V and Zeeman field V_z. The topological origin of this ZBCP can be seen in Fig. 2.3(c), which shows the lowest-lying wave-function probabilities $|\Phi_{A,B}(x)|^2$ [see Sec. 2.1.3] at $V_z = 1.5$ meV$> V_{\text{TQPT}}$ [yellow dashed line in Fig. 2.3(a)]. The localized wave functions $|\Phi_{A,B}(x)|^2$ at opposite ends of the wire verify that the ZBCP at $V_z = 1.5$ meV comes from topological MZMs. However, the wave function is not accessible in a transport experiment in a nanowire. On the other hand, as discussed in the introduction and Sec. 2.2, the quantization of the ZBCP associated with a topological MZM should be robust to changes in the barrier height. This is consistent with Fig. 2.3(b), which shows the conductance false-color plot as a function of bias voltage V and tunneling barrier height E_{barrier} at the fixed Zeeman field $V_z = 1.5$ meV. The plot shows the strength of the MZM-based ZBCP remains widely constant as the tunnel barrier height E_{barrier} increases, while the width of the ZBCP decreases. This can be further confirmed by the linecuts obtained from Fig. 2.3(b) at $V_{\text{bias}} = 0$ that are shown in Fig. 2.3(f), where the zero-bias conductance G_z is found to drop by less than 5% from quantization. Fig. 2.3(f) also includes linecuts from Fig. 2.3(b) at $V_{\text{bias}} = \pm 0.2$ meV. In contrast to the robust G_z, these finite-bias linecuts, which may be interpreted as the normal-state conductance, change significantly with the tunnel barrier height E_{barrier}. In fact, the tunnel barrier height E_{barrier} cannot be obtained directly through experimental measurements because tunnel gates have lever arms that rely on complicated structures of capacitance. Meanwhile, the normal-state conductance G_N determined by Fig. 2.3(f) at $V_{\text{bias}} = \pm 0.2$ meV provides a way to

quantify the tunnel barrier height that is directly comparable to experiments. One subtlety that arises in SM systems is that the conductance at the non-zero bias voltages in Fig. 2.3(f) can be different in SM systems. This can be compensated by defining G_N to be the average between the conductances at $V_{\text{bias}} = \pm 0.2$ meV.

Therefore, to demonstrate a result directly compared to experiments, we plot G_z versus G_N in Fig. 2.3(g), while keeping $V_z = 1.5$ meV [yellow dashed line in Fig. 2.3(a)] to ensure the wire is in the topological SC phase. Consistent with our discussion in the previous paragraph about Fig. 2.3(f), we find that the ZBCP height does not change significantly as G_N is reduced at zero temperature $T = 0$. On the contrary, the results at finite temperature $T > 0$ obtained from Eq. (2.15) show that G_z goes to zero as G_N decreases, as expected from the discussion in Sec. 2.2. The results in Fig. 2.3(g) clearly show that the robustness of the quantized ZBCP to the tunnel barrier changes would be limited by the experimental temperature, even in the case of ideal MZMs. The degree of robustness of the ZBCP quantization over G_N can be characterized by the quality factor F defined in Sec. 2.2, where the "well-quantized" zero-bias conductance G_z lies within a tolerance factor ϵ. The plot of the quality factor F versus temperature as in Fig. 2.3(d) shows that while the quality factor F associated with MZMs can be quite large (i.e., more than 80 at $T = 0$), F decreases quite rapidly as the temperature T becomes comparable to the topological SC gap. The main figure in Fig. 2.3(d) is to show the detailed variations of F in the experimental temperature range from $T = 2$ mK to $T = 30$ mK. The inset figure starting from $T = 0$ gives an overall trend to show how sharply F decreases from zero temperature to finite temperature. Since we only want to demonstrate how sharp the change of F is by the temperature variations, the tick numbers in the inset figure are not crucial here. While the quantitative value of F increases as the tolerance factor ϵ increases, the qualitative behavior does not seem to be remarkably affected

by the value of ϵ.

ZBCPs associated with the ideal MZMs are expected to be robust to variations in the Zeeman field because MZMs arise in a topological SC phase. This is consistent with the result in Fig. 2.3(e), where we find that the zero-bias conductance (i.e., $V_{\text{bias}} = 0$) starts out low in the non-topological regime (i.e., $V_z < V_{\text{TQPT}}$), but then sharply grows into a quantized plateau for $V_z > V_{\text{TQPT}}$. Same as the robustness with respect to the tunnel barrier height seen in Fig. 2.3(f), the result in Fig. 2.3(e) shows that the ZBCP associated with a topological MZM are also quite robust to variations in the Zeeman potential. Based on the discussion in Sec. 2.2, this robustness can be quantified with the definition of parameter J, which is plotted as a function of temperature in Fig. 2.3(h). Similar to the quality factor F associated with tunnel gate robustness, the Zeeman-field quality factor J also decreases with temperature in a way that is qualitatively independent of the tolerance ϵ used in the calculations of J.

2.3.2 "Bad" ZBCP

Now we consider the quality factor of the"bad" ZBCPs, which arise from an inhomogeneous potential near the end of the nanowire as shown in Fig. 2.1(b,c). Such an inhomogeneous potential can lead to ZBCPs [62], which can even exhibit nearly quantized conductance [65]. Thus, it is interesting to analyze the robustness of the quantizated ZBCPs and see if the quality factors can distinguish between such ABSs that give rise to "bad" ZBCPs and the topological MZMs discussed in sub-section 2.3.1.

The conductance false-color plot in Fig. 2.4(a) based on the setup in Fig. 2.1(b) clearly shows that a pair of finite-energy conductance peaks merge together into a ZBCP, quite similar

to the topological result as in Fig. 2.3(a). Based on the ZBCP linecut shown in Fig. 2.4(e), we observe that unlike the ideal MZM case, the ZBCP below the TQPT at $V_z = 0.87$ meV [marked by the black dashed line in Fig. 2.4(e), or the yellow dashed line in Fig. 2.4(a)] is only near the quantized value $2e^2/h$. We can find that the ZBCP splitting for $V_z > 0.87$ meV as seen in Fig. 2.4(a) is very likely to cause the reduction of the ZBCP seen in Fig. 2.4(e). To study if the tunnel-gate robustness of MZMs seen in the last sub-section 2.3.1 applies to this nearly quantized ZBCP, we examine the ZBCP height as the tunnel barrier height varies. As in Fig. 2.4(b), the ZBCP height appears to remain nearly constant while the width of the ZBCP changes, which is quite similar to the case of ideal MZMs. However, a closer checkup on the quantization using the linecut of $V_{\text{bias}} = 0$ shown in Fig. 2.4(f) demonstrates that the ZBCP height at $V_z = 0.87$ meV varies by a substantial amount as the tunnel barrier is changed. This huge variation can also be observed by plotting the ZBCP height versus the normal-state conductance shown in Fig. 2.4(g). Contrary to the case of the ideal MZM, the ZBCP height overshoots the quantized value at low temperatures when the normal-state conductance G_N small. This explains why the value of the quality factor F shown in Fig. 2.4(d) is relatively small compared to the topological case. The quality factor F for $\epsilon = 0.05$ at 10 mK in Fig. 2.4(d) is below 1.5. Interestingly, the quality factor F turns out to be quite large when $\epsilon = 0.2$, which makes sense based on the fact that the conductance G_z in Fig. 2.4(g) remains close to quantized to some extent. These observations along with the small ZBCP splitting seen in Fig. 2.4(a) can be understood by the low-energy wave functions decomposed in terms of Majorana basis shown in Fig. 2.4(c). We can confirm that the system is non-topological because both Majorana components of the wave functions are strongly overlapping at the same end. However, one of the components has a stronger spatial modulation, which means it has a strong weight at a different Fermi level. This suppresses the

overlap between the two states and ensures that only one of the states can couple strongly to the lead, explaining the observations made about Fig. 2.4(a) and Fig. 2.4(g). Given the ZBCP splitting observed in Fig. 2.4(a), the ZBCP quantization in Fig. 2.4(e) can only survive over a rather narrow range of Zeeman field V_z, which consequently leads to the relatively smaller values of the quality factor J seen in Fig. 2.4(h) compared to the topological case.

Fig. 2.5 that shows a "bad" ZBCP comes from another inhomogeneous potential configuration as in Fig. 2.1(c). While the ZBCPs shown in Fig. 2.5(a) are qualitatively similar to the "bad" ZBCP in Fig. 2.4(a), the quantization of the ZBCP at $V_z = 0.9$ meV, based on Figs. 2.5(b,d,e,f,g), appears to be more robust compared to Fig. 2.4. In fact, relative to the previous "bad" ZBCP [Fig. 2.4(d)], the quality factor F in Fig. 2.5(d) at temperature of 20 mK and $\epsilon = 0.1$ is 1.79, closer to the value of 2.74 in the "good" case [see Fig. 2.3(d)]. This can be understood from the Majorana decomposition in Fig. 2.5(c) that shows a pair of partially-separated modes, which have been described as quasi-Majoranas [65]. Such separated segments between spatially-separated MZMs exhibit its own topological characteristics, which explains the high value of F in this "bad" ZBCP. The quality factor J shown in Fig. 2.5(h) also turns out to be intermediate between the "good" ZBCP shown in Fig.2.3(h) and the previous "bad" ZBCP shown in Fig. 2.4(h).

2.3.3 "Ugly" ZBCP

The last sets of results [Figs. 2.6-2.9] belong to the "ugly" scenario, where the disorder-induced random potential, as shown in Fig. 2.1(d), generates a ZBCP by chance. Such ZBCPs only show up in only a small proportion of disorder configurations with the same parameters. Figs. 2.6-2.9 show results that span the set of possibilities, but their occurrence is somewhat

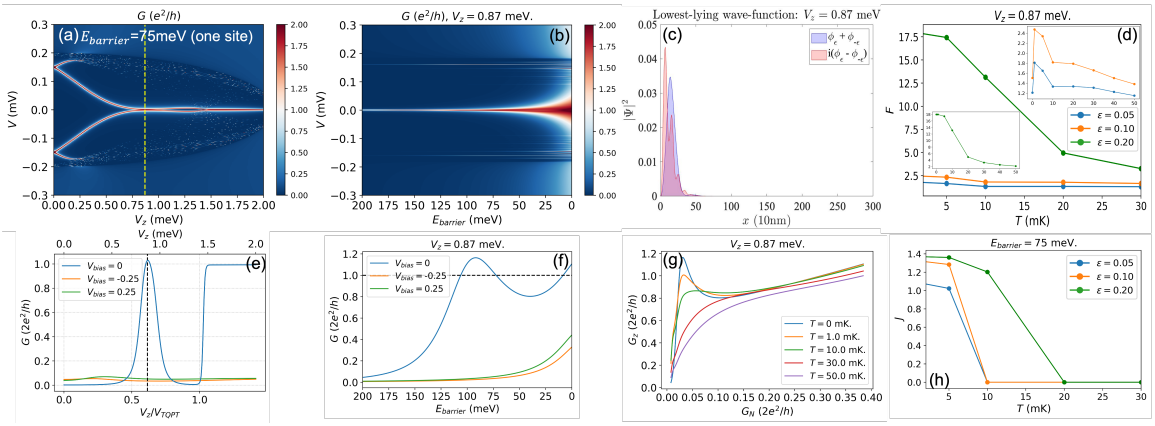

Figure 2.4: Numerical results for the "bad" ZBCP. Parameters: $\alpha = 2.51$ meV, $\Delta_0 = 0.2$ meV, $V_c = 2.1$ meV, $L = 3.0$ μm, $\mu = 1.0$ meV, $\lambda = 1.0$ meV, and $\gamma = 10^{-4}$ meV. The TQPT field is at $V_{\text{TQPT}} = \sqrt{\lambda^2 + \mu^2} = 1.414$ meV. The parameters for the quantum dot on the left end are: $V_D = 0.3$ meV and $\sigma_D = 0.15$ μm. (a) Conductance false-color plot as a function of bias voltage V and Zeeman field V_z, with the fixed tunneling barrier height at $E_{\text{barrier}} = 75$ meV. (b) Conductance false-color plot as a function of bias voltage V and tunneling barrier height E_{barrier}, with the fixed Zeeman field at $V_z = 0.87$ meV. (c) Lowest-lying wave-function probability density $|\Psi|^2$ as a function of nanowire position x, with fixed $V_z = 0.87$ meV and $E_{\text{barrier}} = 75$ meV. (d) Quality factor F as a function of temperature T for three different tolerance factors ϵ, with the fixed $V_z = 0.87$ meV. The inset figure gives an overall trend starting from $T = 0$. At $T = 10$ mK, $F = 1.331$ for $\epsilon = 0.05$. At $T = 20$ mK, $F = 1.789$ for $\epsilon = 0.1$. (e) Conductance linecuts as a function of Zeeman field V_z for three different bias voltage V_{bias}, with the fixed $E_{\text{barrier}} = 75$ meV. The black dashed line marks $V_z = 0.87$ meV. (f) Conductance linecuts as a function of tunneling barrier height E_{barrier} for three different bias voltage V_{bias}, with the fixed $V_z = 0.87$ meV. (g) Zero-bias conductance G_z as a function of normal-metal conductance G_N for five different temperatures T, with the fixed $V_z = 0.87$ meV. (h) Quality factor J as a function of temperature T for three different tolerance factor ϵ, with the fixed $E_{\text{barrier}} = 75$ meV.

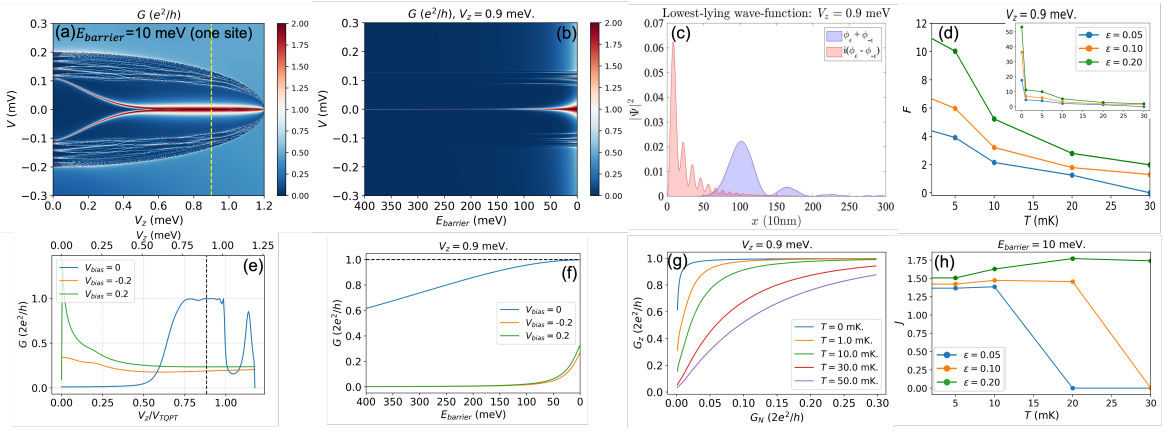

Figure 2.5: Numerical results for the "bad" ZBCP. Parameters: $\alpha = 2.5$ meV, $\Delta_0 = 0.2$ meV, $V_c = 1.2$ meV, $L = 3.0$ μm, $\mu = 1.0$ meV, $\lambda = 0.2$ meV, and $\gamma = 10^{-4}$ meV. The TQPT field is at $V_{\text{TQPT}} = \sqrt{\lambda^2 + \mu^2} = 1.020$ meV. The parameters for the inhomogeneous potential on the left end are: $V_D = 1.2$ meV and $\sigma_D = 0.4$ μm ($\sigma'_D = \sqrt{2} \times 0.4$ μm). (a) Conductance false-color plot as a function of bias voltage V and Zeeman field V_z, with the fixed tunneling barrier height at $E_{\text{barrier}} = 10$ meV. (b) Conductance false-color plot as a function of bias voltage V and tunneling barrier height E_{barrier}, with the fixed Zeeman field at $V_z = 0.9$ meV. (c) Lowest-lying wave-function probability density $|\Psi|^2$ as a function of nanowire position x, with fixed $V_z = 0.9$ meV and $E_{\text{barrier}} = 10$ meV. (d) Quality factor F as a function of temperature T for three different tolerance factors ϵ, with the fixed $V_z = 0.9$ meV. The inset figure gives an overall trend starting from $T = 0$. At $T = 10$ mK, $F = 2.148$ for $\epsilon = 0.05$. At $T = 20$ mK, $F = 1.785$ for $\epsilon = 0.1$. (e) Conductance linecuts as a function of Zeeman field V_z for three different bias voltage V_{bias}, with the fixed $E_{\text{barrier}} = 10$ meV. The black dashed line marks $V_z = 0.9$ meV. (f) Conductance linecuts as a function of tunneling barrier height E_{barrier} for three different bias voltage V_{bias}, with the fixed $V_z = 0.9$ meV. (g) Zero-bias conductance G_z as a function of normal-metal conductance G_N for five different temperatures T, with the fixed $V_z = 0.9$ meV. (h) Quality factor J as a function of temperature T for three different tolerance factor ϵ, with the fixed $E_{\text{barrier}} = 10$ meV.

rare. More generic results that do not show any quantization can be found in the Supplementary Material [90]. Figs. 2.6-2.9(a) show conductance peaks that may be interpreted as bound states or gap closure [94]. Specifically, even though ZBCPs appear in all these plots are below the nominal TQPT field (i.e.,$V_z/V_{\text{TQPT}} = 1$), Figs. 2.6-2.7(a) exhibit the gap closing feature merging into a ZBCP, similar to the way "good" and "bad" ZBCPs [i.e., Figs. 2.3-2.5(a)] does, while Figs. 2.8-2.9(a) show a separation between the ZBCP and the gap closing peaks. What makes the presented results in Figs. 2.6-2.9 so special is that all the ZBCPs in Figs. 2.6-2.9(a) appear to approach close to the quantized value $2e^2/h$ in various degrees, as one can see them clearly through the $V_{\text{bias}} = 0$ linecuts in Figs. 2.6-2.9(e). Fig. 2.6(e) shows a comparatively wide range of ZBCP plateau, but it deviates significantly from the quantized value, which gives rise to a vanishing quality factor J at $\epsilon = 0.05$ plotted in Fig. 2.6(h). Fig. 2.7(e) shows quantized ZBCPs limited to small ranges, with a strong variation of the zero-bias conductance value between the quantized peaks that give rise to a very low quality factor $J \simeq 1.2$ even when the tolerance factor is $\epsilon = 0.2$. Fig. 2.8(e) shows a nearly quantized plateau starting just slightly below the TQPT field (i.e., $V_z \leq V_{\text{TQPT}}$) and maintaining the quantization through the topological regime (i.e., $V_z > V_{\text{TQPT}}$) till the SC collapses. This can be interpreted as a result of a reduction of the actual TQPT field due to the disorder potential. While disorder are typically inclined to suppress the topological phase and increase V_{TQPT}, it could possibly reduce V_{TQPT} in rare fluctuations [108]. Finally, Fig. 2.9(e) exhibits a nearly quantized ZBCP, which is constrained to a small range of Zeeman field that cannot be categorized as a plateau.

Figs. 2.6-2.9(b) show the ZBCP height as the tunnel barrier height varies, with the Zeeman field fixed near the peak of the ZBCP [i.e., dashed line in Figs. 2.6-2.9(a)]. Figs. 2.6-2.7(b) show that the ZBCP splits as the peak is reduced, revealing that the ZBCP was indeed non-

topological, as can be confirmed from the Majorana decomposition shown in Figs. 2.6-2.7(c). However, these ZBCP splittings in Figs. 2.6-2.7(b) can merge and mimic zero-bias peaks when the finite-temperature effect kicks in, preventing ZBCPs to vary sharply as temperature changes, as in Figs. 2.6-2.7(g), which are opposite to what we have seen in Figs. 2.3-2.5(g). This is why we do not observe a sharp drop from the zero-temperature value of F in Figs. 2.6-2.7(d) to a finite-temperature one, and instead observe almost flat profiles of F values as the temperature changes for $\epsilon = 0.1$ and $\epsilon = 0.2$. Due to their non-topological nature of the ZBCPs, the quality factors F at $T = 0$ are much smaller (below 3) in Figs. 2.6-2.7(d) compared to other topological cases [Figs. 2.3, 2.5, 2.8, 2.9(d)]. With the apparent overlapping wave functions localized at one end in Fig. 2.6(c), the robustness of the ZBCP to changes in the tunnel barrier height cannot sustain at a practically measurable temperature of 20 mK, which is quantified to be $F = 0$ for $\epsilon = 0.05$, indicating the complete lack of quantization for this parameter. On the other hand, the partially-overlapping Majorana modes in Fig. 2.7(c), which exhibit a bit more topological character compared to the previous case, reflect this part on the quality factor F– the value is $F = 1.36$ at $T = 20$ mK for $\epsilon = 0.05$.

On the contrary, Fig. 2.8(b) shows the results of another disorder configuration, where a ZBCP remains unsplit even under changes of the tunnel barrier height. This can be verified with the Majorana decomposition plotted in Fig. 2.8(c), which shows a pair of separated Majoranas on opposite ends that indicate a topological state. The ZBCP plotted as a function of normal-state conductance G_N in Fig. 2.8(g) turns out to be quantized only at temperatures below 10 mK, as one can also check from the quality factor F in Fig. 2.8(d). This can be explained by the fact that the nearly quantized ZBCP in Fig. 2.8 occurs only slightly below the nominal TQPT field.

Finally, the ZBCP shown in Fig. 2.9(g) produced by another disorder configuration demon-

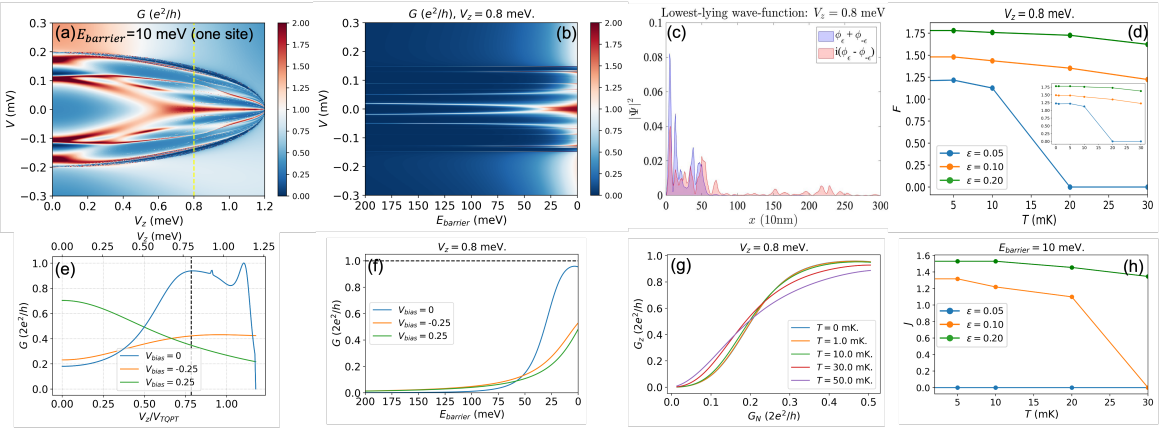

Figure 2.6: Numerical results for the "ugly" ZBCP. Parameters: $\alpha = 2.5$ meV, $\Delta_0 = 0.2$ meV, $V_c = 1.2$ meV, $L = 3.0$ μm, $\mu = 1.0$ meV, $\lambda = 0.2$ meV, and $\gamma = 10^{-4}$ meV. The TQPT field is at $V_{\text{TQPT}} = \sqrt{\lambda^2 + \mu^2} = 1.020$ meV. The parameters for the onsite random potential is: $\sigma_\mu = 2.0$ meV. (a) Conductance false-color plot as a function of bias voltage V and Zeeman field V_z, with the fixed tunneling barrier height at $E_{\text{barrier}} = 10$ meV. (b) Conductance false-color plot as a function of bias voltage V and tunneling barrier height E_{barrier}, with the fixed Zeeman field at $V_z = 0.8$ meV. (c) Lowest-lying wave-function probability density $|\Psi|^2$ as a function of nanowire position x, with fixed $V_z = 0.8$ meV and $E_{\text{barrier}} = 10$ meV. (d) Quality factor F as a function of temperature T for three different tolerance factors ϵ, with the fixed $V_z = 0.8$ meV. The inset figure gives an overall trend starting from $T = 0$. At $T = 10$ mK, $F = 1.126$ for $\epsilon = 0.05$. At $T = 20$ mK, $F = 1.352$ for $\epsilon = 0.1$. (e) Conductance linecuts as a function of Zeeman field V_z for three different bias voltage V_{bias}, with the fixed $E_{\text{barrier}} = 10$ meV. The black dashed line marks $V_z = 0.8$ meV. (f) Conductance linecuts as a function of tunneling barrier height E_{barrier} for three different bias voltage V_{bias}, with the fixed $V_z = 0.8$ meV. (g) Zero-bias conductance G_z as a function of normal-metal conductance G_N for five different temperatures T, with the fixed $V_z = 0.8$ meV. (h) Quality factor J as a function of temperature T for three different tolerance factor ϵ, with the fixed $E_{\text{barrier}} = 10$ meV.

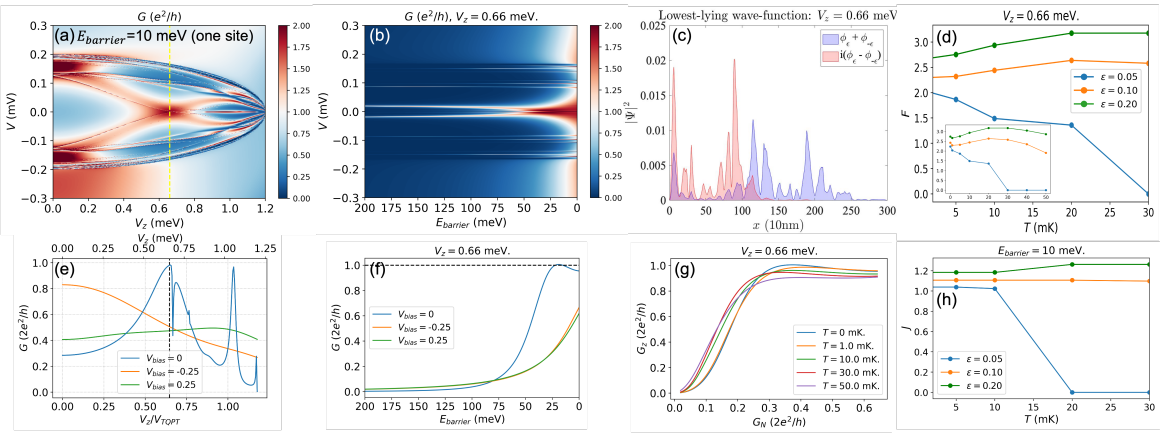

Figure 2.7: Numerical results for the "ugly" ZBCP. Parameters: $\alpha = 2.5$ meV, $\Delta_0 = 0.2$ meV, $V_c = 1.2$ meV, $L = 3.0$ μm, $\mu = 1.0$ meV, $\lambda = 0.2$ meV, and $\gamma = 10^{-4}$ meV. The TQPT field is at $V_{\text{TQPT}} = \sqrt{\lambda^2 + \mu^2} = 1.020$ meV. The parameters for the onsite random potential is: $\sigma_\mu = 2.0$ meV. (a) Conductance false-color plot as a function of bias voltage V and Zeeman field V_z, with the fixed tunneling barrier height at $E_{\text{barrier}} = 10$ meV. (b) Conductance false-color plot as a function of bias voltage V and tunneling barrier height E_{barrier}, with the fixed Zeeman field at $V_z = 0.66$ meV. (c) Lowest-lying wave-function probability density $|\Psi|^2$ as a function of nanowire position x, with fixed $V_z = 0.66$ meV and $E_{\text{barrier}} = 10$ meV. (d) Quality factor F as a function of temperature T for three different tolerance factors ϵ, with the fixed $V_z = 0.66$ meV. The inset figure gives an overall trend starting from $T = 0$. At $T = 10$ mK, $F = 1.490$ for $\epsilon = 0.05$. At $T = 20$ mK, $F = 2.638$ for $\epsilon = 0.1$. (e) Conductance linecuts as a function of Zeeman field V_z for three different bias voltage V_{bias}, with the fixed $E_{\text{barrier}} = 10$ meV. The black dashed line marks $V_z = 0.66$ meV. (f) Conductance linecuts as a function of tunneling barrier height E_{barrier} for three different bias voltage V_{bias}, with the fixed $V_z = 0.66$ meV. (g) Zero-bias conductance G_z as a function of normal-metal conductance G_N for five different temperatures T, with the fixed $V_z = 0.66$ meV. (h) Quality factor J as a function of temperature T for three different tolerance factor ϵ, with the fixed $E_{\text{barrier}} = 10$ meV.

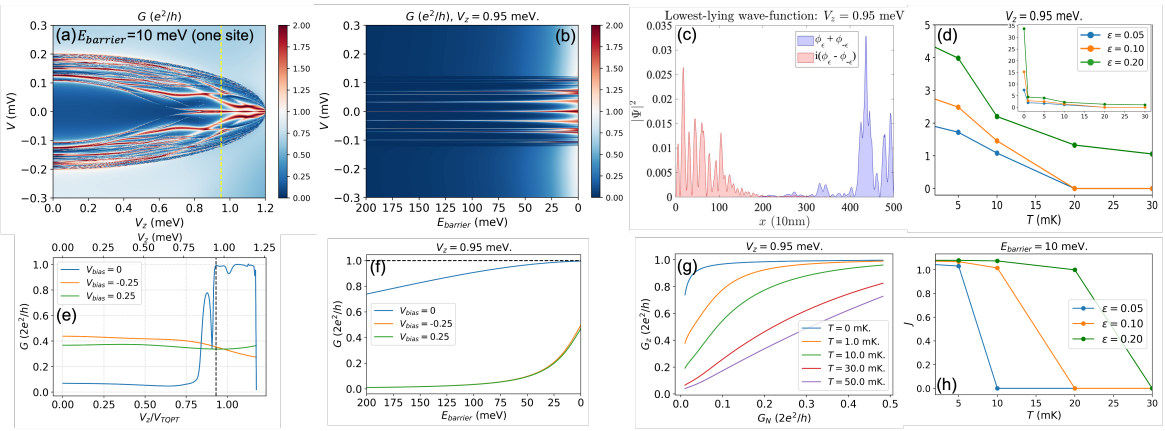

Figure 2.8: Numerical results for the "ugly" ZBCP. Parameters: $\alpha = 2.5$ meV, $\Delta_0 = 0.2$ meV, $V_c = 1.2$ meV, $L = 5.0$ μm, $\mu = 1.0$ meV, $\lambda = 0.2$ meV, and $\gamma = 10^{-4}$ meV. The TQPT field is at $V_{\text{TQPT}} = \sqrt{\lambda^2 + \mu^2} = 1.020$ meV. The parameters for the onsite random potential is: $\sigma_\mu = 1.0$ meV. (a) Conductance false-color plot as a function of bias voltage V and Zeeman field V_z, with the fixed tunneling barrier height at $E_{\text{barrier}} = 10$ meV. (b) Conductance false-color plot as a function of bias voltage V and tunneling barrier height E_{barrier}, with the fixed Zeeman field at $V_z = 0.95$ meV. (c) Lowest-lying wave-function probability density $|\Psi|^2$ as a function of nanowire position x, with fixed $V_z = 0.95$ meV and $E_{\text{barrier}} = 10$ meV. (d) Quality factor F as a function of temperature T for three different tolerance factors ϵ, with the fixed $V_z = 0.95$ meV. The inset figure gives an overall trend starting from $T = 0$. At $T = 10$ mK, $F = 1.084$ for $\epsilon = 0.05$. At $T = 20$ mK, $F = 0$ for $\epsilon = 0.1$. (e) Conductance linecuts as a function of Zeeman field V_z for three different bias voltage V_{bias}, with the fixed $E_{\text{barrier}} = 10$ meV. The black dashed line marks $V_z = 0.95$ meV. (f) Conductance linecuts as a function of tunneling barrier height E_{barrier} for three different bias voltage V_{bias}, with the fixed $V_z = 0.95$ meV. (g) Zero-bias conductance G_z as a function of normal-metal conductance G_N for five different temperatures T, with the fixed $V_z = 0.95$ meV. (h) Quality factor J as a function of temperature T for three different tolerance factor ϵ, with the fixed $E_{\text{barrier}} = 10$ meV.

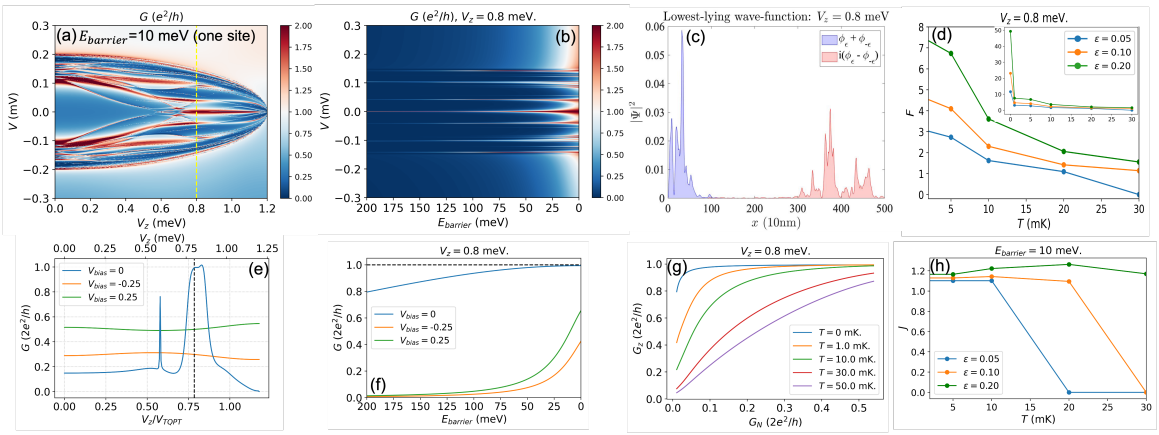

Figure 2.9: Numerical results for the "ugly" ZBCP. Parameters: $\alpha = 2.5$ meV, $\Delta_0 = 0.2$ meV, $V_c = 1.2$ meV, $L = 5.0$ μm, $\mu = 1.0$ meV, $\lambda = 0.2$ meV, and $\gamma = 10^{-4}$ meV. The TQPT field is at $V_{\text{TQPT}} = \sqrt{\lambda^2 + \mu^2} = 1.020$ meV. The parameters for the onsite random potential is: $\sigma_\mu = 2.0$ meV. (a) Conductance false-color plot as a function of bias voltage V and Zeeman field V_z, with the fixed tunneling barrier height at $E_{\text{barrier}} = 10$ meV. (b) Conductance false-color plot as a function of bias voltage V and tunneling barrier height E_{barrier}, with the fixed Zeeman field at $V_z = 0.8$ meV. (c) Lowest-lying wave-function probability density $|\Psi|^2$ as a function of nanowire position x, with fixed $V_z = 0.8$ meV and $E_{\text{barrier}} = 10$ meV. (d) Quality factor F as a function of temperature T for three different tolerance factors ϵ, with the fixed $V_z = 0.8$ meV. The inset figure gives an overall trend starting from $T = 0$. At $T = 10$ mK, $F = 1.624$ for $\epsilon = 0.05$. At $T = 20$ mK, $F = 1.419$ for $\epsilon = 0.1$. (e) Conductance linecuts as a function of Zeeman field V_z for three different bias voltage V_{bias}, with the fixed $E_{\text{barrier}} = 10$ meV. The black dashed line marks $V_z = 0.8$ meV. (f) Conductance linecuts as a function of tunneling barrier height E_{barrier} for three different bias voltage V_{bias}, with the fixed $V_z = 0.8$ meV. (g) Zero-bias conductance G_z as a function of normal-metal conductance G_N for five different temperatures T, with the fixed $V_z = 0.8$ meV. (h) Quality factor J as a function of temperature T for three different tolerance factor ϵ, with the fixed $E_{\text{barrier}} = 10$ meV.

strates a plateau that appears nearly as robust as the ideal topological ZBCP plateau shown in Fig. 2.3. This can be quantified by the quality factor F plotted in Fig. 2.9(d) at $T = 20$ mK, $\epsilon = 0.05$, which is close to that of the "good" ZBCP shown in Fig. 2.3. We can cross-check the nearly topological behavior seen from ZBCP height by the Majorana wave functions shown in Fig. 2.9(c), which show that the left component is spatially-separated from the right component. Therefore, the ZBCP in this parameter should be identified as topological. However, Fig. 2.9(c) also shows a disorder configuration where the right Majorana would not be accessible to tunneling, which will fail the test of end-to-end conductance correlation [81, 83, 87] between MZMs.

2.4 Discussion

2.4.1 Topological Characteristics from the quality factor F

Now we are going to analyze the quality factor F to see if it can allow us to distinguish the case of topological (i.e., "good") MZMs from the "bad" and "ugly" ZBCPs that can arise from quantum dots and disorder. If we focus on the quality factor F with the smallest value $\epsilon = 0.05$ and the lowest temperature $T \sim 0$ [i.e., insets in panel (d) of Figs. 2.3-2.9], the ideal MZM is predicted to reach an F in excess of 80, while this ideal value of the quality factors in the "bad" and the "ugly" cases remain below 20. Unfortunately, this ideal value for the quality factor F is not measurable in a finite-temperature experiment. Panel (d) of Figs. 2.3-2.9 show the quality factor over a more realistic range of temperatures. We see that even measurements performed on an ideal MZM at a low temperature of 10 mK, as one can see in Fig. 2.3(d), can only contribute to a quality factor of 3.3 for $\epsilon = 0.05$, which is much below the value of 84 at $T \sim 0$. Similarly, the quality factors F for the "bad" and the "ugly" cases are reduced to be below

2 at $T \sim 10$ mK for $\epsilon = 0.05$. The significant reduction of the quality factor at experimentally-accessible temperatures potentially could make it difficult to distinguish between topological and non-topological MZMs. However, the good-bad-ugly paradigm is more of a classification of ZBCPs based on microscopic models rather than their ultimate topological characteristics. More specifically, one can find that the wave functions plotted in Panel (c) reveal that many ZBCPs classified as "bad" and "ugly" based on models show spatially-separated MZM wave functions that allow them to be considered as topological. While this occurs in more than one result shown in Sec. 2.3, these are rare for the "bad" and "ugly" model, unless one tunes the parameters specifically to obtain a ZBCP stable with the change of magnetic field. One can find more generic examples of "bad" and "ugly" models with lower F values that do not demonstrate separated wave functions in the Supplementary Material [90]. In fact, among all the results presented in Sec. 2.3, only Figs. 2.4, 2.6 and 2.8 display truly non-topological results, which show a quality factor F below 1.5 for $\epsilon = 0.05$ at 10 mK. While the ideal topological "good" ZBCP in Fig. 2.3 gives $F = 3.25$ at 10 mK for $\epsilon = 0.05$, which is way above 1.5, a threshold of F to distinguish topological ZBCPs can be carefully determined by the statistical distribution of the F values for the non-topological "bad" and "ugly" cases (see the extended data in Supplementary Material [90]).

In Fig. 2.10(a), the blue dots are occurrence times for a case with a quality factor F_n larger than a given F value. The complementary cumulative distribution function (CCDF), as the red dashed curve in Fig. 2.10(a), is determined by fitting the blue dots with spline interpolation. The probability density function (PDF), as the blue curve in Fig. 2.10(b), can be numerically obtained by taking the derivative of the CCDF shown in Fig. 2.10(a). Fig. 2.10(a) shows that there is no non-topological case ("bad" and "ugly") that exhibits a quality factor F larger than 3, while the

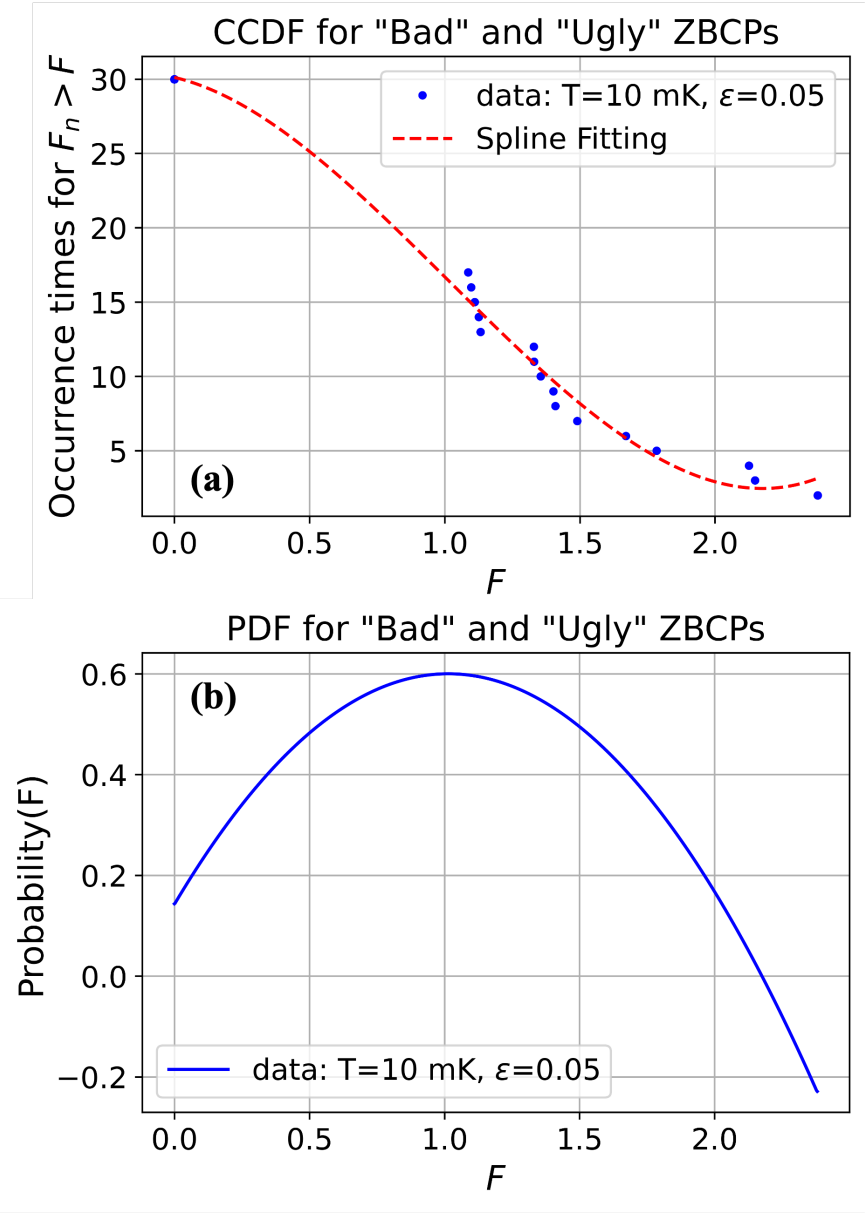

Figure 2.10: Statistical histogram for "bad" and "ugly" ZBCPs at $T = 10$ mK and $\epsilon = 0.05$. (a) Blue dots: number of cases whose quality values F_n (n denotes each case) are larger than a given F value on the x-axis. The data can be found in the Supplementary Material [90]. Red dashed curve: complementary cumulative distribution function (CCDF) is determined by fitting the blue dot data with spline interpolation. (b) Probability density function (PDF) is the (negative) derivative of the CCDF shown in (a).

occurence times for $F > 2$ is already rare. With the extended data of "good" ZBCPs, which all demonstrate $F > 3$ at $T = 10$ mK for $\epsilon = 0.05$ (summarized on the first page of the pdf file of the Supplementary Material [90]), the cumulative histogram for the trivial ZBCPs in Fig. 2.10(a) suggests a threshold of approximately $F = 3$ would be sufficient to separate topological and non-topological ZBCPs. In fact, while the data of $F < 1.5$ (at $T = 10$ mK for $\epsilon = 0.05$) demonstrate overlapping wave functions clearly, the data that linger above $F = 2.0$ in Fig. 2.10(a) demonstrate partially-separated quasi-Majoranas, which can be classified as between topological and non-topological. In short nanowires, which are most of the current experimental setups, MZMs appear as partially-separated quasi-Majoranas, which have been proposed to be able to implement braiding [65]. Nonetheless, quasi-Majoranas are non-topological in the sense that the two Majorana modes would not localize ideally at both ends, which will fail the examination of the end-to-end conductance correlation [83]. An example can be visualized in Fig. 2.5, which is labelled as a model of a "bad" ZBCP with a F value of 2.15 for $\epsilon = 0.05$ at $T = 10$ mK. Since Fig. 2.5(c) shows that the Majorana wave functions in this system are quite well-separated but inaccessible from the right end, this case would correspond to the quasi-Majorana scenario [65]. Because of the separated MZMs, one can interpret this scenario as having a short segment of a topological superconductor at one end of the wire.

The temperature criterion 10 mK discussed in the last paragraph may be relaxed to 20 mK if the tolerance factor ϵ associated with F is increased to $\epsilon = 0.1$. Similar to the way we determine a threshold of F at $T = 10$ mK for $\epsilon = 0.05$ to separate topological and non-topological ZBCPs, a threshold of $F = 2.5$ for $\epsilon = 0.1$ at $T = 20$ mK can be scrupulously determined by a combination of the quality factors of the ideal "good" ZBCPs from the extended data [90], and the statistical histogram in Fig. 2.11 from the extended non-topological "bad" and "ugly" data [90]. To get a

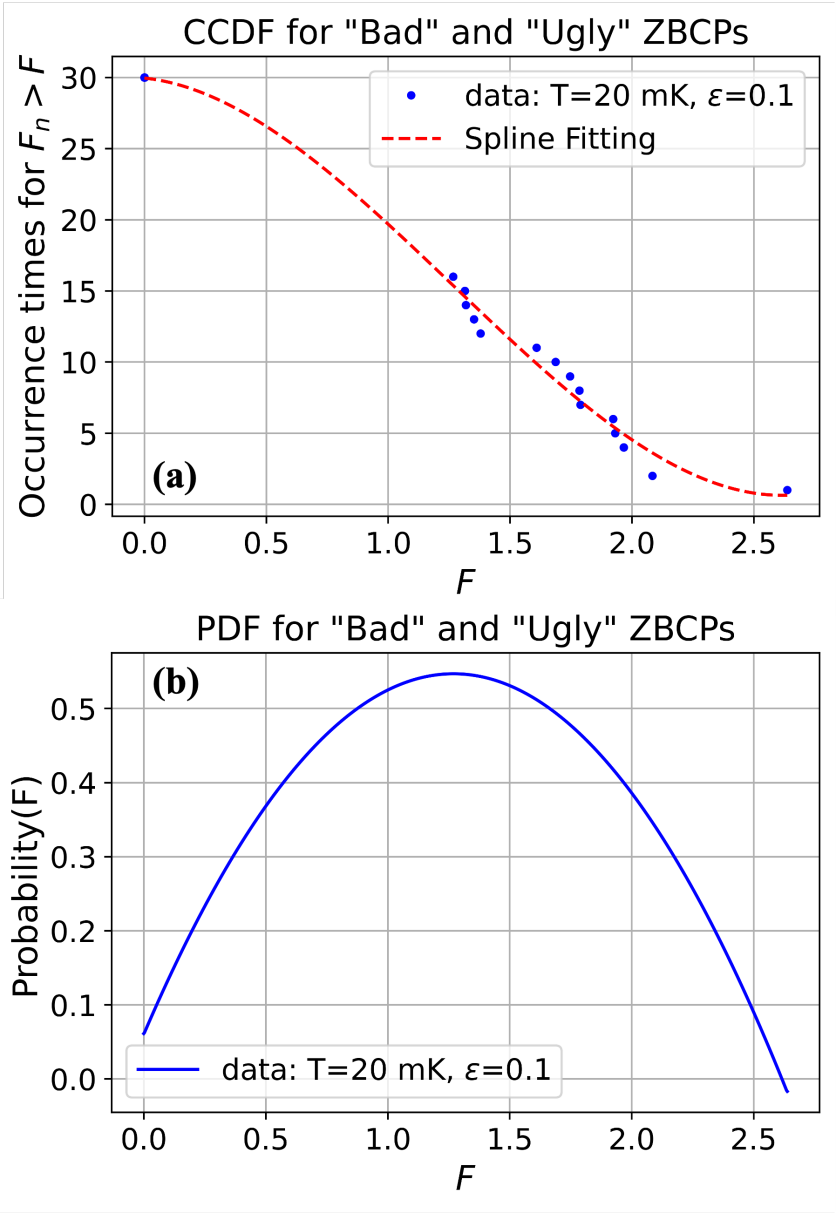

Figure 2.11: Statistical histogram for "bad" and "ugly" ZBCPs at $T = 20$ mK and $\epsilon = 0.1$. (a) Blue dots: number of cases whose quality values F_n (n denotes each case) are larger than a given F value on the x-axis. The data can be found in the Supplementary Material [90]. Red dashed curve: complementary cumulative distribution function (CCDF) is determined by fitting the blue dot data with spline interpolation. (b) Probability density function (PDF) is the (negative) derivative of the CCDF shown in (a).

sense of this distinction, one can find that the ideal MZM shown in Fig. 2.3 is associated with an F of 2.74 for $\epsilon = 0.1$ at $T = 20$ mK, while all the non-topological cases are below 1.8, except for Fig. 2.7. In fact, we particularly present the "ugly" ZBCP results in Fig. 2.7, which is associated with a value of $F = 2.64$ for $\epsilon = 0.1$ at $T = 20$ mK, to show an example that an "ugly" ZBCP could produce a quality factor F larger than the threshold to be mistakenly distinguished as topological, but does not possess topological characters based on its Majorana-decomposed wave functions (as we discussed in Sec. 2.3.3). Fig. 2.7 is also the only one case among the 30 non-topological ZBCPs that shows up with $F > 2.5$ in Fig. 2.11(a). While this false-positive case only accounts 3.3% of our simulated non-topological samples [90], giving rise to a precision rate of 96.7% to distinguish the non-topological ZBCPs from topological ZBCPs, the value of 96.7% is actually a conservative estimation in the sense that we dropped out hundreds of "ugly" cases that do not reach quantization (say $F = 0$ even for $\epsilon = 0.2$) at all and purposely kept as many as we can the "bad" and "ugly" cases that show quantization similar to the ones from MZMs. Therefore, we believe the precision rate to identify non-topological ZBCPs can be higher than 96.7%, which is already a high proportion. Similar to Fig. 2.10(a), one can find those cases [90] associated with $F \simeq 2$ in Fig. 2.11(a) would exhibit partially-separated wave functions, known as quasi-Majoranas, while those cases associated with $F < 1.5$ mostly show overlapping wave functions, which are clearly non-topological. So the quality factor F indeed demonstrate the quality of MZMs of different levels gradually. A high value of F is seen as being associated with a MZM of good quality with sufficient confidence statistically.

This distinction between MZMs and quasi-Majoranas (or ABSs) is further blurred at $\epsilon = 0.2$ where Figs. 2.3-2.5 show an F value of approximately 5 at $T = 20$ mK. However, raising this tolerance ϵ seems to increase the separation between these MZMs/quasi-Majoranas and the

"ugly" ZBCPs. In fact, the threshold for the quality factor F depends on several factors, including the topological superconducting gap E_g (which can be enhanced by increasing the spin-orbit coupling constant α), nanowire length L, temperature T, and tolerance factor ϵ. For a system with large E_g and long L, the MZMs produced in the nanowires are expected to be quite robust against changes in the tunnel barrier height, so we can pick a high value of threshold, below which would be the non-topological cases. As the temperature T is tuned lower, the MZM-induced ZBCPs will become closer to the ideal quantized plateau, giving a high value of F [as we can see in Fig. 2.3], while the ZBCPs induced from trivial subgap states can barely do the same [as we can see in Fig. 2.4-2.9]. The difference of F values between topological and trivial ZBCPs can even become two orders of magnitude as the temperature approaches absolute zero. In this case, it is also easy to choose a higher value of threshold to separate the topological and non-topological ZBCPs. The tolerance factor ϵ can be viewed as the sensitivity to the quantization plateau. A smaller value of ϵ is only applicable when the ZBCP is closer to quantization, which can be realized by increasing the topological superconducting gap E_g, increasing the nanowire length L, and/or lowering the temperature T. Under these conditions, the gap of F values between the topological and non-topological scenarios can be large, which makes us easy to choose the threshold of F. In contrast, when the experimental conditions do not facilitate the production of MZMs, the distinction of the F values between topological case and trivial case can be comparatively minor, making it hard for choosing the threshold. This issue can also be seen from the false-positive case popping up in Fig. 2.11 under the condition of $T = 20$ mK with $\epsilon = 0.1$ with a threshold of 2.5, while this issue is completely diminished in Fig. 2.10 under the condition of $T = 10$ mK with $\epsilon = 0.05$ with a threshold of 3.0.

Among the "bad" and "ugly" results we present, the ones that demonstrate some kind of

topological character (i.e., separated Majorana decomposed wave functions), such as Figs. 2.5, 2.8, and 2.9, in fact do not pass the thresholds determined by the statistical histograms in Figs. 2.10-2.11. We can interpret these as the topological ZBCPs that cannot maintain their topological character in the finite-temperature environment when quantum dots or disorders interfere with the system. Since the threshold we set is to rigorously distinguish the ZBCP induced by MZMs, a measured value of F higher than the threshold indicates a high probability ($> 95\%$) of getting a topological ZBCP. On the other hand, a value of F below the threshold does not tell the scenario – it could be topological or non-topological. Therefore, our proposed quality factor F can help filter out those ZBCPs with F values larger than the threshold as potential MZM candidates to proceed with other Majorana examinations.

To apply this new metric F to the experiments, we estimate the quality factor F values through the recalibrated quantized conductance data from Zhang et al. [52], which is our motivation to study the robustness of quantized ZBCPs. Under the experimental temperature 20 mK, the quantized plateau in Fig. 4(b) of Zhang et al's paper [52] gives rise to $F \simeq 1.16$ for $\epsilon = 0.1$. Their extra data as shown in Fig. G2(b) also exhibits a quality factor value of $F \sim 1$ (for $\epsilon = 0.1$ at 20 mK), which are way below $F = 2.5$ as the suggested threshold in our simulation. These low values of F demonstrating fragile quantization indicate the ZBCPs shown in Zhang et al's paper [44, 52] are very likely arising from non-topological subgap states.

2.4.2 Decoherence rate based on the quality factor F

Based on the analysis and estimations in the previous sub-section, it might be experimentally challenging to distinguish MZMs from other non-topological "bad" and "ugly" ZBCPs. This

leads to doubts about our motivation of using transport to make this distinction, as opposed to time-domain techniques that work directly with nanowires in qubit configuration [109]. Therefore, it is critical for us to argue here that the quality factor F can provide a preliminary estimate of the decoherence rate for the MZM or the quasi-Majorana as a qubit. Alternatively, the best quality factor we can obtain from a class of Majorana device provides an estimated bound of the coherence time for a Majorana qubit based on such devices. To proceed this quote, firstly, we assume the nanowire is long enough such that the overlap of Majoranas is smaller than the measured temperature. In this limit, the estimated bit-flip rate of a topological qubit depends on the topological SC gap E_g and the temperature T according to the relation $Te^{-E_g/2T}$ [5]. Note that the precision of quantization for the MZM-induced ZBCP is limited by the same ratio E_g/T. In detail, the width of ZBCP at $T = 0$, denoted by Γ in Eq. (2.19), is proportional to the normal-state conductance $G_N \propto \Gamma$ [110]. Thus, the quality factor F can be approximated as

$$F = \frac{G_{N,2}}{G_{N,1}} \sim \frac{\Gamma_{\text{max}}}{\Gamma_{\text{min}}}. \tag{2.20}$$

For lower normal-state conductance, G_N, the conductance can be quantized only if $\Gamma_{\text{min}} \geq T$. The largest Γ, for which the ZBCP can be approximated as Lorentzian shape based on Eq. (2.19), has the same order of the topological gap, i.e., $\Gamma_{\text{max}} \sim E_g$. Based on the above arguments, the quality factor for a ZBCP in a long Majorana wire with a topological gap E_g at temperature T is estimated to be $F \sim E_g/T$.

Given the analysis in the previous sub-section, we conclude that among the types of models studied here, the quality factor F needs to be greater than 2 to be confidently identified as a topological MZM. Assuming a qubit is build from an MZM of this quality, using the estimated

decoherence rate quoted earlier, we would conclude a rate of 56 MHz at 20 mK. Compared to most non-topological qubits at current stage, this decoherence rate is already higher, which means the threshold F needs to be higher than the one that can already convincingly distinguish a MZM-based quantized ZBCP.

2.4.3 Multi-channel effects

For the simplicity of presentation, we apply the single-channel semiconductor nanowire model for simulation. Nonetheless, based on the analysis of TSC conductance probed through a QPC [56], the quantization of the measured conductance entirely depends on the number of channels in the tunnel contact, rather than the number of channels in the nanowire. In fact, even if the number of channels in the TSC nanowire is unknown, the quantization of the conductance is still measurable as long as the tunnel contact is gated by a tunnel barrier. Typically, the tunnel barrier is tuned to be high, which leads the normal-state conductance to be below $2e^2/h$ accordingly [52]. This implies that the QPC is likely to be single-channel. It is because the nanowire mobilities are large enough (i.e., ballistic transport) while the tunnel barrier is adiabatic potential (i.e., smooth Gaussian potential with the width larger than Landau Fermi wavelength) so as to show a few quantized steps as a function of gate voltage [111]. Thus, even if the contacts of the tunnel barrier are multi-channel, the transmission eigenvalues through the tunnel barrier are probably quite small for the higher-order channels. Still, the small transmission in the higher-order channels may cause the topological conductance a small deviation from quantization, which could be crucial to explain observed conductances above $2e^2/h$ [38, 52]. In this sense, our analysis on the relation between the quality factor and the topological quantum computing (TQC), as discussed

in the last seb-section, seems to have a limitation. Nevertheless, this can be avoided by making sure the MZM conductance is measured through a clean segment of semiconductor nanowire, which can be controlled to be single-channel. This should be feasible because clear conductance steps through non-SC segments of nanowire can be demonstrated [111, 112].

2.4.4 Characterizing MZMs based on J

Contrary to the quality factor F, which can be extremely large, the quality factor J is limited. From the numerical results in Sec. 2.3, J values are all below 2.1, which are comparatively lower when F values can reach almost 50 in the zero-temperature limit. In general cases of "good" ZBCPs, J values could even be lower than those from "bad" or "ugly" ZBCPs when the Majorana splitting oscillations dominate. The best value of J we can get for the "good" ZBCP is V_c/V_{TQPT} when the nanowire is longer than the SC coherence length and therefore the Majorana splitting is suppressed. The quality factor J in this case turns to be contrained by how soon the SC gap collapses and how late the system enters the topological regime. There is not much significant difference for the J values between the "good" ZBCPs and "bad" or "ugly" ZBCPs. Therefore, based on the models studied here, the robustness to the Zeeman field is difficult to use for characterizing MZMs. However, a low value of the quality factor J suggests a topological gap that may be too small for practical use.

2.5 Summary

To sum up, we have studied the robustness of the ZBCP quantization to the variations of the tunnel barrier height and Zeeman field, which can be a new way to separate topological MZMs

from trivial "bad" and "ugly" ZBCPs associated with subgap ABSs and random disorder, respectively. This is motivated by the robustness nature of "good" ZBCPs associated with MZMs. In addition, contrary to the experimentally-inaccessible wave functions, the quality factors obtained from the tunneling experimental results can show the topological character of the ZBCP. While the quality factor J, which quantifies the quantized plateau over Zeeman field, is not a particularly strong indicator to show the topological character of the system, it can be a useful diagnostic to avoid a small topological gap. On the other hand, the dimensionless quality factor F, which takes on values $\gg 80$ only in the topological phase at zero temperature, can sharply quantify the stability of the ZBCP to changes in normal-state conductance. In contrast, non-topological systems with strongly overlapping MZMs only show quantized plateau over a very narrow range of normal-state conductance G_N, which typically leads to quality factors F less than 10 at zero temperature. Therefore, the value of quality factor F at low temperature is a rather strong indicator of the topological character of the system. Unfortunately, the values of F drop very quickly as soon as the finite-temperature effect kicks in such that it becomes smaller even for the "good" ZBCP. So the use of F to distinguish MZMs from trivial ZBCPs is restricted by the current experimental temperature limit ~ 20 mK. Though the results of finite temperature are kind of disappointing, they do not relegate the quality factor F to limbo. In fact, the quality factor F could still play a single diagnostic for identifying emergent MZMs if the topological gap can be enhanced with the improved material fabrication. Another challenge that threatens the current experimentally-observed quantization is the need to design the tunnel barrier contact carefully so the contact is ensured to only hold a single channel. According to Wimmer *et al.* [56], only when the tunnel contact is single-channel can the measured conductance from TSC be guaranteed to reach quantization $2e^2/h$ at zero temperature. This is very likely the reason why robust

quantized ZBCPs of MZMs are still elusive. Once these design, gap, and temperature constraints are resolved, a ZBCP with a quality factor F greater than the threshold should tell a ZBCP as a topological MZM.

Chapter 3: Presence versus Absence of End-to-end Non-local Conductance Correlation

Based on the fundamental theory of the MZM, the appearance of ZBCP in the topological regime is an important basic hallmark for the MZM. Unfortunately, it is later found that the topologically-trivial ABSs could also produce ZBCPs, making the signature of ZBCP not unique for the topological MZMs. On the other hand, as we illustrated in Chapter. 2, non-topological subgap states can also mimic the quantization of ZBCPs, a signature of MZMs at zero temperature, with appropriate fine-tuning. All these complications brought by the unintentional QD-induced ABSs have obscured the signatures for the existence of MZMs. One may propose to focus on the signatures of MZMs only in the topological regime. However, the TQPT field which separates the topological regime from the trivial regime is typically too weak to be measured. This is why making a distinction between MZMs and ABSs is tremendously important in search of Majoranas.

In this chapter, we utilize the fundamental non-local nature of MZMs [2, 81] to establish a protocol that could decisively distinguish between ZBCPs arising from MZMs and ABSs. Motivated by the three-terminal setup Deng *et al.* [36] carried out tunnel conductance measurements, we propose that by carrying out the tunnel conductance measurements from both ends of the wire and comparing the two sets of tunneling data, the topological character of ZBCPs can be identi-

fied. The ZBCPs arising from MZMs (or ABSs) will be correlated (or uncorrelated) between the two ends, meaning if the ZBCPs show up from both ends, it is likely to be associated with MZMs, whereas if the ZBCP only exists at one end but not the other, then it is likely to come from ABS. We will demonstrate extensive numerical simulations to stress that the presence of this end-to-end conductance correlation is associated with the presence of MZMs, while the absence of the end-to-end conductance correlation is most likely to be come from the ABS localized at one end.

For completeness of the study on the same three-terminal setup, we also calculate the cross conductance in the nanowire with and without the embedded QD. Such a measurement has been proposed a way to detect the TQPT [82]. We suggest that by combining the conductance correlation test and cross conductance measurement, one should be able to distinguish the MZM-induced ZBCPs from ABS-induced ZBCPs.

3.1 Model

In this chapter, we consider a hybrid superconductor-semiconductor nanowire, with an external quantum dot (QD) embedded near the left end of the wire, as shown in Fig. 3.1. One can find the same protocol to numerically calculate the QPC differential conductance $G = dI/dV$, wave functions, and energy spectrum, as we already illustrated in detail in Sec. 2.1, except that now the spatial arrangement of the Hamiltonian is a bit modified. As in Fig. 3.1, from the leftmost end, it starts with H_{lead} (described by Eq. (2.7)), and then H_{barrier} (the tunnel barrier is described by Eq. (2.8)), H_{QD} (described by Eq. (2.2), with $V(x)$ described as Eq. (3.1)), H_{NW} (described

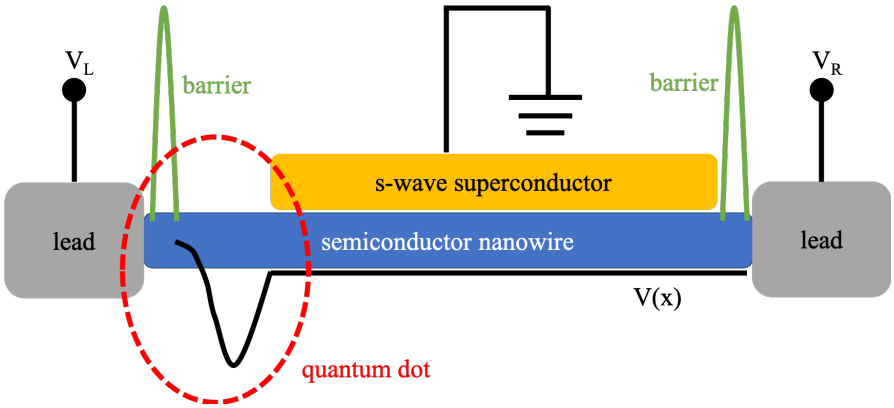

Figure 3.1: Schematic plot of the hybrid structures composed of leads on both sides. This setup is basically motivated by Deng *et al.* experiment [36]. The semiconductor nanowire is covered by a parent s-wave superconductor, except for the part embedded by the quantum dot (shown in the red dashed line). Note that the quantum dot is strongly coupled to the nanowire, which may not exhibit Coulomb blockade effect. The leads used to measure the conductance are set on both sides, which also induce the tunnel barriers (green parts). The differential conductances calculated in this paper are probed either from the left lead or from the right lead.

by Eq. (2.2)), H_{barrier}, and H_{lead} to the right. The QD potential in our numerics is of the form

$$V_{\text{QD}}(x) = V_D \cos\left(\frac{3\pi x}{2l_D}\right), \tag{3.1}$$

where l_D only counts a fraction of the total nanowire length L. In fact, the precise form of the QD potential is irrelevant for our consideration because no qualitative conclusion depends on these details.

Similar to Chapter 2, we calculate the Majorana-decomposed wave function probabilities $|\Phi_A(x)|^2$ and $|\Phi_B(x)|^2$ (which follows by Eq. (2.17) and Eq. (2.18)) over the spatial space in the nanowire, by first summing over the inner degrees of freedom (particle-hole space and spin space). If $|\Phi_A(x)|$ and $|\Phi_B(x)|^2$ are localized separately at each end of the wire, then they are

characterized as an MZM pair. In this case, the ZBCPs we observe in the corresponding conductance plot come from MZMs. In contrast, if $|\Phi_A(x)|$ and $|\Phi_B(x)|^2$ overlap with each other, possibly only localized on one end of the wire, then the observed ZBCP arises from ABS. It is also possible that the nanowire is not long enough such that the tails of the two Majorana bound states (MBSs) at each end overlap with each other pretty much. In this case, we cannot have the topological MZMs. Only the well-separated MBSs without overlapping can facilitate the existence of MZMs. This also means one zero-energy ABS can be considered to be composed of double MBS modes which overlap considerably in the real space. Therefore, one can theoretically distinguish the sources of ZBCPs by just comparing the behaviors of wave functions on both ends of the wire. However, as mentioned in Chapter 2, while the wave functions are easy to theoretically calculated, there is no way to access the wave functions in the experiments. The wave function we present in our numerical results in this chapter are mainly for verifying the topological character of the corresponding calculated ZBCP, which is typical measured in the experiments to search for the MZM.

The parameters in all of our numerical results (Figs. 3.2-3.4) are chosen as follows: the effective mass is $m^* = 0.015m_e$, nanowire length $L = 5$ μm, induced SC gap $\Delta_0 = 0.9$ meV, spin-orbit coupling $\alpha_R = 0.5$ eV$\mathring{A}$. The gate voltage in the lead is $E_{\text{lead}} = -25$ meV, with the induced tunnel barrier height $E_{\text{barrier}} = 10$ meV, and the barrier length $l_{\text{barrier}} = 20$ nm. The strength of the confinement potential in the quantum dot is $V_D = 4$ meV, with length $l_D = 0.3$ μm. The temperature, which smears the conductance profile by thermally broadening all sharp features, is set at 0.02 meV. The phenomenological dissipation parameter is $\Gamma = 0.01$ meV. The above parameters will be fixed throughout all our results, and other tuning parameters, including the chemical potential μ, the Zeeman energy V_z, the SC gap collapsing point V_c, along with the

TQPT field $V_{\text{TQPT}} = \sqrt{\mu^2 + \Delta_0^2}$, will be provided in the captions of the figures. In our presented results of this chapter, we do not include the self-energy, i.e., $\lambda = 0$ in Eq. (2.3). Nevertheless, the presence of non-local correlation that is associated with MZM-induced ZBCPs should not qualitatively depend on the strength of self-energy coupling, as one can find the extensive self-energy results in the appendix of this work [83]. Our strategy to distinguish MZMs from ABSs is valid no matter self-energy effect is included or not. Similar for the parameters Γ and V_c – they are nonessential aspects for our theory with respect to the MZM/ABS distinction. We include them in our simulation to make the results realistic, not because they are necessary for the main point of end-to-end ZBCP corralations being stressed in this work.

3.2 Numerical Results: Local Conductance from each end

The main idea to distinguish between MZMs and ABSs in this work is quite fundamental: ZBCP associated with the topological MZM should exhibit non-local correlations because topological MZMs always appear in pairs at both ends of the wire, which contribute to ZBCPs at each end. On the contrary, an ABS is a non-topological fermionic bound state arbitrarily localized near one or the other end of the wire. Moreover, the ZBCP associated with the ABS only shows up when the tunneling end connects to the relevant ABS localized at the same end. So the ABS-induced ZBCPs do not show up at both ends of the wire simultaneously and thus should have no non-local correlatioins. Since the regime where the ABS sticks to zero-energy depends on a lot of different parameters and therefore kind of random, we present extensive numerical results to touch various scenarios for complete discussion. Particularly, we will vary the chemical potential for each simulated set since the chemical potential can determine the nominal TQPT field, which

divide the trivial regime and the topological regime.

In Fig. 3.2, we show an example (chemical potential $\mu = 1.0$ meV) where there is a pair of ABSs that approach and stick to near zero energy near $V_{\text{TQPT}} = 1.35$ meV, but the Zeeman field range where the ABSs are zero-energy is very limited, as one can see from the energy spectrum in Fig. 3.2(a). Above V_{TQPT}, the expected zero-energy MZMs appear. The corresponding conductance spectra probed by the left lead and the right lead are shown in Fig. 3.2(b) and Fig. 3.2(c), respectively. The dominant ZBCPs only show up above the TQPT field (black dashed line) from both ends, which are consistent with the spectrum in Fig. 3.2(a). One thing to pay attention to in these conductance spectra [Figs. 3.2(b)(c)] is that the conductance pattern that appears to follow the energy pattern induced from ABSs in Fig. 3.2(a) below V_{TQPT} only shows up in the conductance from the left end, as in Fig. 3.2(b). It is clearly because the QD is embedded near the left end of the wire (as shown in Fig. 3.1), which leads to the ABS localized on the left end. On the contrary, the conductance probed from the right end does not demonstrate this subgap feature. Even though the conductance profiles in Fig. 3.2(b) and Fig. 3.2(c) appear quite unlike, the ZBCPs probed from both the left and the right ends show up at the same Zeeman field. This is because both ZBCPs arise from MZMs, while the ABSs exist in this parameter regime do not stick to zero energy [see the subgap states below V_{TQPT} in Fig. 3.2(a)]. One can examine the conductance further by taking the linecuts of conductance from both ends at the same Zeeman field in Figs. 3.2(b)(c) and presenting them in the same plot, such as Fig. 3.2(d) for $V_z = 2.0$ meV. Obviously, despite that the heights of the ZBCPs at the left and the right ends have a big difference, the ZBCPs appear to be correlated. As the Zeeman field where the conductance linecuts are checked increases (such as Fig. 3.2(e) at $V_z = 3.0$ meV), the ZBCP heights from both ends become comparable. In this case where the chemical potential is small, the zero-energy states

come from MZMs appearing at each end of the wire. This can be confirmed from an examination of the lowerst-lying wave functions, which should display the near zero-energy states, both when V_z is close to V_{TQPT} [as Fig. 3.2(f)] and when V_z is deeper into the topological regime [as Fig. 3.2(g)]. Both sets of linecuts show the Majorana-decomposed wave functions localized at each end with finite weight.

The situation changes qualitatively when the chemical potential is raised to $\mu = 5.0$ meV. As shown in the energy spectrum [Fig. 3.3(a)], now even ABSs appearing below V_{TQPT} (black dashed line) have several chances to stick to zero energy. In this case, the ZBCP on the left end [Fig. 3.3(b)] also shows up in the trivial regime ($V_z < V_{\text{TQPT}}$), while the ZBCP on the right end [Fig. 3.3(c)] does not show up until the Zeeman field is in the vicinity of V_{TQPT}. The linecuts of the conductance in the trivial regime at $V_z = 1.9$ meV [yellow dashed lines in Figs. 3.3(b)(c)] exhibit a dramatic difference between the left end and the right end, as one can see in Fig. 3.3(d). The linecut from the left end shows an obvious ZBCP, while the one from the right end only shows strong gaps located near $V = \pm 0.5$ meV. However, as the Zeeman field is increased to $V_z = 6.0$ meV [purple dashed lines in Figs. 3.3(b)(c)], ZBCPs with comparable height appear on both ends [Fig. 3.3(e)], which is expected since $V_z = 6.0$ meV is in the topological regime. The origin of the ZBCP on the left end in Fig. 3.3(d) can be cross-checked with the corresponding wave functions as shown in Fig. 3.3(f). We can see the Majorana-decomposed wave functions are entirely localized ar the left end, which is the same way as ABSs exhibit. In contrast, the wave functions are separated on each end of the wire at a higher Zeeman field, as in Fig. 3.3(g), which is consistent with the behavior of the topological MZMs. Interestingly, the ABS-induced ZBCP on the left end as in Fig. 3.3(d) is very similar to the MZM-induced ZBCPs in Fig. 3.3(e) though the former one does not possess any topological character.

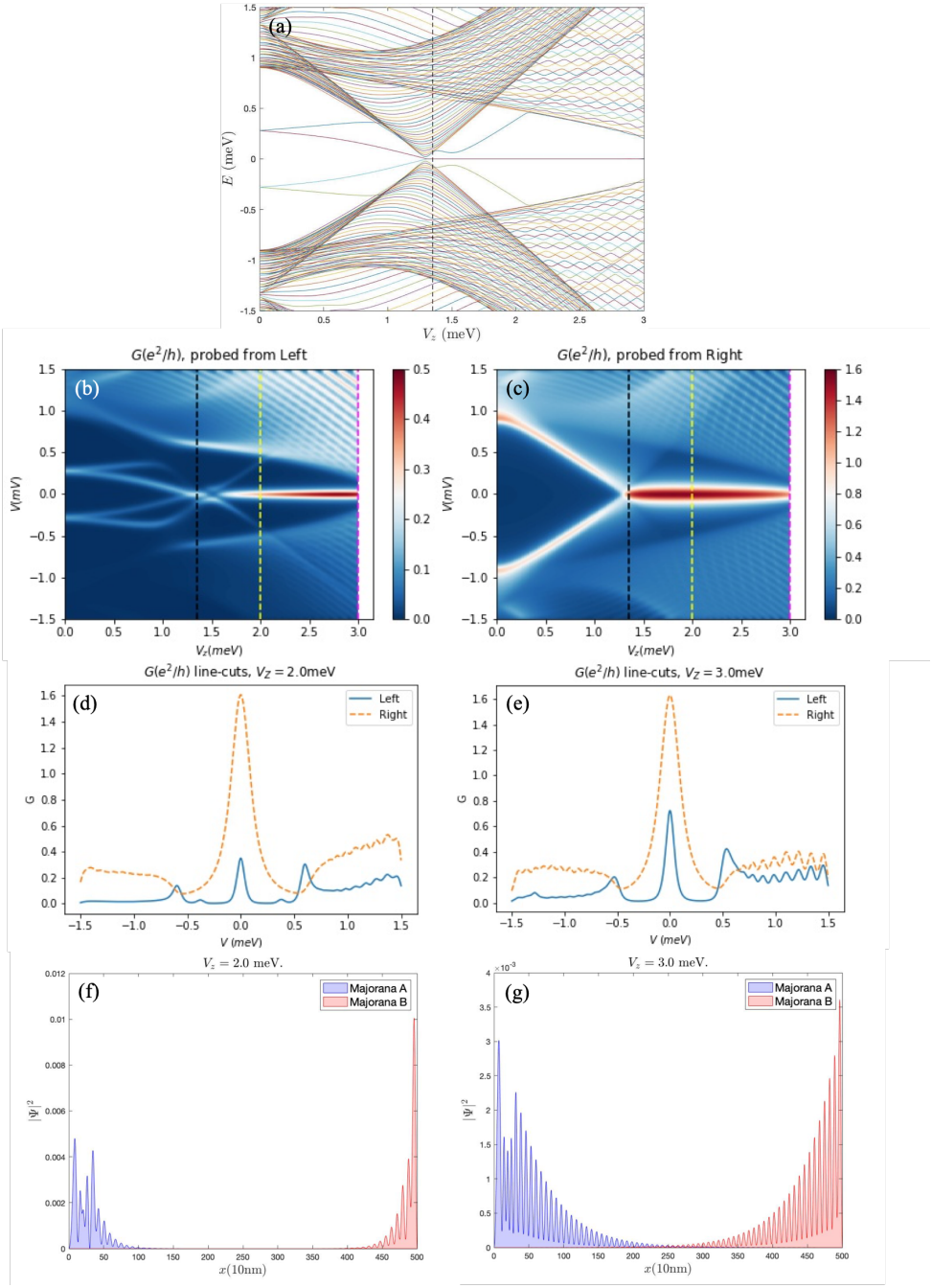

Figure 3.2: Numerical results with chemical potential $\mu = 1.0$ meV. (a) Energy spectrum. (b) Conductance $G(V)$ measured from the left lead. (c) Conductance $G(V)$ measured from the right lead. (d) Conductance linecuts from both leads at $V_z = 2.0$ meV. (e) Conductance linecuts from both leads at $V_z = 3.0$ meV. (f) Majorana components of lowest-lying wave functions in the nanowire at $V_z = 2.0$ meV, above V_{TQPT}. (g) Majorana components of lowest-lying wave functions in the nanowire at $V_z = 3.0$ meV, above V_{TQPT}. The SC collapsing field is at $V_c = 3.2$ meV. The black, yellow and purple vertical dashed lines in the panels (a,b,c) represent the TQPT field $V_{\text{TQPT}} = 1.35$ meV, $V_z = 2.0$ meV and 3.0 meV respectively.

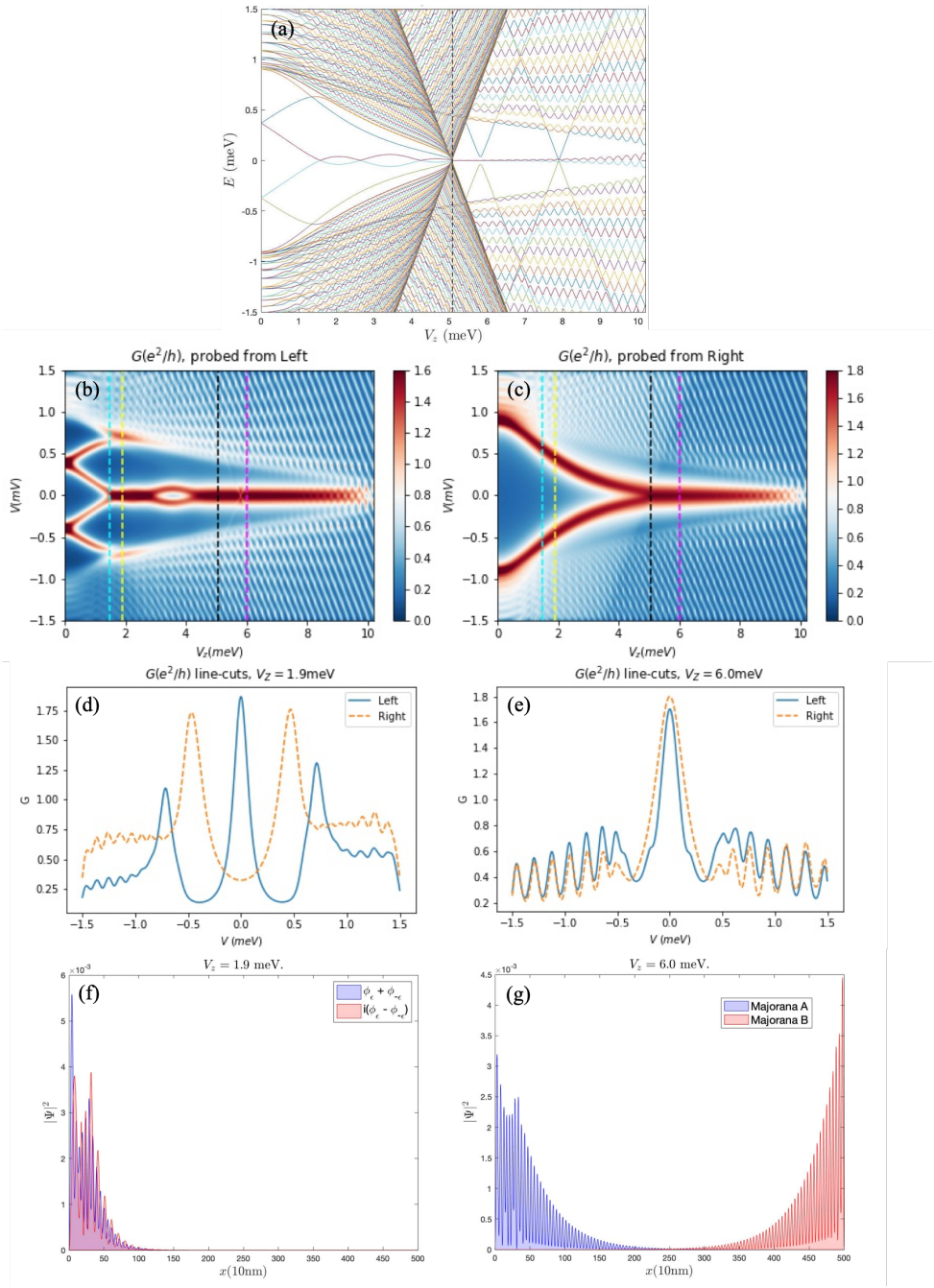

Figure 3.3: Numerical results with chemical potential $\mu = 5.0$ meV. (a) Energy spectrum. (b) Conductance $G(V)$ measured from the left lead. (c) Conductance $G(V)$ measured from the right lead. (d) Conductance linecuts from both leads at $V_z = 1.9$ meV. (e) Conductance linecuts from both leads at $V_z = 6.0$ meV. (f) Majorana components of lowest-lying wave functions in the nanowire at $V_z = 1.9$ meV, below V_{TQPT}. (g) Majorana components of lowest-lying wave functions in the nanowire at $V_z = 6.0$ meV, above V_{TQPT}. The SC collapsing field is at $V_c = 10.4$ meV. The black, yellow and purple vertical dashed lines in the panels (a,b,c) represent the TQPT field $V_{\text{TQPT}} = 5.08$ meV, $V_z = 1.9$ meV and 6.0 meV respectively.

Here we only show results for two chemical potentials as in Fig. 3.2 and Fig. 3.3 to demonstrate the difference of the end-to-end conductance comparisons between MZMs and ABSs, respectively. One can find the extensive results in the appendix of Ref. [83] for many other values of chemical potential and magnetic field to confirm further that the presence (or absence) of end-to-end conductance correlations implies the presence (or absence) of MZMs (or ABSs) in the nanowire. There are several subtleties for our proposed non-local correlation method to work in the experiments.

One subtlety that we would like to address for our method is that all the results we demonstrate in this work satisfy the relation $V_{\text{TQPT}} < V_c$, meaning there is always a topological regime that exists before the SC collapses. If $V_{\text{TQPT}} > V_c$, then there will never be any MZM pair showing up before the SC gap crashes and destroys the TSC nanowire. In this case, all the measured ZBCPs are unfortunately induced from the trivial ABSs and thus manifest no correlations in the tunneling signals from both ends of the wire. Therefore, making sure $V_{\text{TQPT}} < V_c$ is an important ingredient in experiments to realize our proposed non-local correlation method.

Another subtlety we want to emphasize is that the nanowire needs to be long enough (i.e., longer than the SC coherence length) such that the topological physics can manifest itself. If the wire is short, the tail of ABS wave function could extend to the other end, making the ZBCP on the other end also show up. In this case, there will also be end-to-end correlation even for trivial ABSs. The presence of non-local correlation will not be exclusive for the well-separated MZMs at this point. On the other hand, in short wires, it will be easier to discern MZMs by the Majorana splitting oscillations as studied in Ref. [81] already. Our work applies to long wires, where there is a fundamental difference between MZMs and ABSs.

The other false-positive scenario that could accidentally deduce the ABS-induced ZBCPs

to come from MZM pairs is when two different QDs fortuitously locate respectively at each end of the wire. In this case, each QD can exhibit ABS-induced ZBCP on both ends, leading to the presence of non-local correlations in the tunneling measurements from the two ends. This issue is statistically unlike to happen, but cannot be ruled out. Therefore, one should pay more attention to the presence of non-local correlation before jumping to the conclusion about the existence of MZMs. This issue can be taken care better if one can also show the bulk gap closing and reopening near the TQPT using the same setup [Fig. 3.1] as a cross-check, which we will discuss in the next sub-section.

3.3 Numerical Results: Cross Conductance

Other than the conductance correlation between the two ends of the wire, our three-terminal setup as in Fig. 3.1 allows one to measure the cross conductances, $G_{\text{LR}} = dI_L/dV_R$ or $G_{\text{RL}} = dI_R/dV_L$. This non-local conductance is useful because it can distinguish the bulk states from non-topological subgap states induced by potential inhomogeneity [82]. It is important in the sense that bulk states appearing at the gap closure is a hallmark of the TQPT, which should tell us the boundary between the trivial regime and the topological regime. One can find the cross conductance G_{LR} as a function of voltage for a pristine nanowire model showing bulk gap closure [Fig. 3.4(a)], which is a signature of TQPT. Specifically, with the Zeeman field varying, the cross conductance area that is suppressed to zero becomes narrower from $V_z = 2.8$ meV to $V_z = V_{\text{TQPT}} = 3.13$ meV, but then becomes wider again as the Zeeman field is increased to $V_z = 3.3$ meV, which demonstrates bulk gap closing and reopening near the TQPT. On the other hand, in Fig. 3.4(b), we show the cross conductance for the nanowire with an embedded QD on

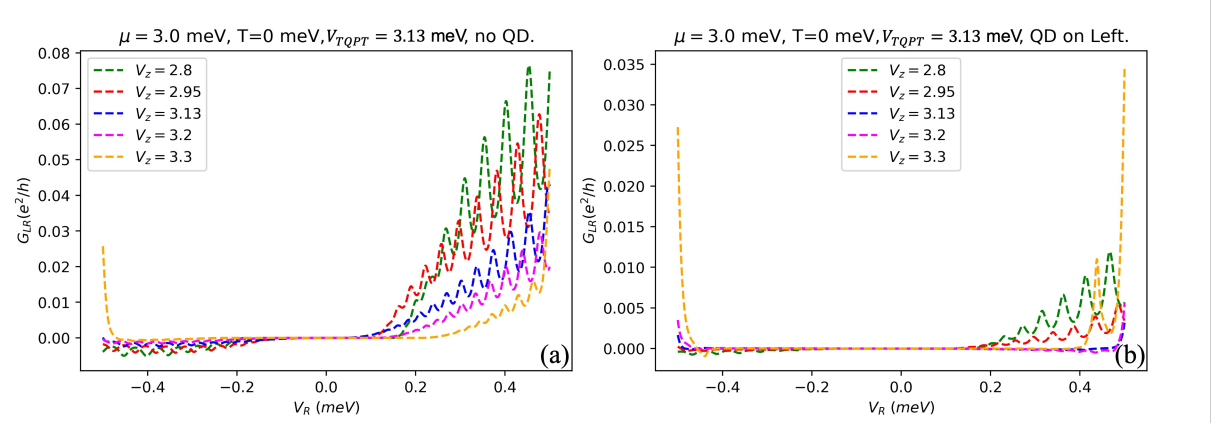

Figure 3.4: Cross conductance G_{LR} as a function of voltage V_R from the right end applied to the nanowire, for different Zeeman fields V_z. Note that the induced tunnel barrier height is $E_{\mathrm{barrier}} = 1.0$ meV. (a) G_{LR} for a pristine Majorana nanowire. The bulk gap appears to close and reopen as V_z crosses the TQPT field V_{TQPT}. (b) G_{LR} for a Majorana nanowire with an embedded QD on the left end. The bulk gap closing and reopening signature is difficult to see in (b).

the left end. In this case, the cross conductance is almost zero in an apparently wide voltage range, and the signature of bulk gap closing and reopening near TQPT is clearly suppressed with this extra QD embedded. One may therefore need to implement extra tuning to compensate this suppressing effect brought by the QD. Nevertheless, the cross conductance one can check upon the same setup can be used as a cross-check method for the existence of MZMs.

3.4 Summary

Through our extensive numerical simulations, the ABS-induced ZBCP can be distinguished from the topological MZM-induced ZBCP by comparing independent tunneling measurements carried out from both ends of the wire at the same time. The basic idea behind our work is simple: Topological MZMs exhibit non-local nature intrisically, whereas the topologically-trivial

ABSs can only exist near one or the other end depending on the extrinsic details. Therefore, a tunneling measurement from a particular end can only detect an ABS-induced ZBCP if the ABS locates at that end, whereas the MZM-induced ZBCPs must be equally accessible from both wire ends. Note that the signature of non-local correlated ZBCPs for MZMs has been well-studied in Ref. [81]; nevertheless, the work presented in this chapter incorporates detailed studied in the scenario of trivial ABSs existing in the wire, which is outside the domain of Ref. [81]. As long as the subtle conditions, including $V_{\mathrm{TQPT}} < V_c$, $L \gg l_c$ (nanowire length is much longer than the SC coherence length), and two unintended QDs do not accidentally locate at both ends of the wire, one should be able to claim that the presence (absence) of correlated ZBCPs from both ends indicate the presence (absence) of the topological MZMs (trivial ABSs) in the nanowire.

For completeness, we also studied the cross conductance that can be measured in the same three-terminal setup as the conductance correlation. We have shown that the bulk gap closing and reopening feature near TQPT can be clearly identified in the pristine nanowire, where only MZMs exist. However, the QD-induced ABSs could obscure this feature, making the TQPT field hard to identify. MZMs can exist in the nanowire even when the cross-conductance fails to demonstrate a TQPT. Therefore, we suggest using a combination of end-to-end conductance correlation together with cross conductance to confirm the existence of MZMs so as to avoid false-positive conclusions.

Chapter 4: **Coulomb-blockade Transport In Realistic Majorana Nanowires**

Motivated by the Coulomb blockade experiments introduced in Chapter 1 (Sub-section 1.5.3), we want to theoretically study the Majorana nanowire in the CB regime with the realistic modeling in this chapter. Particularly, we intend to explain the features, the "bright-dark-bright" pattern, and the decreasing OCPS with the increasing Zeeman field that appear in the experiments. [91, 113, 114]. In addition, we will justify if the experimental results of the length-dependent OCPS [91] are an indication of MZMs.

The relatively short experimental device length for epitaxially grown SC-SM nanowires allows for a measurement of transport in the CB regime [91, 113, 114] simply by lowering the transmission to either end of the wire. The schematic setup for CB transport measurements is shown in Fig. 4.1, which describes a CB SC-SM island between two leads. Transport in the CB regime, while somewhat more complicated to theoretically interpret relative to QPC tunneling, provides information about the states at both ends and possibly also bulk transport [91, 115, 116]. The theoretical complication arises from the fact that one must take into account both MBS and CB physics on an equal and non-perturbative footing while at the same time addressing the non-equilibrium physics of tunneling transport. Direct measurement of tunnel conductance at both ends requires a three-terminal configuration [49], which risks generating additional spurious sub-gap states at the third contact [117]. The CB measurement dispenses with the need for such a

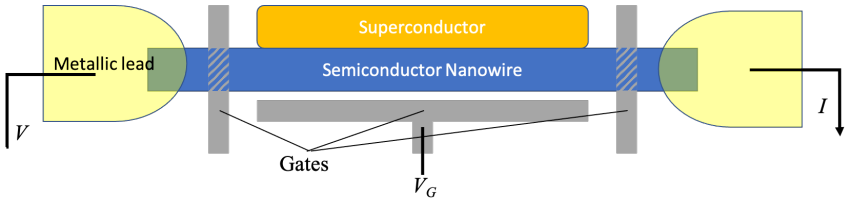

Figure 4.1: Schematic plot of the Coulomb blockaded Majorana nanowire. This semiconducting nanowire (e.g. InAs or InSb) is proximitized by the parent s-wave superconductor (e.g. Al) which only covers part of the nanowire. The gate with voltage V_G controls charge on the nanowire. The Coulomb blockaded transport is measured between the leads shown at the two ends of the Majorana nanowire. The coupling to the leads is pinched off to the required degree by the tunnel gates shown.

third contact, leading to a more straightforward measurement. Additionally, as we will discuss later in this work, the CB conductance is less sensitive to subgap states that are localized only at one end or another, with the exception of MBSs, making it a particularly attractive experimental approach. This possibility of exploring both wire ends and the bulk so that the bulk-boundary topological correspondence could be investigated in a single experiment in a single sample compels us to carry out the extensive theoretical analysis presented in this work.

Despite the advantages of CB measurements, they are more complicated to interpret relative to QPC both because of the involvement of tunneling at both ends and Coulomb interaction. As a result, there is no standard formalism to model such transport analogous to the BTK formalism used to model QPC tunneling [59–69]. In fact, the interplay of Coulomb interactions and low-temperature Fermi-liquid correlations can lead to intricate many-body physics, such as the Kondo effect [118–122], which can further complicate the interpretation of data. Such complications can be avoided for temperatures above the Kondo temperature, where transport can be modeled by perturbation theory in tunneling [115]. However, CB transport through a complex system, such

as an SC-SM nanowire which has many low-energy levels, is challenging to treat numerically and is characterized by an exponential complexity of the perturbative rate equations [116].

In this work, we show that the CB transport can be modeled at the same level of complexity as QPC tunneling, provided we consider the regime where the tunneling rate is below the equilibration rate of the nanowire. This assumption leads us to a generalized Meir-Wingreen formula for tunnel conductance, which we use to study various effects in the nanowire, such as ABSs, self-energy, and soft gap. We anticipate that our theory will provide a route to interpret CB transport in hybrid Majorana systems resulting from these important realistic effects.

4.1 Ideal Simulation Result

One of the main motivations of our work is to provide a qualitative understanding of measured CB transport experiments [91,113,114]. Therefore, before presenting the details of the formalism in Secs. 4.2, 4.3 and 4.4, we present a preliminary description of our main results to motivate our work. In Fig. 4.2(a), we show a representative result that qualitatively resembles some of the recent experimental data [91, 113, 114] for the CB conductance as a function of gate-induced charge number n_g and Zeeman field V_z. As discussed in more detail in Sec. 4.5, Figs. 4.2(b,c,d) allow us to compare the information from Fig. 4.2(a) to other characteristics of the wire, such as end conductance [Fig. 4.2(b)] that is measured more typically (i.e., QPC) [31–35,37,43,123] and the nanowire spectrum [Fig. 4.2(c)], which is the information desired from tunneling transport. The OCPS shown in Fig. 4.2(d) is directly obtained from the peak spacing along n_g in Fig. 4.2(a) and can be compared to parts of the spectrum in Fig. 4.2(c). The model used to obtain the results in Fig. 4.2(a), which most closely resembles experimental data [91,113,114], is a Majorana

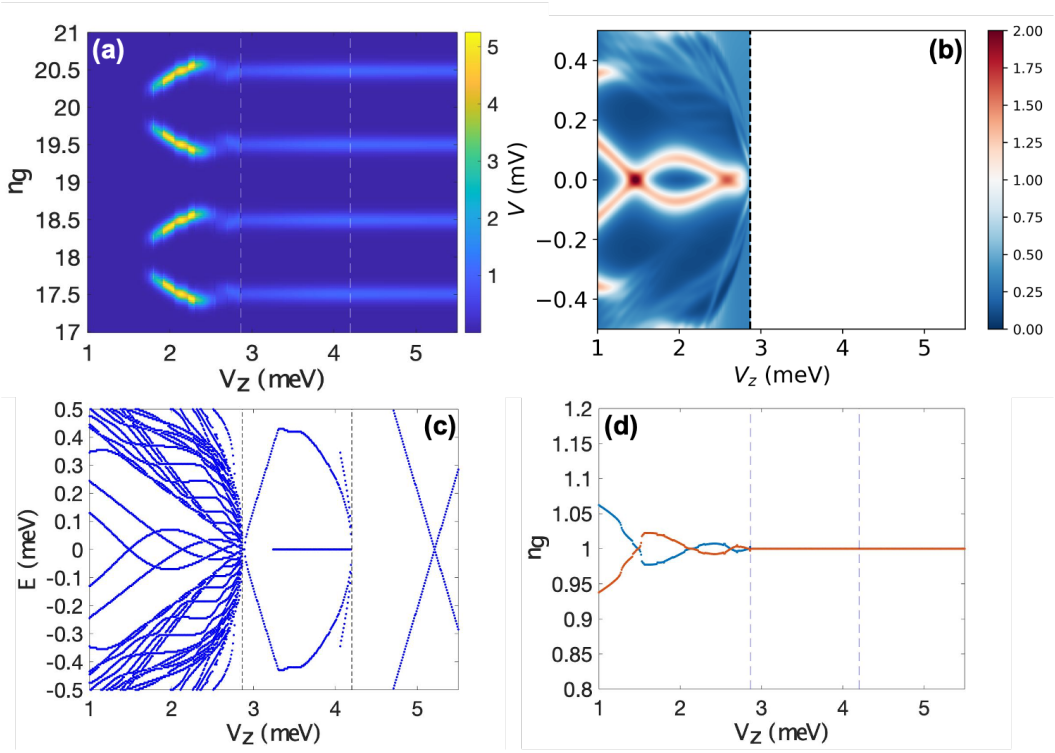

Figure 4.2: The ideal case results, which show the most similar features as experimental data by fine-tuning. The parameters are: the temperature $T = 0.01$ meV, the wire length $L = 1.5$ μm, the SC gap at zero Zeeman field $\Delta_0 = 0.9$ meV, the SC collapsing field $V_c = 4.2$ meV. Other relevant parameters are given in Sec. 4.5. (a) Coulomb-blockade conductance G as a function of the gate-induced charge number n_g and Zeeman field V_z at $E_c = 0.13$ meV. We only show two periods in the range of $n_g \in [17, 21]$. (b) Non-Coulomb-blockade conductance G from the left lead as a function of bias voltage V and Zeeman field V_z. (c) Energy spectrum as a function of Zeeman field V_z. (d) OCPS as a function of Zeeman field V_z that is extracted from the vertical peak spacing in panel (a).

nanowire model that includes quantum dots, self-energy effects, suppression of SC, and soft SC gap, in addition to CB (see Sec. 4.4 for details).

Figure 4.2(a) does not show the $2e$-periodic (in n_g) part of the CB conductance that appears as the brightest features in the experimental data [91, 113, 114] at the lowest part of Zeeman field range. This is because the quasi-particle gap in this range of Zeeman field, which is below that shown in Fig. 4.2(a), is larger than the charging energy E_c, so the transport is dominated by Cooper-pair transport [115]. The charging energy E_c is defined by the electrostatic energy

$$U(N) = E_c(N - n_g)^2, \tag{4.1}$$

where N is the total electron number in the Majorana nanowire. The range of Zeeman energy plotted in Fig. 4.2(a) is where the quasi-particle gap is below E_c, so the conductance is dominated by single-electron transport. As will be discussed in more detail in Sec. 4.2, the calculated conductance G is $2e$-periodic in the gate charge n_g. As a result, the conductance plot shown in Fig. 4.2(a) is representative of the conductance over the entire range of gate charge n_g. Note that the CB conductance [e.g. Fig. 4.2(a)] in this work is shown in units where the normal-state conductance peak (i.e., at high V_z) is equal to one. This is a natural unit to use in CB situations, and further details of this choice are discussed following Eq. (4.36).

The energy spectrum in Fig. 4.2(c) shows (as elaborated in Sec. 4.5) that the oscillations seen in the OCPS in Fig. 4.2(d) arise from ABSs [59, 61–65] (and not MBSs) at the ends of the wire. The dark region of the conductance in Fig. 4.2(a) arises from the part of the ABS where the energy difference between the two ABSs at the two ends exceeds the temperature. The structure of this energy spectrum contains multiple subgap states as in Shen *et al.* [113] As

illustrated in Sec. 4.5, we find such oscillations in OCPS with decreasing amplitude only in the case of QD-generated ABSs before the TQPT shown by the first dashed line in Fig. 4.2(a). One of the puzzling features of the CB conductance data [91, 113, 114] in Majorana nanowires is the intensity of the $2e$-periodic peaks being higher than the $1e$-periodic part, which is the opposite of what the naive expectation is. This occurs despite the $2e$ conductance arising from Cooper-pair transport, which is higher-order in the tunneling, while the $1e$-periodic peaks being from electron transport. As a result, as discussed in Sec. 4.3, the conductance of the $2e$-periodic part is theoretically expected to be smaller [115]. However, our results in Fig. 4.2(a) show a significant suppression of the $1e$-periodic conductance both from the self-energy corrections as well as from the soft-gap, compared with systems where these effects are not included. This suppression can explain the discrepancy between the experiments [91,113,114] and the simple model of Majorana tunneling for $1e$-periodic conductance [115]. A more detailed understanding of the features in Fig. 4.2 as well as the role of the various contributing factors, such as soft-gap, self-energy, and quantum dots, are provided in Sec. 4.5.

4.2 Two-terminal Generalized Meir-Wingreen Formalism

We will start by combining the rate equation formalism with an equilibration assumption to derive a two-terminal generalization of the Meir-Wingreen mesoscopic theoretic formalism for the interacting CB system. We will then apply this formalism to a semi-realistic model for a semiconductor nanowire that has been used to study QPC tunneling [27, 59–69, 83, 104, 110, 124] in Majorana nanowires. We will then study various limits of the model to develop a generic correspondence between features seen in CB transport experiments [91, 113, 114] manifesting

characteristics of the semiconductor wire model such as self-energy, soft gap etc.

4.2.1 Setup

Let us consider transport through a thermalizing dot Q, which has N units of charge on it. Note that this thermalizing dot is our main system, i.e., the nanowire in our case, which has nothing to do with the unintentional quantum dots induced by disorder in our context. It is described by the Hamiltonian

$$H_Q = \sum_j E_j |\psi_j\rangle\langle\psi_j|, \tag{4.2}$$

where $\{E_j\}$ is the set of energies of the system. The dot Q is coupled to two leads L and R, with chemical potential μ_L and μ_R, respectively, through a tunneling Hamiltonian

$$H_t = \sum_{k,\alpha=L,R} t_\alpha \left[a^\dagger_{k\alpha} c_\alpha + \text{H.c.} \right], \tag{4.3}$$

where $c_{\alpha=L,R}$ is an electron annihilation operator on the left and right ends of Q. The operators $a^\dagger_{k,\alpha}$ create electrons in the leads $\alpha = L, R$. t_α is the tunneling matrix element at the α end.

We treat the tunneling to the lead perturbatively as in Ref. [125]. The tunnel coupling is assumed to be weak enough so that the quantum dot Q can reach thermal equilibrium between successive tunneling events that change the conserved change N. The assumption here is that the tunneling is slow compared with the equilibration time, which can always be ensured by tuning the tunnel barrier. Within this framework, the state of dot Q within a specific charge sector N, labeled i, have a conditional probability given by the Boltzmann distribution

$$P_N(E_i) = Z_N^{-1} e^{-\beta E_i}, \tag{4.4}$$

where E_i is the energy of state i, β is the inverse of temperature, and

$$Z_N = \sum_i e^{-\beta E_i} \tag{4.5}$$

is the normalized partition function for each charge N, i.e., state i has N electrons. Note that

$$P_N(E_i) = \frac{P(E_i)}{P_{0,N}}, \tag{4.6}$$

where $P(E_i)$ is the probability of the state i with energy E_i and $P_{0,N}$ is the probability of having N electrons. It is assumed that the state i has N electrons.

The probability distribution $P_{0,N}$ of having N electrons is determined by the balance of two processes where the system Q either gains or loses the electron from the leads via a tunneling process. The tunneling rate of electrons from the leads into Q, which is assumed to be in a charge state N, can be computed using Fermi's golden rule to be

$$\Gamma_N^\alpha = \tau_\alpha \sum_{i,j} P_N(E_i) \int d\epsilon f(\epsilon - \mu_\alpha)\delta(E_j - E_i - \epsilon)|\langle\psi_j|c_\alpha^\dagger|\psi_i\rangle|^2, \tag{4.7}$$

where $f(\epsilon) = (1 + e^{\beta\epsilon})^{-1}$ is the Fermi function, $c_\alpha^\dagger$ is the electron creation operator at the end $\alpha = L, R$ of the system, and $\tau_\alpha = t_\alpha^2 \rho_\alpha$ is the basic tunneling rate into the lead α with ρ_α being the density of states in lead $\alpha = L, R$. Considering the current from tunneling at voltages large compared to the SC gap, the tunneling rate τ_α can be written as $\tau_\alpha = g_\alpha / 2\pi\nu_{1D,\alpha}$ [115], where g_α is the normal-state conductance at the end α and $\nu_{1D,\alpha}$ is the density of states at the end of the Majorana nanowire. Following the derivation in Appendix A.1, one can show that the reverse

tunneling rate of electrons Λ_N^α, i.e., from dot Q into the leads, is related to the rate Γ_N^α as

$$\Lambda_N^\alpha = e^{-\beta\mu_\alpha}\frac{Z_{N-1}}{Z_N}\Gamma_{N-1}^\alpha. \tag{4.8}$$

Such a relation is consistent with the requirement of satisfying the correct number distribution in Q when the system is decoupled from one of the leads.

More generally, let us consider the process of transferring j electrons into the dot as $\Gamma_N^{\alpha,j}$. Equilibrium with the lead α requires the rate of the reverse process to be

$$\Lambda_N^{\alpha,j} = e^{-j\beta\mu_\alpha}\frac{Z_{N-j}}{Z_N}\Gamma_{N-j}^{\alpha,j}. \tag{4.9}$$

4.2.2 Steady-state Rate Equations

The steady-state probability distribution $P_{0,N}$ can be determined from the rates Γ_N^α and Λ_N^α by equating the rate of electrons transitioning from having N electrons to $N \pm 1$ electrons to the rate of electrons making the reverse transition. This equation, following the definitions of the rates Γ_N^α and Λ_N^α, can be written to be:

$$P_{0,N}\sum_{\alpha,j}(\Gamma_N^{\alpha,j} + \Lambda_N^{\alpha,j}) = \sum_{\alpha,j}\left[P_{0,N-j}\Gamma_{N-j}^{\alpha,j} + P_{0,N+j}\Lambda_{N+j}^{\alpha,j}\right] \tag{4.10}$$

Substituting $\Lambda_N^{\alpha,j}$ from Eq. (4.9) and rearranging the terms, the above condition is given by

$$\sum_{\alpha,j}\tilde{\Gamma}_N^{\alpha,j}\{\tilde{P}_{0,N} - \tilde{P}_{0,N+j}e^{-j\beta\mu_\alpha}\} = \sum_{\alpha,j}\tilde{\Gamma}_{N-j}^{\alpha,j}\{\tilde{P}_{0,N-j} - \tilde{P}_{0,N}e^{-j\beta\mu_\alpha}\} \tag{4.11}$$

where $\tilde{\Gamma}_N^{\alpha,j} = \Gamma_N^{\alpha,j} Z_N$ and $\tilde{P}_{0,N} = P_{0,N}/Z_N$. The above equation is solved by the detailed balance condition, where both sides of the above equation vanish such that

$$\tilde{P}_{0,N} = \left(\frac{\sum_{\alpha,j} \tilde{P}_{0,N+j} \tilde{\Gamma}_N^{\alpha,j} e^{-j\beta\mu_\alpha}}{\sum_{\alpha,j} \tilde{\Gamma}_N^{\alpha,j}} \right). \tag{4.12}$$

Redefining $P'_{0,N} = \tilde{P}_{0,N} e^{-N\beta\mu_L}$ to simplify the equilibrium solution and defining $\mu_\alpha = V_\alpha + \mu_L$ as the voltages for linear response, the above equation becomes

$$P'_{0,N} = \left(\frac{\sum_{\alpha,j} P'_{0,N+j} \tilde{\Gamma}_N^{\alpha,j} e^{-j\beta V_\alpha}}{\sum_{\alpha,j} \tilde{\Gamma}_N^{\alpha,j}} \right) \tag{4.13}$$

$$\approx \left(\frac{\sum_{\alpha,j} P'_{0,N+j} \tilde{\Gamma}_N^{\alpha,j}}{\sum_{\alpha,j} \tilde{\Gamma}_N^{\alpha,j}} \right) - \beta \left(\frac{\sum_{\alpha,j} j P'_{0,N+j} \tilde{\Gamma}_N^{\alpha,j} V_\alpha}{\sum_{\alpha,j} \tilde{\Gamma}_N^{\alpha,j}} \right) \tag{4.14}$$

There is a trivial solution for equilibrium with $V_\alpha = 0$, which is constant with $P'_{0,N} = P_{0,eq} + v_N$, so

$$v_N \approx \left(\frac{\sum_{\alpha,j} v_{N+j} \tilde{\Gamma}_N^{\alpha,j}}{\sum_{\alpha,j} \tilde{\Gamma}_N^{\alpha,j}} \right) - \beta P_{0,eq} \zeta_N \tag{4.15}$$

$$\zeta_N = \left(\frac{\sum_{\alpha,j} j \tilde{\Gamma}_N^{\alpha,j} V_\alpha}{\sum_{\alpha,j} \tilde{\Gamma}_N^{\alpha,j}} \right). \tag{4.16}$$

This solution is invariant under a constant shift, which in principle is fixed by normalization. In the case of a two-terminal case, only $V_R = V$ is non-zero, so we can expand $\zeta_N = \rho_N V$, where

$$\rho_N = \left(\frac{\sum_j j \tilde{\Gamma}_N^{R,j}}{\sum_{\alpha,j} \tilde{\Gamma}_N^{\alpha,j}} \right). \tag{4.17}$$

The fluctuations v_N can now be expanded $v_N = \beta P_{0,eq} V \nu_N$, which satisfies

$$\nu_N \approx \left(\frac{\sum_{\alpha,j} \nu_{N+j} \tilde{\Gamma}_N^{\alpha,j}}{\sum_{\alpha,j} \tilde{\Gamma}_N^{\alpha,j}} \right) - \rho_N. \tag{4.18}$$

4.2.3 Linear-Response Conductance

The current at the left lead L is determined by the balance of electrons tunneling in and out of L. Using the definitions of the tunneling rate $\Gamma_N^{\alpha,j}$ and $\Lambda_N^{\alpha,j}$, this current can be written as

$$I = \sum_{N,j} j P_{0,N} \left(\Gamma_N^{L,j} - \Lambda_N^{L,j} \right). \tag{4.19}$$

Using the rescaled variables in Eq. (4.11), the current is re-written as

$$I = \sum_{N,j} j \tilde{\Gamma}_N^{L,j} e^{\beta N \mu_L} \{ P'_{0,N} - P'_{0,N+j} \}. \tag{4.20}$$

Substituting the current to linear order is

$$I \approx \sum_{N,j} j \tilde{\Gamma}_N^{L,j} e^{\beta N \mu_L} \{ v_N - v_{N+j} \}. \tag{4.21}$$

Fortunately, the current is not affected by the constant shift ambiguity.

Divided by V, the conductance is found to be

$$G = \sum_{N,j} j \beta P_{0,eq} \tilde{\Gamma}_N^{L,j} e^{\beta N \mu_L} \{ \nu_N - \nu_{N+j} \} \tag{4.22}$$

$$= \sum_{N,j} j \gamma_N^{L,j} \{ \nu_N - \nu_{N+j} \}, \tag{4.23}$$

where $\gamma_N^{\alpha,j} = -\beta P_{0,N}\Gamma_N^{\alpha,j}$. Since the redefinition is a scaling that depends only on N and the equation for ν_N only involves ratios of $\tilde{\Gamma}$, the equation for ν can be re-written in terms of $\gamma_N^{\alpha,j}$ as

$$\rho_N = \left(\frac{\sum_j j\gamma_N^{R,j}}{\sum_{\alpha,j} \gamma_N^{\alpha,j}} \right). \tag{4.24}$$

The fluctuations v_N can now be expanded as $v_N = \beta P_{0,eq} V \nu_N$, which satisfies

$$\nu_N \approx \left(\frac{\sum_{\alpha,j} \nu_{N+j}\gamma_N^{\alpha,j}}{\sum_{\alpha,j} \gamma_N^{\alpha,j}} \right) - \rho_N. \tag{4.25}$$

4.2.4 Generalized Meir-Wingreen Formula

In this case, we limit to one-electron processes that should dominate in the strict tunneling limit. If necessary, the generalization to multi-electron processes is straightforward, albeit quite cumbersome, but multi-electron transport should be negligible in the tunneling limit of interest here.

The zero-bias conductance G can be calculated by expanding the current I to the lowest order in the bias voltage $\mu_R - \mu_L = V$. Refer to the Appendix A.3,

$$G = \frac{dI}{dV}|_{V=0} = -\beta \sum_N \tilde{P}_{0,N} \frac{\tilde{\Gamma}_N^R \tilde{\Gamma}_N^L}{\tilde{\Gamma}_N^R + \tilde{\Gamma}_N^L}. \tag{4.26}$$

Restoring the variable change from Eq. (4.11), the conductance can be re-written in terms of a re-scaled lead conductance $\gamma_N^\alpha = -\beta P_{0,N}\Gamma_N^\alpha$ as

$$G = \sum_N \frac{\gamma_N^R \gamma_N^L}{\gamma_N^R + \gamma_N^L}. \tag{4.27}$$

Incidentally (as detailed in the Appendix A.4), applying all the variable transformation to Eq. (4.7), the rescaled transition rate γ_N^α is given by

$$\gamma_N^\alpha = \tau_\alpha \sum_{i,j} \{P(E_i) + P(E_j)\} f'(E_j - E_i - \mu) \left|\langle \psi_j | c_\alpha^\dagger | \psi_i \rangle\right|^2, \tag{4.28}$$

which is very similar to the effective one-terminal conductance in the Meir-Wingreen's paper [126].

In the strong CB limit, where only two charge states N and $N-1$ participate in transport, γ_N can be assumed to vanish except for one value of N, so

$$G = \frac{\gamma_N^R \gamma_N^L}{\gamma_N^R + \gamma_N^L}, \tag{4.29}$$

which is physically the series formula for the conductance at each end. This equation is the same as Eq.(176) of the Aleiner *et al.* review [127], except that the matrix elements of Eq.(130) are replaced by the Meir-Wingreen formula.

To proceed further, we assume the system Hamiltonian [i.e., Eq. (4.2)] to be of the form

$$H_Q = \sum_p \epsilon_p d_p^\dagger d_p + U(N), \tag{4.30}$$

where ϵ_p is the eigen-energy of the quasi-state p. The electron number variable N is in general different from the total occupation of Bogoliubov quasi-particles $d_p^\dagger$ and instead is equivalent to the parity of the number of quasi-particles in this case. Specifically, in the limit of strong Coulomb blockade where only two consecutive values of electron number N_0, $N_0 - 1$ are allowed, the electron number $N \in \{N_0, N_0 - 1\}$ can be uniquely fixed by the relation $(-1)^N = Q_0 \cdot (-1)^{\sum_p d_p^\dagger d_p}$,

where Q_0 is the ground-state fermion parity of the first part (i.e., BdG) of the Hamiltonian H_Q, written as

$$Q_0 = \mathrm{Pf}\{H_{Q,\mathrm{BdG}}(E=0)\}, \tag{4.31}$$

where $H_{Q,\mathrm{BdG}}$ is the first part of H_Q written in a Majorana basis. Applying this relation to Eq. (4.1), we can show that $U(N) = (\Delta U/2) \cdot Q_0 \cdot (-1)^{\sum_p d_p^\dagger d_p}$, where $\Delta U = (-1)^{N_0}[U(N_0) - U(N_0-1)]$ is the electrostatic energy difference between the two transition-allowed charge states $N_0, N_0 - 1$. Substituting the energy eigenvalues E_i and wave-functions $|\psi_i\rangle$ for H_Q, the coefficients γ_N^α in Eq. (4.28) can be written in a more explicit form (details are in Appendix A.4):

$$\gamma_N^\alpha = \beta \frac{e^2}{\hbar} \sum_p \sum_{n=0,1} \sum_{Q=\pm 1} \tilde{F}_p(n,Q) \left[(1-n)A_p^\alpha + nB_p^\alpha\right], \tag{4.32}$$

where

$$\tilde{F}_p(n,Q) = f_{eq}\left[(1-2n)\epsilon_p - Q\Delta U\right] \cdot F_p(n,Q) \tag{4.33}$$

with

$$F_p(n,Q) = \frac{e^{-\beta\left(\frac{Q\Delta U}{2} + n\epsilon_p\right)}\left[1 + QQ_0(-1)^n \prod_{s\neq p} \tanh\left(\frac{\beta\epsilon_s}{2}\right)\right]}{\sum_{Q=\pm 1}\sum_{n=0,1} e^{-\beta\left(\frac{Q\Delta U}{2} + n\epsilon_p\right)}\left[1 + QQ_0 \prod_s \tanh\left(\frac{\beta\epsilon_s}{2}\right)\right]}. \tag{4.34}$$

Note that $f_{eq}(\epsilon) = (1 + e^{\beta\epsilon})^{-1}$ is the Fermi distribution at equilibrium and, following Eqs. (4.56) and (4.57),

$$A_p^\alpha = \sum_{\sigma=\uparrow,\downarrow} |u_{p,\alpha\sigma}|^2 \tag{4.35}$$

is the tunneling rate for the electron from the lead at α end to the nanowire (same for the opposite direction), and

$$B_p^\alpha = \sum_{\sigma=\uparrow,\downarrow} |v_{p,\alpha\sigma}|^2 \tag{4.36}$$

is the tunneling rate for the hole from the lead at α end to the nanowire (same for the opposite direction), where τ_α are assumed to be the same at both ends α. Within the tunneling limit considered here, the value of the tunneling amplitudes τ_α determines the overall scale of the conductance G. In our calculation, the value of τ_α has been chosen such that the peak height in the normal metal (i.e., large V_z) regime is equal to 1. This should be considered a choice of units for our calculation. Comparison to experimental data can be made by scaling the experimental data in a similar way by the normal state conductance. We note that this choice of unit is the natural one in the tunneling limit under consideration here. Note that $u_{p,\alpha\sigma}$ and $v_{p,\alpha\sigma}$ are coefficients of electron and hole relation with quasi-particle and quasi-hole that are discussed in more detail in Sec. 4.4.1.

The equation for G in Eq. (4.27), together with the definitions (4.31)-(4.36), is the central formalism used in this work to compute the conductance of a system Q coupled to separate leads L and R. Since the only constraint in equations for the conductance [Eqs. (4.31)-(4.36)] connecting the number of electrons N to the quasi-particle degrees of freedom is through the parity, the results are invariant as long as N changes by 2. Using Eq. (4.1), this also implies that the conductance G is periodic in n_g with period 2. Because of this, in this paper, we will only plot the gate charge n_g over two periods i.e., a range of length 4. This formalism reduces, in the case where leads L and R coincide in space, to the well-known conductance derived by Meir and Wingreen [126] for interacting systems. Our work generalizes the formalism to the situation with arbitrarily spatially separated L and R leads as appropriate for Majorana nanowire experiments.

4.3 Conductance for Few-level Systems

The evaluation of the conductance G using Eq. (4.27) for a realistic Majorana system, which has a complicated spectrum, requires a rigorous numerical treatment. In this section, we analytically evaluate Eq. (4.27) in cases where the system Q has one or two levels in the low-energy spectrum. We will find that the conductance G can be written analytically in these cases. The results in these cases will help understand the numerical results for the more complex Majorana wire system, which in certain parameter regimes contains only a few low-energy levels relevant for these analytical results.

4.3.1 Rates for Few-electron Process

In addition to electron tunneling processes, transport through the system Q also occurs through Cooper-pair tunneling because of the proximity-induced superconductivity. In order to place these two processes on a comparable footing, we rewrite the equation of the scaled transition rate for tunneling of electrons [Eq. (4.28)] as

$$\gamma_N^{\alpha,1} = \beta\tau_\alpha^{(1)} \sum_{i,j} P(E_i) \int d\epsilon f(\epsilon-\mu)\delta(E_j-E_i-\epsilon)M_{ij}^{(1)} \tag{4.37}$$

$$= \beta\tau_\alpha^{(1)} Z_{\text{tot}}^{-1} \sum_{i,j} e^{-\beta(E_i-N\mu)} f(E_j-E_i-\mu)M_{ij}^{(1)}, \tag{4.38}$$

where $M_{ij}^{(1)} = \left|\langle|c_\alpha^\dagger|\rangle\right|^2$ is the transition matrix element for transferring one electron from the leads to the dot, and $\tau_\alpha^{(1)}$ is the one-electron tunneling rate, which was referred to as τ_α in

Eq. (4.7). Similarly, we can write the rate for two-electron (or Cooper-pair) transfer

$$\gamma_N^{\alpha,2} = \beta\tau_\alpha^{(2)} Z_{\text{tot}}^{-1} \sum_{i,j} e^{-\beta(E_i - N\mu)} \int d\epsilon f(\epsilon - \mu) f(E_j - E_i - \epsilon - \mu) M_{ij}^{(2)} \tag{4.39}$$

$$= \tau_\alpha^{(2)} Z_{\text{tot}}^{-1} \sum_{i,j} e^{-\beta(E_i - N\mu)} f^{(2)}(E_j - E_i - 2\mu) M_{ij}^{(2)}, \tag{4.40}$$

where $f^{(2)}(\epsilon) = (\beta\epsilon)/(e^{\beta\epsilon} - 1)$ and $\sqrt{M_{ij}^{(2)}}$ is the matrix element of transferring a Cooper pair into Q. The charge of the system changes by 2, preserving parity under this tunneling process. The parameter $\tau_\alpha^{(2)}$ sets the scale of the Cooper-pair tunneling rate analogous to the one-electron tunneling rate $\tau_\alpha^{(1)}$.

Using the fact that μ and the gate voltage entering E_j play equivalent roles, we can set μ to zero. In that case, we can write the rates in a more symmetric form

$$\gamma_N^{\alpha,1} = \beta\tau_\alpha^{(1)} Z_{\text{tot}}^{-1} \sum_{i,j} \frac{1}{e^{\beta E_i} + e^{\beta E_j}} M_{ij}^{(1)}, \tag{4.41}$$

$$\gamma_N^{\alpha,2} = \beta\tau_\alpha^{(2)} Z_{\text{tot}}^{-1} \sum_{i,j} \frac{E_j - E_i}{e^{\beta E_j} - e^{\beta E_i}} M_{ij}^{(2)}, \tag{4.42}$$

where E_i is understood to be replaced by $E_i \to E_i - \min_i E_i$. The latter can be done since only ratios of E_i enter the formula. In this form, it is clear that any γ_N rate is significant if both energies are less than β^{-1}.

The tunneling matrix elements $\tau_\alpha^{(i=1,2)}$ can be estimated by considering the limits of transport without a SC gap and without sub-gap states respectively. In the case without SC, we can rewrite Eq. (4.41) as $\gamma^1 \approx \beta\tau^{(1)}\nu_Q \int_{\omega>0} d\omega \langle M^{(1)}(\omega)(1 + e^{\beta\omega})\rangle$, where ν_Q is the normal-state density of states (DOS) in the system Q. Ignoring the frequency dependence of $M^{(1)}(\omega)$ on

the scale of the temperature T so that $\nu_Q M^{(1)}(\omega) \approx \nu_{1D,\alpha}$, we can write the end conductance $\gamma^{(1)} \equiv P_{0,N} g_\alpha \sim P_{0,N} \tau_\alpha^{(1)} \nu_{1D,\alpha}$ so that $g_\alpha \sim \tau_\alpha^{(1)} \nu_{1D,\alpha}$, which is similar to the normal-state conductance discussed below Eq. (4.7). In the limit of large conductance at the opposite end, which maintains the equilibrium distribution for the number N, the normal-state conductance is $G \sim g_\alpha$. In the case of Cooper-pair transport with no subgap quasi-particle state and negligible charging energy, we can assume $E_j \sim E_i$ so that $\gamma^{(2)} \sim \tau_\alpha^{(2)} M^{(2)}$. The parameter in this approximation is the single-end NS conductance $g^{(SC)}$ calculated from the BTK formalism [88] so that $\tau^{(2)} M^{(2)} \sim g^{(SC)}$. The Beenakker formula [128] suggests that the gapped SC conductance $g^{(SC)} \sim g_\alpha^2$ in the limit where g_α is the conductance in units of the quantum of conductance and is assumed to be much smaller than unity. Therefore, in the tunneling limit $\gamma^{(2)} \ll \gamma^{(1)}$, leading to the expectation that the conductance from Cooper-pair transport processes should be much smaller than arising from electron transport [129].

The constraint $\gamma_\alpha^{(2)} \ll \gamma_\alpha^{(1)}$ may be alleviated by enhancement of Cooper-pair transport in the presence of ABSs. To understand this, we note that the Cooper-pair tunneling amplitude $\tau_\alpha^{(2)}$ is generated by elastic co-tunneling of two electrons into the SC through virtual states

$$\tau_\alpha^{(2)} = t^2 \sum_n \frac{u_n v_n^*}{E_n - \delta} \tag{4.43}$$

$$= t^2 \int_{\omega > \Delta U} d\omega \mathrm{Tr}[\rho(\omega)\tau_+](\omega - \Delta U)^{-1}, \tag{4.44}$$

where u_n, v_n and E_n are the particle and hole components of the wave functions of states with Bogoliubov-de Gennes (BdG) eigenvalue $E_n > 0$. Here $\rho(\omega)$ is the local density of the SC wire in Nambu space with a particle-hole matrix $\tau_+ = \tau_x + i\tau_y$. Considering a simplified SC model where we apply a uniform pair potential to the states of a normal metal such that the

SC density matrix is given by $\mathrm{Tr}[\rho(\sqrt{\omega^2+\Delta^2})\tau_+] = \rho_0(\omega)\frac{\Delta}{\sqrt{\Delta^2+\omega^2}}$. Within this approxmation, $\tau_\alpha^{(2)} = t^2\int_{\omega>\Delta U} d\omega\rho_0(\omega)\frac{\Delta}{\sqrt{\omega^2+\Delta^2}(\sqrt{\omega^2+\Delta^2}-\Delta U)}$. In the limit of a uniform density of states, we can scale the integration variable $\omega \to \omega\Delta$ so that $\tau_\alpha^{(2)} \approx t^2\rho_0$. The conductance $\gamma_2 \sim \tau_\alpha^{(2)2} \sim t^4\rho_0^2 \sim \gamma_1^2 \ll \gamma_\alpha^{(1)}$. Alternatively, if we consider a scenario that may be realistic for a SM/SC structure where the local density of states in the SM is suppressed near the Fermi level but enhanced above energy $\omega \geq \Delta$, $\tau_\alpha^{(1)} \sim \rho_0(\omega \sim 0)$ may be suppressed without changing $\tau_\alpha^{(2)}$. This allows a situation where the 2e conductance peaks with height γ_2 may exceed the normal CB conductance peaks at high magnetic fields.

4.3.2 Single-bound-state Induced Electron Transport

In the case of one "active" level, i.e., within the range of thermal activation, there are only two states: one with electron number N and another with $N+1$, where the quasi-particle energy $\epsilon = E_{N+1} - E_N$ is the energy difference between the two states. Substituting the quasi-particle energy into Eq. (4.41) leads to

$$\gamma_N^{\alpha,1} = \frac{\beta\tilde{\tau}_\alpha^{(1)}}{4}\mathrm{sech}^2\left(\frac{\beta\epsilon}{2}\right), \tag{4.45}$$

where $\tilde{\tau}_\alpha^{(1)} = \tau_\alpha^{(1)}M_{ij}^{\alpha,(1)}$. In this case, the conductance becomes

$$G = \frac{\beta}{4}\frac{\tilde{\tau}_R^{(1)}\tilde{\tau}_L^{(1)}}{\tilde{\tau}_R^{(1)}+\tilde{\tau}_L^{(1)}}\mathrm{sech}^2\left(\frac{\beta\epsilon}{2}\right), \tag{4.46}$$

which is consistent with Chiu *et al.* [116]. The single-level case is also consistent with Meir-Wingreen's original formula [126]. Note here that the conductance of a state that is localized at

one of the ends of the system is substantially suppressed since one of $\tau_{R,L}^{(1)}$ is small. From the last paragraph, $\tilde{\tau}_\alpha \sim g_\alpha \nu_{1D}$ so that $G \sim \beta\nu_{1D}\frac{g_R g_L}{g_R+g_L}\text{sech}^2(\beta\epsilon/2)$. This conductance is enhanced compared to the non-Coulomb blockaded conductance.

One can use Eq. (4.46) to estimate the conductance in the case of a large number of levels with similar transmissions $\tilde{\tau}$. Assuming that the conductance is split among N levels with conductance $\tilde{\tau}/N$ spread out over a range Δ, the resulting conductance can be approximated by

$$G \simeq \frac{\beta}{4}\frac{\tilde{\tau}_R^{(1)}\tilde{\tau}_L^{(1)}}{\tilde{\tau}_R^{(1)}+\tilde{\tau}_L^{(1)}}\Delta^{-1}\int \text{sech}^2\left(\frac{\beta\epsilon}{2}\right)d\epsilon \tag{4.47}$$

$$\approx \frac{\beta}{4}\frac{\tilde{\tau}_R^{(1)}\tilde{\tau}_L^{(1)}}{\tilde{\tau}_R^{(1)}+\tilde{\tau}_L^{(1)}}\frac{2T}{\Delta}. \tag{4.48}$$

We note that the conductance G in this case is suppressed relative to Eq. (4.46) by a temperature-dependent factor of (T/Δ). This factor cancels the factor $\beta\nu_{1D}$ so that the conductance is now temperature independent and comparable with the conductance of the non-Coulomb blockaded case [127, 130].

4.3.3 One Subgap State At Each End

Let us consider the case of a long wire with a pair of levels, one at each of the left and right ends:

$$\gamma_N^{\alpha,1} = \beta\tau_\alpha^{(1)} Z_{\text{tot}}^{-1}\sum_{i,j}\frac{1}{e^{\beta E_i}+e^{\beta E_j}}M_{ij}^{(1)} \tag{4.49}$$

We assume that there are levels at the two ends of a wire with energy ϵ_α. Generalizing Eq. (4.45) to this case, the left and right conductances would be given by

$$\gamma_N^{\alpha,1} = (2Z_{\text{tot}})^{-1}\, \beta\tilde{\tau}_\alpha^{(1)} e^{-\beta\epsilon_\alpha/2} \text{sech}\left(\frac{\beta\epsilon_\alpha}{2}\right). \tag{4.50}$$

Using Eq. (4.29), the conductance can be written as

$$G = \frac{\beta}{4} \frac{\tilde{\tau}_R^{(1)}\tilde{\tau}_L^{(1)}}{\tilde{\tau}_0^{(1)} \cosh^2\left(\frac{\beta\epsilon_1}{2}\right) + \tilde{\tau}_1^{(1)} \cosh^2\left(\frac{\beta\epsilon_0}{2}\right)}, \tag{4.51}$$

where $\epsilon_0 = \min_\alpha(\epsilon_\alpha)$ and $\epsilon_1 = \max_\alpha(\epsilon_\alpha)$. Note that at the CB resonance, $\epsilon_0 \to 0$ while ϵ_1 stays positive. This means that the conductance G is exponentially suppressed if a pair of levels near the left end and right end have different energies.

If the energy levels of the ABSs on the left and the right are nearly degenerate, i.e., $\epsilon_L \approx \epsilon_R = \epsilon$, the above equation reduces to the result for a single level, i.e., Eq. (4.46) and the conductance suppression is eliminated. This can be seen in the short nanowire case, considering that the ABSs on both ends are delocalized such that one bound state occupies both ends. This also means the exponential suppression in Eq. (4.51) only applies to the long nanowire, where the bound states are localized enough. The conductance for the two-state system in Eq. (4.51) can also be suppressed even in the case of nearly degenerate level $\epsilon_\alpha = \epsilon$ in the presence of gapless states in the bulk of the superconductor that are generated by a magnetic field, as is assumed for the results in Fig. 4.2. This suppression can be understood as a suppression of the tunneling matrix elements τ_α resulting from hybridization between the bound states and the bulk states. As will be elaborated in the discussion, this suppression will play a role in understanding the

suppression of conductance relative to that from the $2e$ periodic Cooper-pair transport.

4.3.4 Conductance Near N and $(N+2)$ Degeneracy

In this case, transport is dominated by Cooper-pair transfer processes and Eq. (4.29) can be generalized to

$$G = \frac{\gamma^{L,2}\gamma^{R,2}}{\gamma^{L,2}+\gamma^{R,2}} \tag{4.52}$$

Using Eq. (4.42), so that $\gamma^{\alpha,2} = \beta\tau^{\alpha,2}\frac{\epsilon}{\sinh(\beta\epsilon)}$, where $\epsilon = E_{N+2} - E_N$, the Cooper-pair conductance is written as

$$G = \frac{\tau^{L,2}\tau^{R,2}}{\tau^{L,2}+\tau^{R,2}}\frac{\beta\epsilon}{\sinh(\beta\epsilon)}. \tag{4.53}$$

We notice that this reaches a maximum value comparable to g_{SC} that is independent of temperature as ϵ approaches 0. This is different from the suppression factor for the single-level case in Sec. 4.3.3 and the maximum value in this case is simply the non-CB conductance g_{SC}.

For an ideal superconductor, the number of electrons in the system N is even. However, sub-gap bound states that are not directly coupled to the leads can play an important role in the CB transport. For example, applied Zeeman fields can drive a state to cross zero energy changing the ground-state parity of N. This leads to a shift in the periodicity of the CB conductance of the system [113]. Another possibility is where the system has states on the order of or lower than the temperature of the system. In this case, the N and $N+2$ degeneracy cannot be reached, because this gate voltage would correspond to a ground state of $N+1$, which has no degeneracy.

4.4 Model

4.4.1 Hamiltonian

The 1D superconductor-proximitized semiconductor nanowire with spin-orbit coupling in the presence of a field-induced Zeeman spin splitting can be described in the following discretized form

$$\hat{H}_{\text{BdG}}(\epsilon) = \sum_x \left\{ C_x^\dagger \left[(2t-\mu)\tau_z\sigma_0 + V_z\tau_0\sigma_x + \Sigma(\epsilon) \right] C_x + \left[C_{x+a}^\dagger(-t\tau_z\sigma_0 + i\alpha\tau_z\sigma_y)C_x + \text{H.c.} \right] \right\}, \tag{4.54}$$

where $C_x = (c_{x\uparrow}, c_{x\downarrow}, c_{x\downarrow}^\dagger, -c_{x\uparrow}^\dagger)$ is the electron operator at position x, and $\Sigma(\epsilon)$ is the self-energy [99] following Eq. (2.3) (replacing ω by ϵ), with the Zeeman-field-varying SC gap following Eq. (2.4). We can also add the quantum dot (QD) into the nanowire. As an example, the potential confining quantum dots for our numerical results follows the form of Eq. (3.1) at the left and right ends of the nanowire, but the potential depth V_D value is different on both sides. l_D is the QD length. The whole Hamiltonian with the QD is

$$\hat{H}_{\text{QD}}(\epsilon) = \sum_x \left\{ C_x^\dagger \left[(2t-\mu+V_{\text{dot}}(x))\tau_z\sigma_0 + V_z\tau_0\sigma_x \right] C_x + \left[C_{x+a}^\dagger(-t\tau_z\sigma_0 + i\alpha\tau_z\sigma_y)C_x + \text{H.c.} \right] \right\}. \tag{4.55}$$

The Hamiltonian of the leads can be described by Eq. (4.55) but replacing $V_{\text{dot}}(x)$ by a constant E_{lead}, which represents the gate voltage applied on the lead. There is also a NS tunnel barrier at the junction between the leads and the nanowire. The Hamiltonian in the area with the tunnel barrier is described by Eq. (4.55) but replacing $V_{\text{dot}}(x)$ by $V_{\text{barrier}}(x) = E_{\text{barrier}}\Pi_{l_{\text{barrier}}}(x)$, a

square potential with potential strength E_{barrier} and width l_{barrier}.

The electron creation and annihilation operators are written in terms of quasi-particles and quasi-holes

$$c^{\dagger}_{x\sigma} = \sum_{p} \left(u^{*}_{p,x\sigma} d^{\dagger}_{p} + v_{p,x\sigma} d_{p} \right), \tag{4.56}$$

$$c_{x\sigma} = \sum_{p} \left(v^{*}_{p,x\sigma} d^{\dagger}_{p} + u_{p,x\sigma} d_{p} \right). \tag{4.57}$$

The normalization leads to $\sum_{x,\sigma} \left(|u_{p,x\sigma}|^2 + |v_{p,x\sigma}|^2 \right) = 1$. The quasi-particle and quasi-hole for the energy level p are given by

$$d^{\dagger}_{p} = \sum_{x,\sigma=\uparrow,\downarrow} \left(u_{p,x\sigma} c^{\dagger}_{x\sigma} + v_{p,x\sigma} c_{x\sigma} \right), \tag{4.58}$$

$$d_{p} = \sum_{x,\sigma=\uparrow,\downarrow} \left(v^{*}_{p,x\sigma} c^{\dagger}_{x\sigma} + u^{*}_{p,x\sigma} c_{x\sigma} \right). \tag{4.59}$$

4.4.2 Tunneling Rate From The Density Matrix

From Eqs. (4.35) and (4.36), the tunneling rate can be expressed as the square of wave function coefficients, based on Eqs. (4.58) and (4.59). So, the expression in Eq. (4.35) and (4.36) is technically $\left| \langle \psi^{e}_{\epsilon_p} | x \rangle \right|^2$ and $\left| \langle \psi^{h}_{\epsilon_p} | x \rangle \right|^2$, respectively. Note that $\psi^{e}_{\epsilon_p}$ ($\psi^{h}_{\epsilon_p}$) is the electron (hole)-part of wave function with eigen-energy ϵ_p. We choose to use the density matrix approach to find the degeneracy and degenerate wave functions for the tunneling rates.

We start with the density matrix obtained by taking the anti-Hermitian part of the Green's function, i.e.,

$$\rho_{\text{wire}}(\omega) = \left(\frac{G(\omega) - G^{\dagger}(\omega)}{2i\pi} \right) \tag{4.60}$$

or

$$\rho_{\text{wire}}(\omega) \equiv \rho_{wire}(x\sigma\tau; x'\sigma'\tau'; \omega) \tag{4.61}$$

$$= \sum_{n,m} \psi_{n,m}(x\sigma\tau)\psi^{\dagger}_{n,m}(x'\sigma'\tau')\delta(\omega - \epsilon_n) \tag{4.62}$$

(n is the energy-level index and m is the degeneracy index of an energy level), while we express the Green's function in the basis of eigenstates, i.e.,

$$G(\omega) \equiv G_{\text{wire}}(x\sigma\tau; x'\sigma'\tau'; \omega) \tag{4.63}$$

$$= \left(\hat{H}_{\text{BdG}}(\omega) - \omega + i\eta\right)^{-1} \tag{4.64}$$

$$= \sum_{p} \frac{\psi_p(x\sigma\tau)\psi^{\dagger}_p(x'\sigma'\tau')}{\epsilon_p - \omega + i\eta} \tag{4.65}$$

$$= \underbrace{\sum_{p} \psi_p(x\sigma\tau)\psi^{\dagger}_p(x'\sigma'\tau')P(\frac{1}{\epsilon_p - \omega})}_{\text{Hermitian}} + \underbrace{i\pi \sum_{p} \delta(\omega - \epsilon_p)\psi_p(x\sigma\tau)\psi^{\dagger}_p(x'\sigma'\tau')}_{\text{anti-Hermitian}}, \tag{4.66}$$

where the linewidth η is assumed to be infinitesimal. We can pick out the sub-density matrix at energy level ϵ_n by integrating the density matrix over the bound state range $[\epsilon_n - a, \epsilon_n + b]$, i.e.,

$$\rho^{(n)}_{\text{wire}}(x\sigma\tau; x'\sigma'\tau') \equiv \int_{\epsilon_n - a}^{\epsilon_n + b} \rho_{\text{wire}}(\omega) d\omega \tag{4.67}$$

$$= \sum_{m} \psi_{n,m}(x\sigma\tau)\psi^{\dagger}_{n,m}(x'\sigma'\tau'). \tag{4.68}$$

Note that the integration grid needs to be much finer than the linewidth η, so the numerical discrete integration can be close to the continuous integration. The benefit of using density matrix is that we can find the degenerate wave functions of energy ϵ_n by diagonalizing the sub-density

matrix $\rho^{(n)}_{\text{wire}}$ and get eigenvalues λ_m and eigenwave function $\phi_{n,m}$. Then we can express the sub-density matrix as

$$\rho^{(n)}_{\text{wire}}(x\sigma\tau; x'\sigma'\tau') = \sum_m \lambda_m \phi_{n,m}(x\sigma\tau)\phi^{\dagger}_{n,m}(x'\sigma'\tau'). \tag{4.69}$$

Comparing Eqs. (4.67) and (4.69), we can get the effective wave function of degeneracy label m of energy ϵ_n:

$$\psi_{n,m}(x\sigma\tau) = (\lambda_m)^{1/2}\phi_{n,m}(x\sigma\tau). \tag{4.70}$$

By default, we will get $(4N_{\text{tot}})$ of λ_m by diagonalizing $\rho^{(n)}_{\text{wire}}(x\sigma\tau; x'\sigma'\tau')$ with the dimension $(4N_{\text{tot}}) \times (4N_{\text{tot}})$, if N_{tot} is the number of lattice site. In order to get the correct degeneracy for the bound states, we need to technically set some threshold for λ_m, i.e., only those degenerate states with λ_m larger than the threshold can be picked as the degenerate states we are going to include into the calculations. This threshold is also kind of constrained by the linewidth of the Green's function η in Eq. (4.63). When η is small, the peak of DOS is very sharp and narrow, even a small threshold can select the eigenvalue λ_m precisely. On the other hand, when η is larger, the peak of DOS becomes broadened, then we need a higher threshold to select out the positions of the central peaks. This threshold for λ_m should be universally the same over the whole parameter space, in order to make sure the conductance depends only on the LDOS at both ends of the nanowire near zero energy.

The above formula Eq. (4.70) applies to the bound states below the gap. For SC states (above the gap before the gap collapses) and metallic states (after the gap collapses), the integra-

tion range in Eq. (4.67) will be a bit different, i.e.,

$$\rho^{(n)}_{\text{wire}}(x\sigma\tau; x'\sigma'\tau') \equiv \int_{\epsilon_n-\Delta\epsilon_{n-1}/2}^{\epsilon_n+\Delta\epsilon_n/2} \rho_{\text{wire}}(\omega)d\omega \tag{4.71}$$

$$\approx \rho_{\text{wire}}(\epsilon_n)\left(\frac{\Delta\epsilon_n + \Delta\epsilon_{n-1}}{2}\right) \tag{4.72}$$

$$\approx \rho_{\text{wire}}(\epsilon_n)\cdot\Delta\epsilon_n \tag{4.73}$$

$$= \sum_m \lambda_m \phi_{n,m}(x\sigma\tau)\phi^\dagger_{n,m}(x'\sigma'\tau')\cdot\Delta\epsilon_n \tag{4.74}$$

with the energy spacing picked as

$$\Delta\epsilon_n \equiv \epsilon_n - \epsilon_{n-1} \approx \frac{D_n}{\rho_{\text{SC}}(\epsilon_n)V_{\text{SC}}}, \tag{4.75}$$

where the presumed degeneracy D_n is the size of the density matrix, the bulk BCS DOS of the superconductor $\rho_{\text{SC}}(\epsilon_n)$ is

$$\rho_{\text{SC}}(\epsilon) = \frac{2\rho_F\epsilon}{\sqrt{\epsilon^2 - \Delta(V_z)^2}}\theta\left[\epsilon - \Delta(V_z)\right], \tag{4.76}$$

where ρ_F is the DOS at Fermi level. V_{SC} is defined from the total DOS above the SC gap as

$$\rho_{\text{tot}}(\epsilon) = V_{\text{SC}}\rho_{\text{SC}}(\epsilon). \tag{4.77}$$

This total DOS is under the assumption that the superconductor is much larger than the nanowire so that the component of the wave function in the nanowire is negligible. After the superconduct-

ing gap collapses, i.e., $\Delta(V_z > V_c) = 0$, Eq. (4.76) reduces to

$$\rho_{\text{metal}}(\epsilon) = 2\rho_F, \tag{4.78}$$

a constant. Note that the factor 2 here is due to the spins.

To avoid the singularity at $\rho_{\text{SC}}(\epsilon_n = \Delta)$ [check out Eq. (4.76)], we define each energy level (for SC states and metallic states) as follows. First, we define the states' density (states existing per unit volume) as

$$F(\epsilon) \equiv \int_0^{\epsilon} \rho_{\text{SC}}(x)dx = \int_{\Delta}^{\epsilon} \frac{2\rho_F x}{\sqrt{x^2 - \Delta^2}}dx = 2\rho_F\sqrt{\epsilon^2 - \Delta^2}. \tag{4.79}$$

At the same time, $F(\epsilon_n)$ can also be written as

$$F(\epsilon_n) = \frac{1}{V_{\text{SC}}} \sum_{m \leq n} D_m, \tag{4.80}$$

where D_m is the degeneracy of ϵ_m for $\epsilon_m \leq \epsilon_n$. (Note that $\epsilon_1 = \Delta + 0^+$.) By equating Eqs. (4.79) and (4.80), we can find the energy level (for SC states and metallic states) is at

$$\epsilon_n = \sqrt{\Delta^2 + (\frac{\sum_{m \leq n} D_m}{2\rho_F V_{\text{SC}}})^2}. \tag{4.81}$$

The benefit from the technical side is that we only need coarse profiles of DOS. The DOS does not need to have very sharp and precise peaks of each of the energy states. We can just presume there are a lot of degenerate states occupying one dominant peak. The details, which may not be precisely known for the experimental system, would not be crucial in such a situation.

4.5 Numerical Results

In this section, we will use the formula derived from Sec. 4.2.4 to calculate the CB conductance from single-electron tunneling processes similar to the one shown in Fig. 4.2(a) and discussed in the beginning of the chapter. In the strong CB limit, transport can only occur near a degeneracy between the energy of the SC island with N and $N+1$ electrons. This occurs for magnetic fields that are large enough to reduce the SC gap below the charging energy [91, 115]. The range of Zeeman field over which the conductance is shown [similar to Fig. 4.2(a)] is thus limited to the range where the $2e$ periodic CB peaks seen at small Zeeman field are split. As mentioned in the discussion of the results in Fig. 4.2, the CB conductance depends on many details of the Hamiltonian such as soft gap, self-energy, quantum dots, etc. To dig into each factor, we will systematically study the contribution of various mechanisms and ingredients used in Fig. 4.2 by changing one parameter at one time from the reference case shown in Fig. 4.3.

The reference result shown in Fig. 4.3 is calculated from the Hamiltonian described in Sec. 4.4.1 with the following parameters: the temperature $T = 0.01$ meV, the nanowire length $L = 1.5$ μm (150 sites, with the lattice space $a = 10$ nm), the hopping strength $t = 25$ meV, the SC gap at zero Zeeman field $\Delta_0 = 0.9$ meV, the SC collapsing field $V_c = 4.2$ meV, the spin-orbit coupling constant $\alpha = 2.5$ meV, the chemical potential $\mu = 2.5$ meV, the self-energy coupling constant $\lambda = 1.4$ meV, the TQPT field is theoretically at $V_{\text{TQPT}} = \sqrt{\lambda^2 + \mu^2} = 2.87$ meV for this parameter choice, the QD potential height at the left end $V_D = 1.0$ meV, the QD potential height at the right end $V_D = 4.0$ meV, and the two QD widths are both $l_D = 0.26$ μm. The tunneling barrier induced by the lead occupies $N_{\text{barrier}} = 20$ nm (2 sites), with the energy height $E_{\text{barrier}} = 10$ meV. DOS at Fermi level $\rho_F = 0.1$ $(\mu m^3 \cdot \text{meV})^{-1}$, SC bulk volume $V_{\text{SC}} = 10^5$ μm^3, and the

upper bound of energy level is 2.5 meV (roughly 3 times larger than Δ_0). The numerical results in this work will use variations around these standard parameters as described in the various sub-sections. Our choice of parameters is generic for the currently used experimental Majorana nanowire systems.

For all the results in this chapter: Panel (a) shows the Coulomb-blockade conductance as a function of the gate-induced charge number n_g and the Zeeman field V_z. We show the calculated CB conductance for two periods in n_g space, which has identical conductance pattern, thus explicitly verifying the periodicity of the conductance shown in Sec. 4.2.4. Panel (b) is the regular QPC tunnel conductance probed locally from the left lead as a function of the bias voltage V and the Zeeman field V_z without CB. Panel (c) is the energy spectrum as a function of Zeeman field V_z, which is aligned with the conductance in Panel (a). The spectrum in Fig. 4.3(c) is identical to the one in Fig. 4.2(c) below the TQPT field [marked by the dashed line at the lower Zeeman field V_z], where there is a closure of the bulk spectrum. The $1e$ periodic conductance features in Fig. 4.3(a) showing up above TQPT are found to be brighter than in the case of the Fig. 4.2(a), and show an abrupt drop in intensity following the Zeeman field V_c [marked by the dashed line at the higher Zeeman field V_z], where the superconductivity of the parent Al SC is destroyed. The drop in intensity of the $1e$ periodic conductance peak in Fig. 4.3(a) is a result of a transition from transport through MBSs suggested in earlier works [91, 115] to $1e$ periodic CB transport in a normal metal [130]. The enhanced CB peak in Fig. 4.3(a) is a result of resonant transport through MBS, similar to the case in quantum dots [130], and has been discussed in more detail in sub-section 4.3.2.

Panel (d) is obtained by tracing the maximum conductance value n_g for each V_z value from Panel (a) for both even and odd N, and then calculating the absolute value of difference of

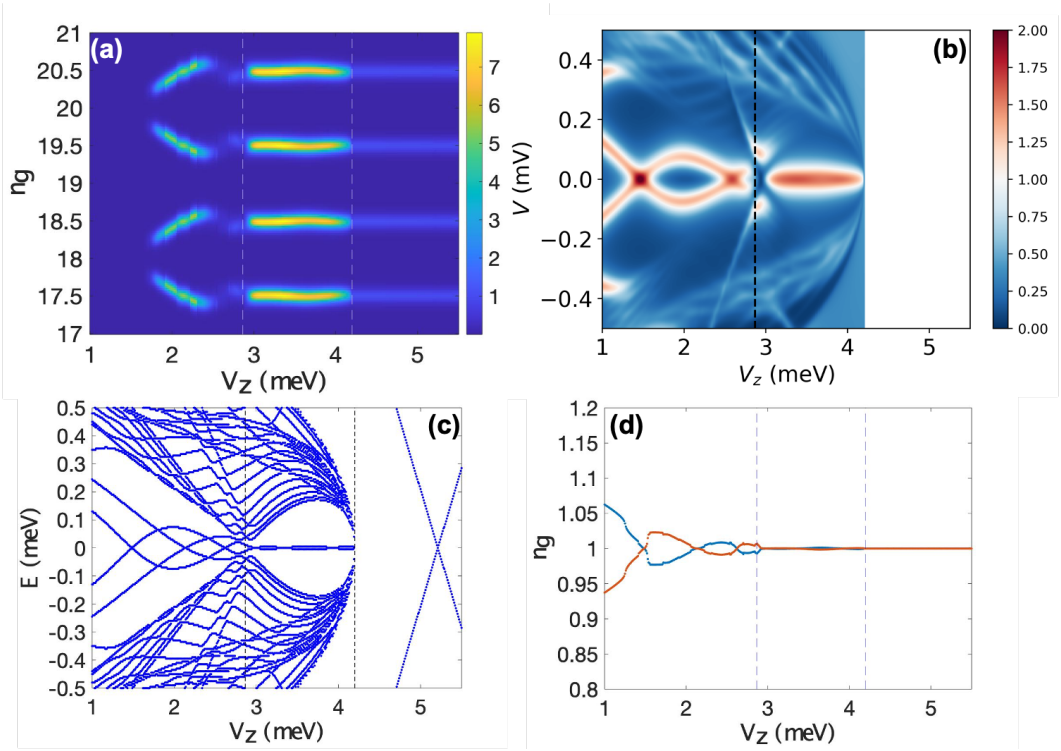

Figure 4.3: The reference case: We will use this set of results as reference for the later results in this section. The difference from Fig. 4.2 is that this set of result does not have soft gap. The parameters are: the temperature $T = 0.01$ meV, the wire length $L = 1.5$ μm, the SC gap at zero Zeeman field $\Delta_0 = 0.9$ meV, the SC collapsing field $V_c = 4.2$ meV. Other relevant parameters are given in Sec. 4.5. (a) Coulomb-blockade conductance G as a function of the gate-induced charge number n_g and Zeeman field V_z at $E_c = 0.13$ meV. We only show two periods in the range of $n_g \in [17, 21]$. (b) Non-Coulomb-blockade conductance G from the left lead as a function of bias voltage V and Zeeman field V_z. (c) Energy spectrum as a function of Zeeman field V_z. (d) OCPS as a function of Zeeman field V_z that is extracted from the vertical peak spacing in panel (a).

these two tracking n_g for both even and odd N. Comparing the positions of the dashed lines in Fig. 4.3(d) with the energy spectrum shown in Fig. 4.3(c), we see that the OCPS arises from the ABS states before the TQPT. The oscillatory splitting of ABSs at each end appears in the local tunneling conductance spectrum at the left lead as seen in Fig. 4.3(b) though the oscillation in this case does not show significant suppression with Zeeman potential. On the other hand, the decreasing OCPS as in Fig. 4.3(d) demonstrates the lobes coming from the two ABSs at both ends exhibited in Fig. 4.3(c). Therefore, OCPSs, which we obtain from the CB conductance in Panel (a), give information about the non-local states, rather than just local states. The non-local transport through a pair of localized levels at each end, which is what is responsible for the shift of the energy of the resonance between the two ABSs, is described in more detail by Eq. (4.51) in Sec. 4.3.3. The main conclusion in our model, where occupation of one ABS is allowed to relax to the other ABS, is that the intensity of the transport peak is suppressed by the energy difference between the two ABSs relative to temperature. This is in contrast to the case where such relaxation is forbidden [91] and non-local transport requires both ABSs to be near zero energy relative to temperature. Both these models would lead to suppression of conductance from ABS states for Zeeman field in the beginning of the range in Fig. 4.3(a) [and Fig. 4.2(a)] where the ABS energy difference is much larger than temperature.

Aside from demonstrating the ideal case (the most similar to the experimental data) as in Fig. 4.2, we will also discuss different effects by changing various parameters relative to the reference case shown in Fig. 4.3, such as wire length, temperature, chemical potential, SC collapsing field, with and without self-energy, and with and without QDs, in the following subsections of Sec. 4.5.

4.5.1 Soft-gap Dependence

Most of the CB experiments [91, 113, 114] in nanowires do not show the abrupt drop in the $1e$ periodic conductance seen in the ideal case plotted in Fig. 4.3(a). Additionally, as discussed in Sec. 4.3.4 as well as in previous work [115], the conductance into the ideal MBS seen in Fig. 4.3(a) is expected to have a significantly higher intensity than the $2e$ periodic conductance from Cooper-pair transport. Such an enhanced intensity is not seen in experiments [91, 113, 114], leading to a contradiction between theory and experiment. These issues are resolved in the calculated conductance in Fig. 4.2, in which the soft SC gap is considered in the topological regime completely. The CB conductance difference of $1e$ transition between the topological regime and the normal-metal regime (i.e., regime above V_c) do not show any visible difference. Clearly, soft gap plays a key role in the experimental CB phenomenology, and brings agreement between theory and experiment.

Physically, the soft SC gap arises from impurity-induced bound states in the SC that is subject to a strong Zeeman field. Experimentally, Majorana nanowires always manifest soft gaps at finite magnetic fields even if the gap is hard at zero field. We model the soft gap phenomenologically by splitting the superconductivity of the proximity-inducing superconductivity into two parts with two different gaps $\Delta_1(V_Z)$ and $\Delta_2(V_Z)$ with different critical Zeeman fields such that

$$\Delta_1(V_z) = \Delta_0\sqrt{1-(V_z/V_{\text{TQPT}})^2}, \tag{4.82a}$$

$$\Delta_2(V_z) = \Delta_0\sqrt{1-(V_z/V_c)^2}. \tag{4.82b}$$

The SC gap collapse is thought to arise from the magnetic field entering the parent SC (i.e.,

Al in these CB experiments), destroying the parent superconductivity and hence all Majorana physics. The soft gap regime ($V_{\text{TQPT}} < V_z < V_c$) is characterized by weakened SC, which we model using a self-energy that is as an average of the self-energy from a clean SC and that from a normal metal. The soft gap is the generic experimental situation in Majorana nanowires at finite magnetic field values even if the zero field system has a hard SC gap. With this choice, the non-vanishing sub-gap density of states is generated in the bulk SC above $V_z > V_{\text{TQPT}}$ from the closing of the first SC gap Δ_1, which is given by

$$\rho_{\text{SC}}(\epsilon) = \frac{1}{2}\left\{ \frac{2\rho_F}{\sqrt{\epsilon^2 - \Delta_1(V_z)^2}}\theta(\epsilon - \Delta_1(V_z)) + \frac{2\rho_F}{\sqrt{\epsilon^2 - \Delta_2(V_z)^2}}\theta(\epsilon - \Delta_2(V_z)) \right\}. \tag{4.83}$$

At the same time, the system remains superconducting below $V_z < V_c$ from the second superconducting part Eq. (4.82b). We will then follow the same procedure as Eqs. (4.79)-(4.81) to obtain the energy levels within the soft-gap regime, i.e., $\Delta_1(V_z) < \epsilon < \Delta_2(V_z)$, and the hard gap regime i.e., $\epsilon > \Delta_2(V_z)$, as before. The two SC gaps $\Delta_j(V_z)$ also correspondingly modify the SC self-energy in Eq. (2.3) to a form which averages between the two SC gaps as in Eq. (4.83).

The effect of the soft SC gap on the CB conductance is a reduction of the peak height associated with the MBS in the topological regime of the Zeeman field ($V_{\text{TQPT}} < V_z < V_c$) from Fig. 4.3(a) to Fig. 4.2(a). For the parameters chosen in Fig. 4.2(a), the MBS conductance is found to be almost identical to the normal state conductance above $V_z > V_c$, which appears to be the case in the experimental data [91, 113]. Our results suggest that an MBS peak height comparable to the normal CB peak at higher Zeeman field would be indicative of a soft gap. While the precise matching of the MBS and normal state CB peaks might be a result of our parameter choices, the smooth intensity variations of the CB peak in experiments [91, 113] suggest the emergence

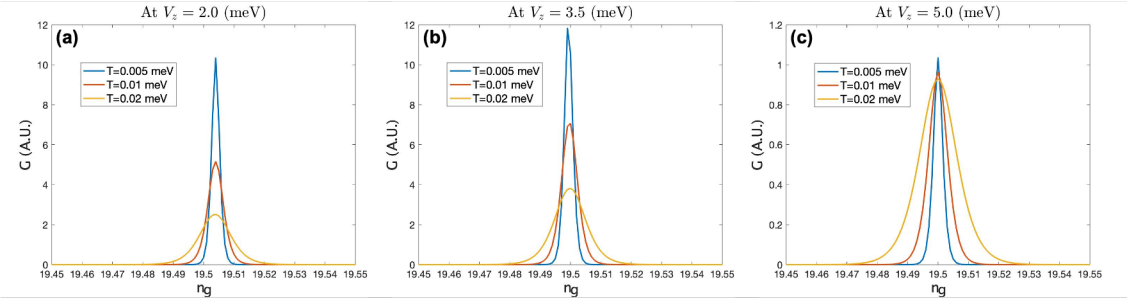

Figure 4.4: Line cuts of the conductance as a function of the gate-induced charge number n_g (i.e., Fig. 4.3), for fixed Zeeman fields V_z, with different temperature values $T = 0.005$ meV, $T = 0.01$ meV, and $T = 0.02$ meV in a single panel. (a) At $V_z = 2.0$ meV, the nanowire is in the Andreev-bound-state/trivial regime. (b) At $V_z = 3.5$ meV, the nanowire is in the Majorana/topological regime. (c) At $V_z = 5.0$ meV, the nanowire is in the normal-metal regime.

(possibly gradual) of a soft SC gap at some Zeeman field above the TQPT. This is of course the experimental phenomenology observed in the usual tunneling spectroscopy of all Majorana nanowires studied so far, where the SC gap always becomes monotonically softer with increasing magnetic field.

4.5.2 Temperature Dependence

As discucssed in Sec. 4.3.2, the $1e$ periodic CB peaks arising from MBS and normal metal behavior show, respectively, an inverse and vanishing temperature dependence of the CB peak height. This is a characteristic difference of a CB peak arising from a resonant bound state or a continuum of states [127, 130]. In Fig. 4.4(a), $V_z = 2.0$ meV, which is in the topologically-trivial regime below TQPT, the conductance peak heights for $T = 0.005$, 0.01, and 0.02 meV are roughly 10, 5, 2.5 in arbitrary units. As explained in Sec. 4.3.1, the overall scale of the conductance in our work is determined by the tunneling parameter τ. Our results can be compared

to experiment by setting the normal state CB conductance for $V_z > V_c$ to the normal-state tunnel conductance. Since the CB conductance peaks arise from ABSs, which are isolated bound states, the peak heights vary inversely with temperature as discussed in Sec. 4.3.2 [127, 130]. A similar temperature dependence is seen for the resonance in the topological regime ($V_z = 3.5$ meV) in Fig. 4.4(b), where the peak heights are approximately 12, 7, and 3.5 at $T = 0.005$, 0.01, and 0.02 meV, respectively. This is in contrast to the CB conductance peak in the normal-metal regime at $V_z = 5.0$ meV, which is shown in Fig. 4.4(c), where we find the peak heights to be almost temperature independent as with normal metal CB (see Sec. 4.3.2) [127, 130]. The results in Fig. 4.4 show that the temperature dependence of the CB peaks can be used to distinguish between $1e$ periodic CB peaks arising from MBSs or trivial non-superconducting CB effect in regular metallic grains.

4.5.3 Length Dependence

In Fig. 4.5, we decrease the nanowire length to $L = 1.0$ μm, compared to Fig. 4.3 ($L = 1.5$ μm). The Majorana oscillations between the two dashed lines in Fig. 4.5 become more obvious in the shorter wire, which satisfies the trend of the Majorana splitting $e^{-2L/\xi}$ [81] which is necessarily enhanced in shorter wires indicating an exponential weakening of the topological protection. Due to the Majorana splitting, the lobes of the OCPS, which project the combination of the lowest-energy states on both ends, start to increase as soon as we enter the topological regime for the shorter wire. On the other hand, Majorana oscillation is suppressed for the longer wire, as in Fig. 4.3 for the case of $L = 1.5$ μm. Therefore, we can see that lobes of the OCPS for $L = 1.5$ μm decrease monotonously as the Zeeman field increases, while the counterparts of

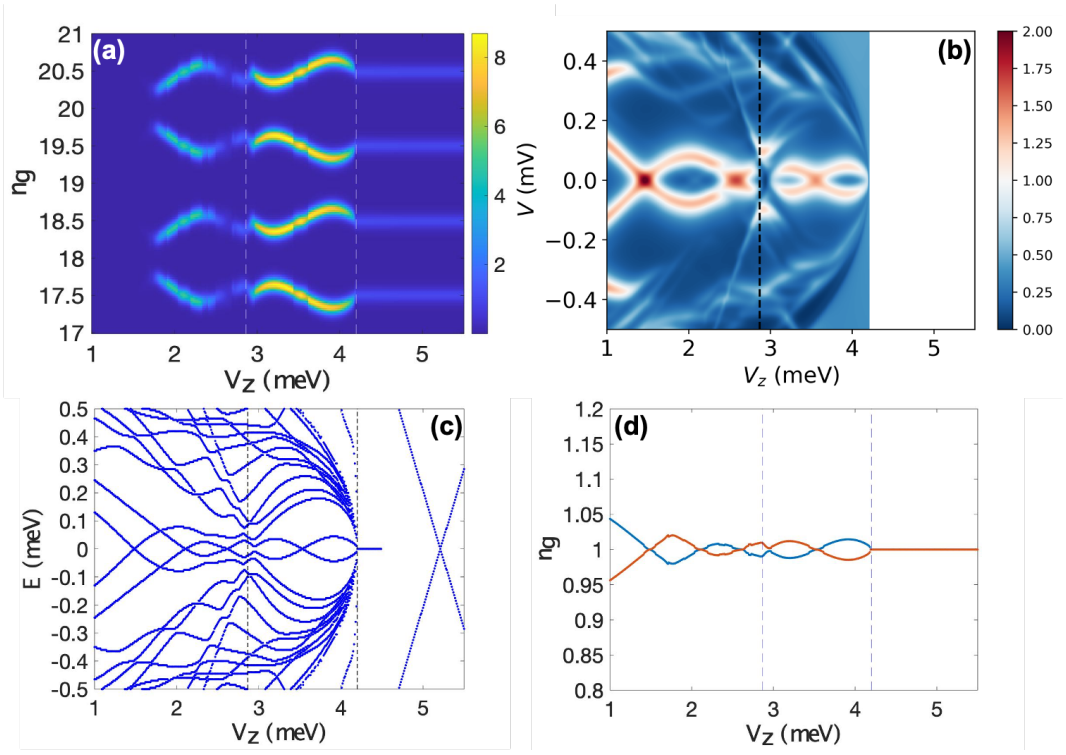

Figure 4.5: This set of results has the shorter wire length $L = 1.0$ μm, while keeping all the other parameters the same as Fig. 4.3. (a) Coulomb-blockade conductance G as a function of the gate-induced charge number n_g and Zeeman field V_z at $E_c = 0.13$ meV. (b) Non-Coulomb-blockade conductance G as a function of bias voltage V and Zeeman field V_z. (c) Energy spectrum as a function of Zeeman field V_z. (d) OCPS as a function of Zeeman field V_z.

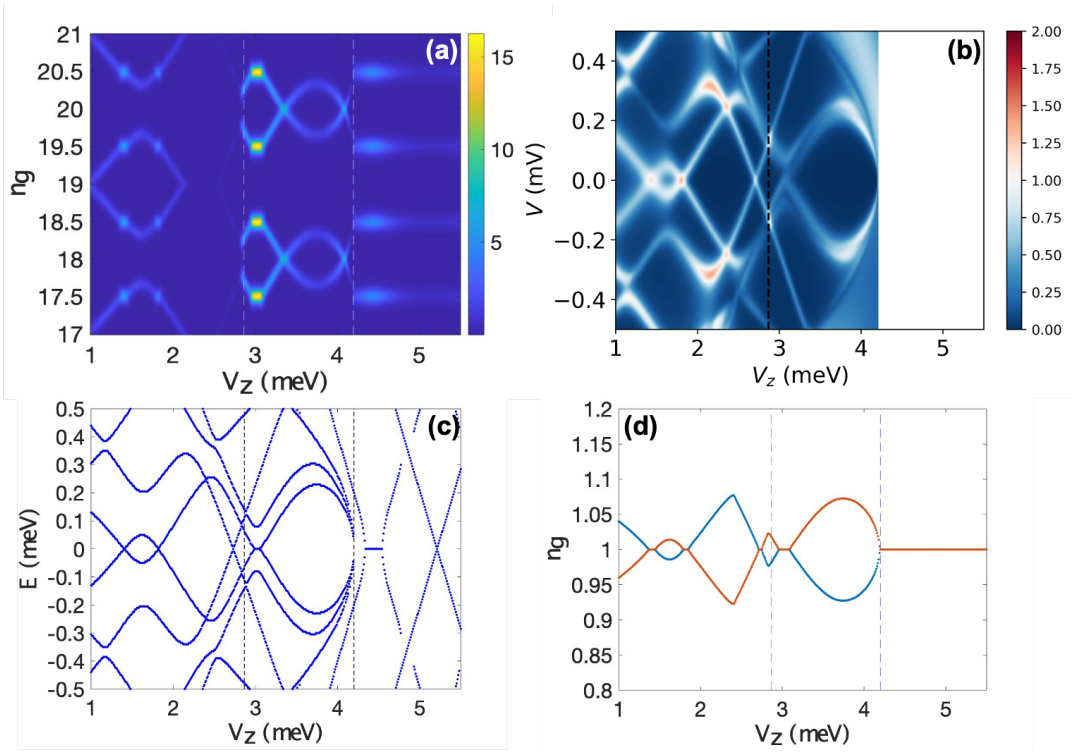

Figure 4.6: This set of results has the shorter wire length $L = 0.6$ μm, while keeping all the other parameters the same as Fig. 4.3. (a) Coulomb-blockade conductance G as a function of the gate-induced charge number n_g and Zeeman field V_z at $E_c = 0.13$ meV. (b) Non-Coulomb-blockade conductance G as a function of bias voltage V and Zeeman field V_z. (c) Energy spectrum as a function of Zeeman field V_z. (d) OCPS as a function of Zeeman field V_z.

$L = 1.0$ μm decrease only before the TQPT field. We also expect that the OCPS for the wire length longer than $L = 1.5$ μm will look no different from the one of $L = 1.5$ μm, considering that both ABS and MBS will be even more localized and stable, and thus the oscillations in the topological regime will be suppressed and negligible as in Fig. 4.3. Based on Figs. 4.3(c) and 4.5(c), both of which show the decreasing lowest-lying energies as a function of Zeeman field below the TQPT field (first dashed line), we can also observe that the decreasing lobes of OCPS in Fig. 4.5(d) mainly come from the ABSs induced by the two quantum dots at both ends. The decreasing OCPS coming from the lowest-lying ABSs on both ends will be destroyed when the nanowire is too short so that the ABSs on both ends interfere with each other, such as the $L = 0.6$ μm case in Fig. 4.6.

In Fig. 4.6(a), with shorter nanowire length $L = 0.6$ μm, the conductance peak is visible in the range of Zeeman potential at the lowest end in Fig. 4.6(a), which is in contrast to Figs. 4.2(a), 4.3(a), and 4.5(a), where the conductance is suppressed based on Eq. (4.51) in Sec. 4.3.3 for the longer wire case.

The suppression of the conductance based on Eq. (4.51) in the long wire case is eliminated for shorter wires with length comparable to the coherence (or the localization) length of the bound states. In this case, electrons from either end can tunnel into each of the ABSs so that electron tunneling between the ends of the wire through either of the ABSs described by Eq. (4.46) provides a measurable contribution to the CB conductance in shorter wires such as in Fig. 4.6(a). These results lead to the conclusion that the observation of the dark region at the transition from $2e$ periodic conductance near the lowest part of the Zeeman range shown in the CB conductance plots [e.g. Figs. 4.2(a), 4.3(a), 4.5(a). etc.] can be understood to be a consequence of ABSs at the ends of the wire.

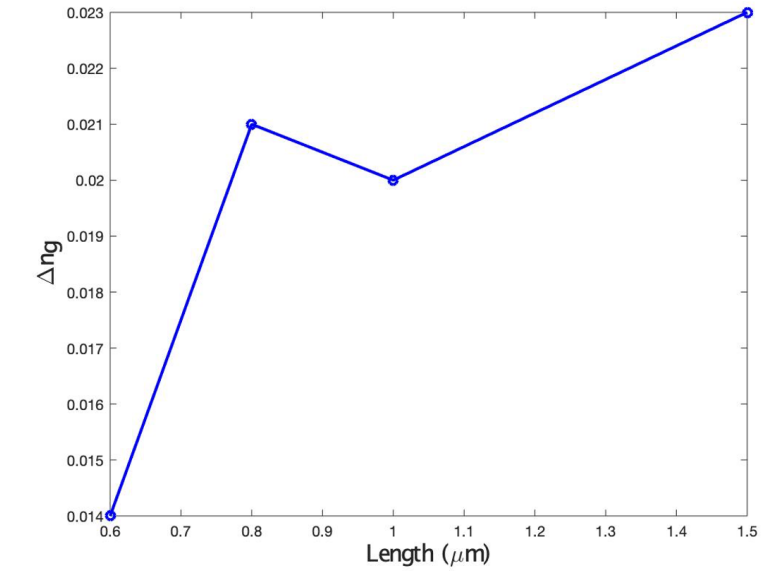

Figure 4.7: The oscillatory amplitude of the first lobe in the OCPS ($|S_o - S_e|/2$) for different wire lengths. All the other parameters are kept the same as Fig. 4.3, except for the nanowire length. The maximum oscillatory amplitude does not display strong length dependence as experimental data.

The length dependence of the first lobe of the OCPS, which is plotted in Fig. 4.7 shows a 40% increase in magnitude of the OCPS with increasing length. This is in contrast to the exponential decrease in the magnitude of OCPS expected from MBS splitting oscillations, which has been claimed to be observed experimentally [91, 114]. Additionally, the change in the OCPS observed by Albrecht *et al.* [91, 114] is two orders of magnitude in contrast to the 40% we see in Fig. 4.7 over the same range of lengths. A similar ($\sim 40\%$) length dependence of OCPS has been obtained in earlier theoretical work [116] using a master-equation approach. The origin of the large discrepancy of the length dependence of our OCPS with experiment is the fact that the OCPS in our models arise from ABSs rather than MBSs, as expected in the experiments. Since the ABS energy is dominated by the profile of the confining potential at the end, we do not expect them to have the exponential length dependence induced by MBS. While this might be a motivation to restrict to models where OCPS from ABSs are absent, one should note that OCPS from MBSs are found numerically to increase or show no significant decrease with increasing applied Zeeman field [116] as seen in Fig. 4.5(d). Thus the OCPS pattern from a single device in the experiment [91, 113, 114] is significantly more consistent with those arising from ABSs [such as Fig. 4.2(d)] than from MBSs. Therefore, while our results show qualitative consistency of the OCPS with single device, the range of models we study cannot reproduce both the decreasing OCPS with field as well as with length seen in the experiments [91, 114]. Again, this is consistent with the earlier theoretical conclusion based on the master-equation approach [116], and we believe that the conclusion of an "exponential protection" made in Ref. [91] is incorrect and is an artifact of using very few samples with each sample having its own different sets of ABS, etc. (i.e., the sample length was not varied *in situ*, but only by going from sample to sample where obviously many things, not just the sample length, are changing in an uncontrolled manner).

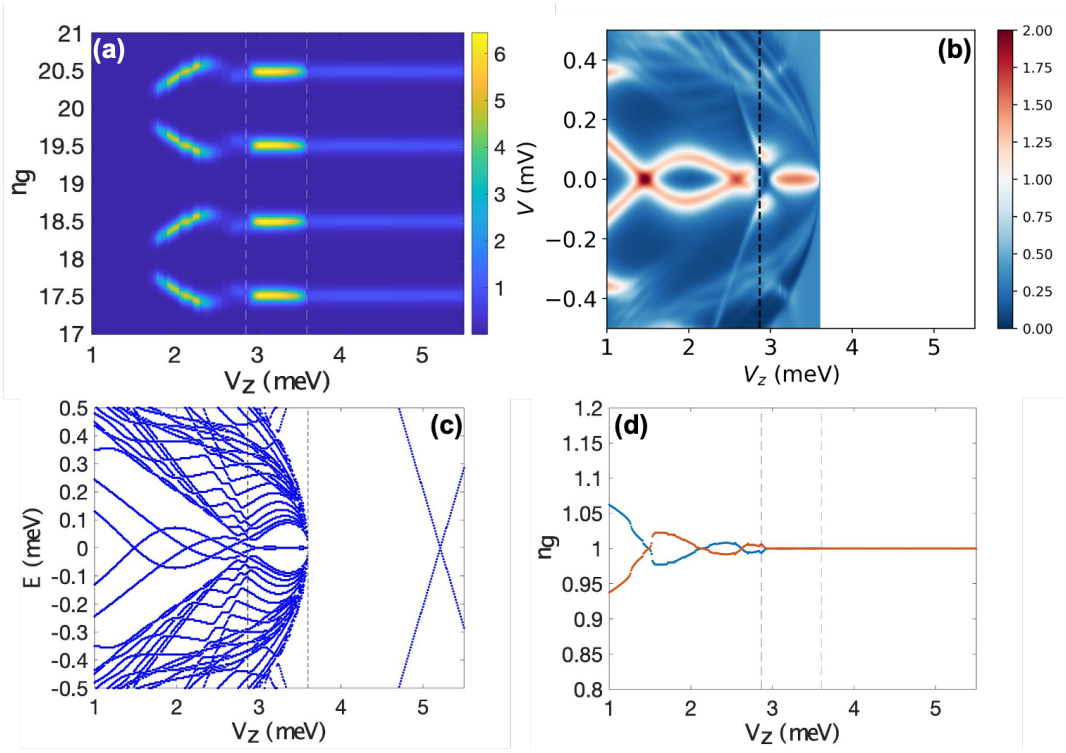

Figure 4.8: This set of results has the lower SC collapsing field $V_c = 3.6$ meV, while keeping all the other parameters the same as Fig. 4.3. (a) Coulomb-blockade conductance G as a function of the gate-induced charge number n_g and Zeeman field V_z at $E_c = 0.13$ meV. (b) Non-Coulomb-blockade conductance G as a function of bias voltage V and Zeeman field V_z. (c) Energy spectrum as a function of Zeeman field V_z. (d) OCPS as a function of Zeeman field V_z.

4.5.4 SC Collapsing Field Dependence

In this subsection, we change the SC collapsing field in Fig. 4.3 from $V_c = 4.2$ meV to lower value $V_c = 3.6$ meV, as in Fig. 4.8, and to higher value $V_c = \infty$, i.e., $\Delta(V_z) = \Delta_0$, as in Fig. 4.9. The value of V_c determines the size of the topological regime relative to the normal metal regime, where the SC gap is destroyed. Since the CB conductance for a normal metal is exactly $1e$ periodic [92, 131–135], a low value of V_c can appear as a suppression of the Majorana splitting oscillations expected in the topological superconducting regime. The range

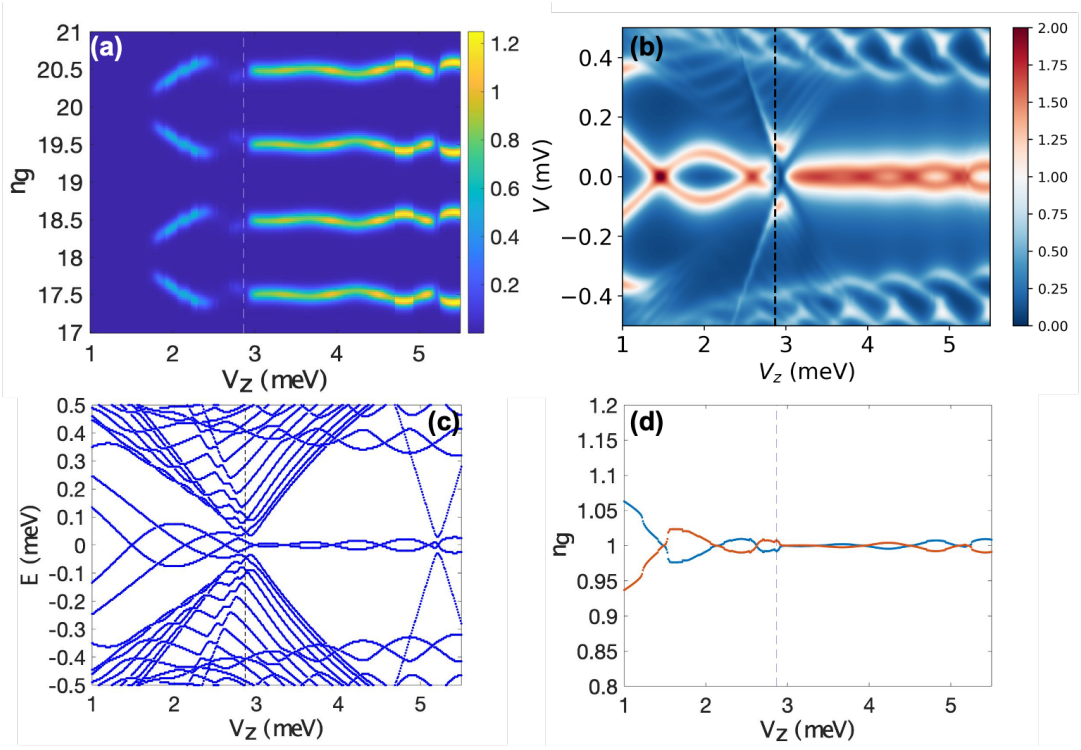

Figure 4.9: This set of results has the infinite SC collapsing field, i.e., $\Delta(V_z) = \Delta_0$, while keeping all the other parameters the same as Fig. 4.3. (a) Coulomb-blockade conductance G as a function of the gate-induced charge number n_g and Zeeman field V_z at $E_c = 0.13$ meV. (b) Non-Coulomb-blockade conductance G as a function of bias voltage V and Zeeman field V_z. (c) Energy spectrum as a function of Zeeman field V_z. (d) OCPS as a function of Zeeman field V_z.

of the topological regime in Figs. 4.3 and 4.8, which starts at the TQPT field and ends at the SC collapsing field V_c (i.e., region between the two dashed lines), does not give enough parameter space for the MBS to be delocalized by the strong external magnetic field. On the contrary, if the parent SC gap is highly robust to the applied magnetic field (i.e., $V_c \gg V_{\text{TQPT}}$) as is the case in Fig. 4.9, the range of topological SC becomes large enough to accommodate an observable range of Majorana splitting oscillations with an amplitude that increases with increasing Zeeman field. Thus, the oscillations in the topological superconducting phase are found to have an amplitude increasing with field, which is in contradiction with the experiments. As discussed in the previous subsections, the experimental observations of OCPSs [91, 113, 114] are more consistent with ABSs which dominate when V_c is not too large relative to V_{TQPT} as in Fig. 4.8 or Figs. 4.2 or 4.3.

4.5.5 Chemical Potential Dependence

Unlike the dependencies discussed so far, changing the chemical potential can substantially change the spectrum of the nanowire even below the TQPT in a way that has been studied in the context of tunneling transport [58, 59, 62, 64, 65, 124]. Aside from changing the value of the TQPT field (the first dashed line), changing the chemical potential μ also modifies the spectrum of subgap ABS energies [59,62,64,65,124]. In addition, the ABSs induced from both ends of the nanowire do not follow a monotonic trend as the chemical potential is varied, due to the fact that the potential heights of QDs are not the same on both ends. Since the OCPS roughly projects the combination of the lowest energies on both ends, it is not guaranteed to generate the decreasing trend of OCPS by simply tuning the chemical potential. We can compare Fig. 4.3 with Figs. 4.10 and 4.11, where the chemical potential changes from $\mu = 2.5$ meV to $\mu = 2.0$ meV and $\mu = 3.0$

meV, respectively. The energy spectrum below TQPT field in Fig. 4.10(c) has no similarity to the one in Fig. 4.3(c), while the structure in Fig. 4.11(c) is similar to Fig. 4.3(c), even the chemical potentials in Figs. 4.10 and 4.11 are both just away from $\mu = 2.5$ meV by 0.5 meV. Nevertheless, the behaviors in the topological regime for these three plot sets do not seem to show a significant difference when the nanowire is long enough to suppress the Majorana splitting oscillation. Thus, as seen in Figs. 4.3(d), 4.10(d), and 4.11(d), the first OCPS lobes arise from end ABS. Comparing the different chemical potential cases in Figs. 4.3, 4.10, and 4.11, we see that while the OCPSs do not show any strong increase with Zeeman potential, observing a strong decrease with Zeeman field as in Fig. 4.3 and seen in experiments [91, 113, 114] depends on the choice of chemical potential.

While the results in Figs. 4.2, 4.3, 4.8, 4.9, and 4.12 suggest the decreasing oscillations of CB conductance peaks are indicative of conductance in the ABS regime, the results in Figs. 4.10 and 4.11 suggest otherwise. These latter results show small decreasing oscillations across the $V_z = V_{\text{TQPT}}$, making it difficult to distinguish the ABS regime from the MBS regime. This is especially so in Fig. 4.11(a), where the CB conductance patterns between the ABS regime and MBS regime look similar (i.e., both display almost $1e$ periodic CB transitions) because the ABSs stay close to zero energy, giving rise to the brightness pattern, which barely has oscillations. This result means that the CB conductance profiles by themselves cannot provide enough information about the difference between the ABS regime and the MBS regime. However, it should be noted that in Fig. 4.11(a), a little patch of darkness near TQPT separates the ABS regime and MBS regime though it is not so visible in the general case. This will be discussed in more detail in Sec. 4.6.1. In general, however, our detailed theoretical results indicate that particular caution is warranted in interpreting experimental CB conductance peaks as arising from MZMs since the

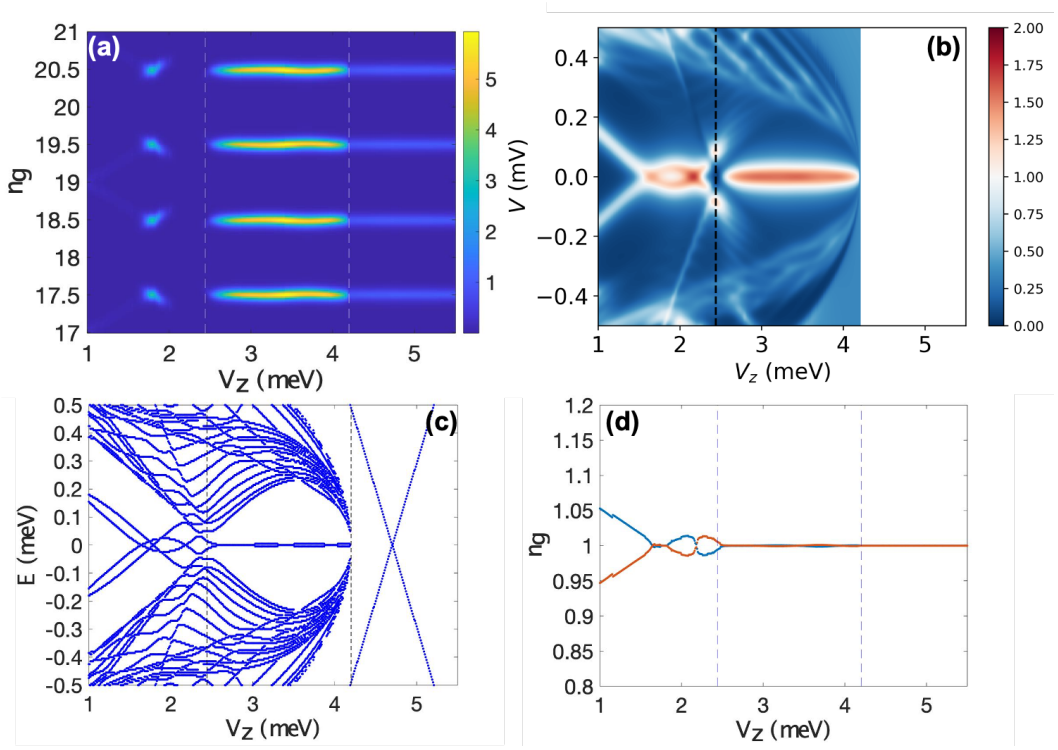

Figure 4.10: This set of results has the lower chemical potential $\mu = 2.0$ meV, while keeping all the other parameters the same as Fig. 4.3. (a) Coulomb-blockade conductance G as a function of the gate-induced charge number n_g and Zeeman field V_z at $E_c = 0.16$ meV. (b) Non-Coulomb-blockade conductance G as a function of bias voltage V and Zeeman field V_z. (c) Energy spectrum as a function of Zeeman field V_z. (d) OCPS as a function of Zeeman field V_z.

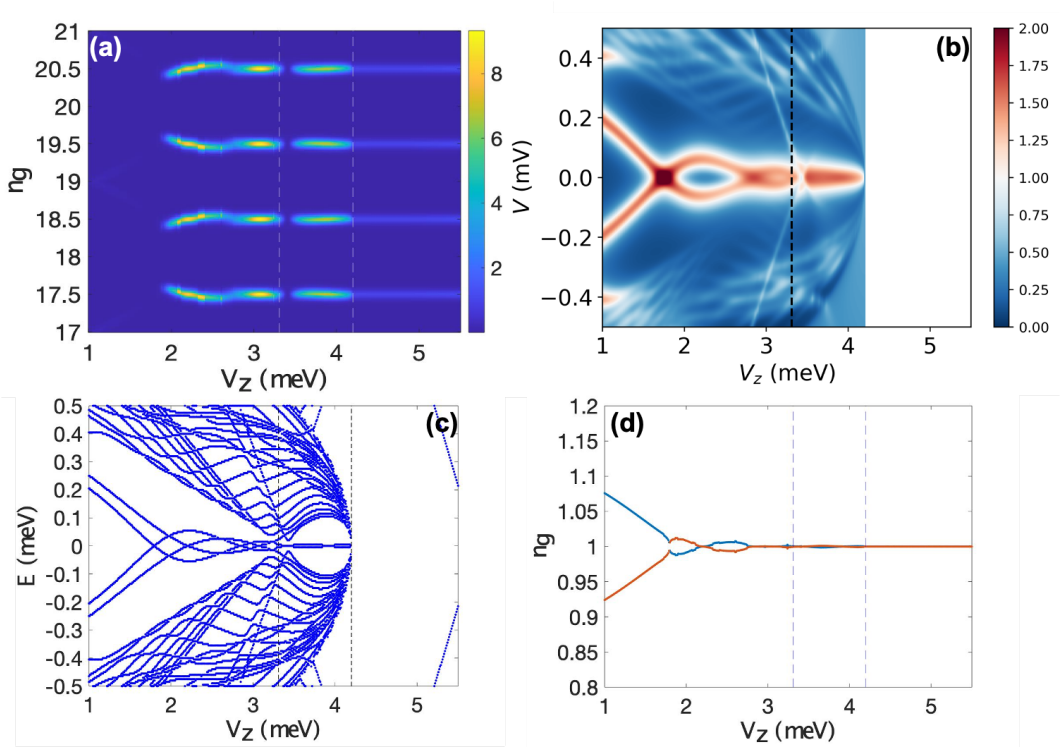

Figure 4.11: This set of results has the lower chemical potential $\mu = 3.0$ meV, while keeping all the other parameters the same as Fig. 4.3. (a) Coulomb-blockade conductance G as a function of the gate-induced charge number n_g and Zeeman field V_z at $E_c = 0.21$ meV. (b) Non-Coulomb-blockade conductance G as a function of bias voltage V and Zeeman field V_z. (c) Energy spectrum as a function of Zeeman field V_z. (d) OCPS as a function of Zeeman field V_z.

distinction between the manifestations of ABS and MBS in CB conductance is rather subtle and small.

4.5.6 Quantum Dot Dependence

In Fig. 4.3, we show the calculated results with two QDs on both ends of the nanowire. In this subsection, we show the results of one QD in Fig. 4.12 by removing the QD on the right end but keeping the left one. We also show the results without any QD in Fig. 4.13. Compared to Fig. 4.12(c), the non-Coulomb-blockade conductance in Fig. 4.12(b) reflects the ABS located at the left end as it is measured from the left lead. We also observe that there is no difference between Figs. 4.3(b) and 4.12(b), even though there are two low-energy ABSs in Fig. 4.3. Both Fig. 4.3(b) and Fig. 4.12(b) only demonstrate the ABS induced from the QD at the left end. So the regular tunnel conductance (without Coulomb blockade) can only provide local information. On the other hand, Fig. 4.3(d) projects the combination of the two ABSs located at both ends, by comparing it with Fig. 4.3(c). Therefore, the OCPS obtained from the Coulomb blockade conductance gives us non-local information that the regular (non-Coulomb-blockade) conductance cannot provide.

In Fig. 4.12(a), the CB conductance peak is suppressed below the TQPT field (first dashed line), relatively lower than the Majorana peak, which lies between the two dashed lines. The diminished conductance associated with the ABSs in Fig. 4.12 arises from the difference in the ABS energies (seen in Fig. 4.12(c)) at the two ends. Such a difference in energies leads to suppression in conductance as seen in Eq. (4.51). The CB conductance intensity increases once the ABS energies approach zero energy and continues to remain high past the TQPT until the SC

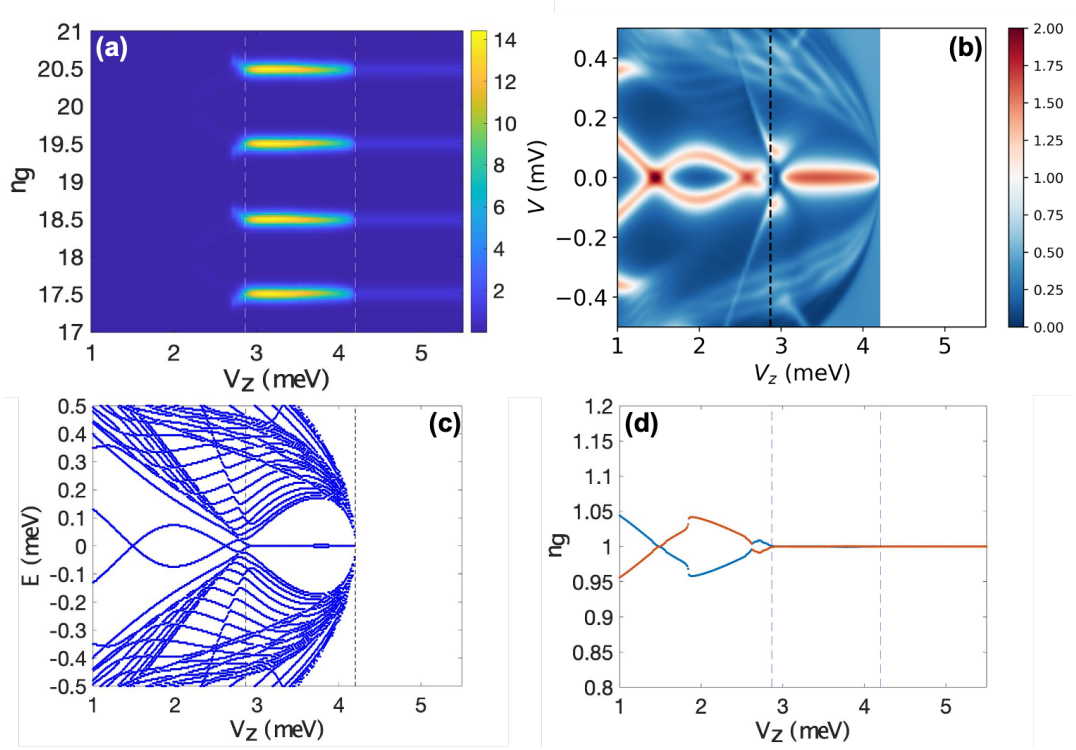

Figure 4.12: This set of results has only one QD on the left end of the wire, while keeping all the other parameters the same as Fig. 4.3. (a) Coulomb-blockade conductance G as a function of the gate-induced charge number n_g and Zeeman field V_z at $E_c = 0.13$ meV. (b) Non-Coulomb-blockade conductance G as a function of bias voltage V and Zeeman field V_z. (c) Energy spectrum as a function of Zeeman field V_z. (d) OCPS as a function of Zeeman field V_z.

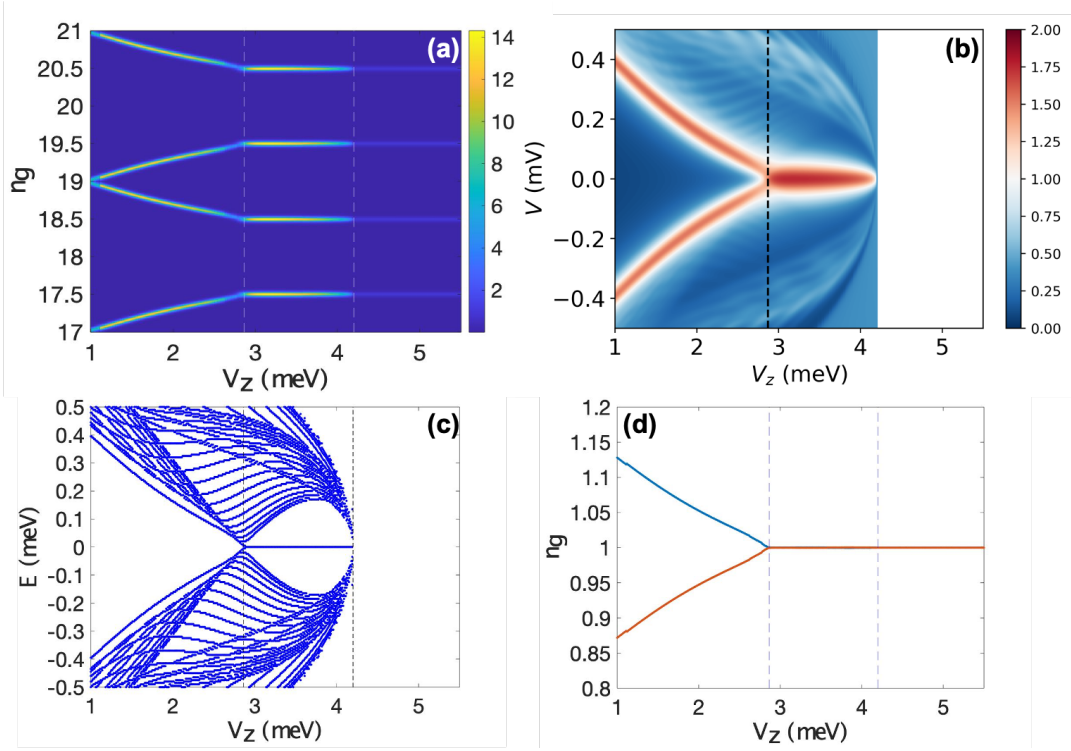

Figure 4.13: This set of results has none QD on both ends of wire, while keeping all the other parameters the same as Fig. 4.3. (a) Coulomb-blockade conductance G as a function of the gate-induced charge number n_g and Zeeman field V_z at $E_c = 0.40$ meV. (b) Non-Coulomb-blockade conductance G as a function of bias voltage V and Zeeman field V_z. (c) Energy spectrum as a function of Zeeman field V_z. (d) OCPS as a function of Zeeman field V_z.

gap closes.

Comparing the OCPS of two-QD case [Fig. 4.3(d)] with the case without QDs [Fig. 4.13(d)], we conclude that the Zeeman-field oscillations of OCPS depend on the presence of QDs. This is consistent with the absence of oscillations in the ABS spectrum in Fig. 4.13. While the MBS spectrum typically shows oscillations with Zeeman energy [136], the splitting amplitude is significantly below the thermal resolution [62] at the temperatures we consider. Indeed, neither the non-CB conductance [Fig. 4.13(b)] nor the OCPS from CB conductance [Fig. 4.13(d)] show any

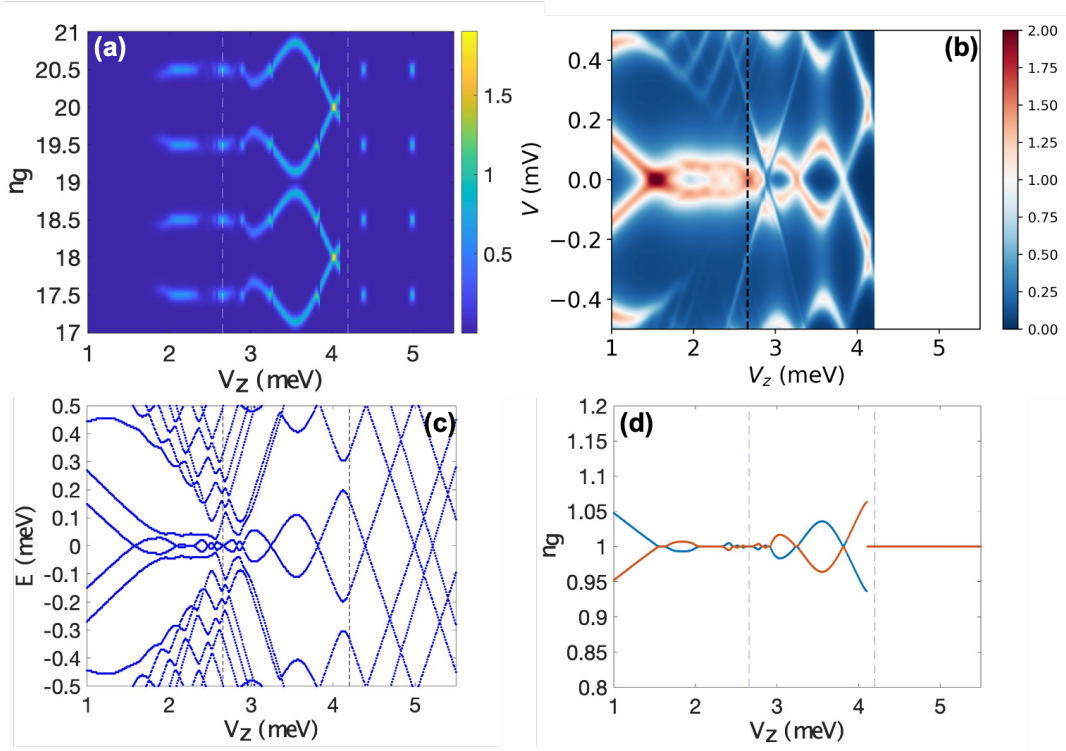

Figure 4.14: This set of results does not include the self-energy, while keeping all the other parameters the same as Fig. 4.3. (a) Coulomb-blockade conductance G as a function of the gate-induced charge number n_g and Zeeman field V_z at $E_c = 0.13$ meV. (b) Non-Coulomb-blockade conductance G as a function of bias voltage V and Zeeman field V_z. (c) Energy spectrum as a function of Zeeman field V_z. (d) OCPS as a function of Zeeman field V_z.

oscillations, which is different from the results in Figs. 4.3 or 4.12, both of which have at least one QD. Therefore, the oscillatory lobes of OCPSs in the experimental data [91, 113, 114] most likely come from the ABSs induced by the QDs.

4.5.7 Self-energy Dependence

In Fig. 4.14, we remove the self-energy term induced by the parent SC. The energy splittings from both ABSs and MBSs are enlarged without self-energy, compared to Fig. 4.3, which

incorporates self-energy. The self-energy suppresses the energy splitting by a factor of $1/(1+\lambda/\Delta)$ [104]. Aside from the effective SC gap Δ being replaced by the self-energy coupling λ, the TQPT field is shifted to $V_{\text{TQPT}} = \sqrt{\lambda^2+\mu^2}$ for the self-energy case, rather than $V_{\text{TQPT}} = \sqrt{\Delta_0^2+\mu^2}$ for the non-self-energy case. According to weak-coupling BCS theory, coherence length is $\xi = \hbar v_F/(\pi\Delta)$, so the coherence length becomes shorter when $\lambda > \Delta$. Therefore, the Majorana splitting, which follows $e^{-L/\xi}$, becomes smaller with parent SC coupling [79, 137]. The subgap states become more localized as we increase the coupling strength λ too. The self-energy generically reduces the Majorana oscillation amplitude above TQPT, but the quantitative suppression depends on many details of the parameters.

The inclusion of self-ernergy may be a key to understanding why MBS oscillations increasing in amplitude with Zeeman field are not observed in OCPS experiments or conventional conductance experiments without CB. For the non-self-energy results in Fig. 4.14, we do not observe the OCPS decreasing with the Zeeman field monotonously. In fact, the splitting in the absence of self-energy seen in Fig. 4.14 is large enough to eliminate any $1e$ periodic features that are seen in the experiments and in Fig. 4.3 beyond a magnetic field which is not large enough to kill SC completely. Whether the almost universal experimental absence of Majorana oscillations with increasing Zeeman field is a consequence of the self-energy effect or simply a manifestation of the dominance of ABS in the experiments is an important question. Obviously, if the experiments are manifesting only ABS and no MBS, there will not be any Majorana oscillations whether self-energy effects are included or not. The current nanowire experiments, including the CB experiments, are certainly more consistent with the physics of ABS being dominant, which provides a natural explanation for why the MBS oscillations are never seen.

4.6 Key Features of Coulomb Blockaded Conductance

In this section, we summarize how the generic features of the experiment can be understood from a compilation of our results in Sec. 4.5 together with the analytical arguments in Sec. 4.3.

4.6.1 Bright-dark-bright Pattern

One of the commonly seen features in the CB experiments [91, 113, 114] is the bright-dark-bright intensity pattern that is seen as the Zeeman field increases. Specifically, the $2e$ periodic CB peaks at small Zeeman field are seen to be bright followed by a dark region, which then becomes bright as the CB resonances approach the purely $1e$ periodic regime. While the numerical results shown in Fig. 4.3-4.14 do not show the $2e$ periodic region, they do show a dark region of suppressed conductance at the lower end of the Zeeman scale corresponding to immediately after the $2e$ periodic region, consistent with experiments. The suppressed conductance seen in our numerical plots in this so-called dark region can be understood from Eq. (4.51), which shows that the conductance intensity will become suppressed when the eigen-energy difference from both ends is larger than the temperature. From the spectrum in Figs. 4.2(c), 4.3(c) and 4.5(c), there are two sub-gap ABSs which are located on both wire ends respectively. The higher-energy subgap ABS suppresses the resonant conductance as the arguments below Eq. (4.51) suggest. Therefore, we are unable to observe the conductance below $V_z = 1.7$ meV. The brightness appears above $V_z = 1.7$ meV, when the energy difference from L and R ends is within the temperature range, i.e., $|\epsilon_L - \epsilon_R| < T$. These numerical results also prove that Eq. (4.51) applies in the long nanowire, where the ABSs on both ends are localized. On the other hand, when the wire is short, the ABSs on both ends are delocalized and one can use Eq. (4.46) instead of Eq. (4.51) to

describe conductance through each of these states. The resulting conductance is no longer suppressed by the energy difference between the ABSs, though it is instead suppressed by the short length. The topological MBS peaks are associated with a single ABS that is therefore described by Eq. (4.46) and shows a bright CB resonance even when split [115]. This Majorana peak (in the absence of a soft gap) described by Eq. (4.46) is the brightest in the CB conductance plot. Thus, the presence of exponential suppression based on Eq. (4.51) can in principle explain the bright-dark-bright feature seen in experiments on long Majorana wires [91, 113, 114] although the experimental wires are unlikely to be in the long wire regime given the rather small induced SC gap.

The mechanism for the dark feature discussed in the previous paragraph is different from that proposed previously [115], where the dark feature resulted from a continuum of delocalized states. The suppression in the latter mechanism arises from the delocalization of the continuum states, as opposed to the localization of the ABSs considered in our work. The numerical results in Figs. 4.3-4.14(a) also contain contribution from continuum states, but only near the TQPT when the bulk gap closes. This is seen as a separate small dark region in the vicinity of the TQPT (dashed line at the lower V_z) in Figs. 4.3-4.14. Since this region is characterized by a large number of states, the numerical treatment of this region requires the generalized Meir-Wingreen formalism described in Sec. 4.2 of this work. One can use this small dark region as a signature to distinguish the ABS regime and the MBS regime, as seen in Fig. 4.11(a). But we can barely pinpoint this small dark patch generically because this signature may be confused with a larger range of dark conductance arising from localized ABSs at the two ends as seen in other CB conductance numerical results, i.e., Panel (a) of Figs. 4.3, 4.5, 4.6, 4.8, 4.9, 4.10, and 4.14. Furthermore, the soft-gap effect in the MBS regime together with certain ABS wave-function

profiles could obscure the darkness associated with the TQPT patch, making the presence of MZM challenging to distinguish, as in Fig. 4.2(a). This further reinforces our earlier comment that CB conductance studies may not be a good experimental technique to discern MBS from ABS.

A separate puzzle that is not immediately resolved by our numerical treatment is the relative intensity between the two bright regions. The first $2e$ periodic bright region results from elastic cotunneling of Cooper pairs and the second one arises from tunneling of electrons. Thus, one expects the second bright region to be brighter than the first region [115], which is quite different from what is seen in experiments [91,113,114]. A potential resolution of this puzzle is provided in this work by details of the proximity-induced semiconductor structure. Specifically as described in Sec. 4.3.1, the normal-state CB conductance at high fields, which is equal to the normal-state conductance, is suppressed in semiconductor structures if the local density of states is suppressed away from an ABS resonance in the semiconductor at low densities. Such a suppression does not affect the virtual elastic cotunneling process since a non-resonant ABS can contribute to Cooper-pair tunneling. Thus, the inclusion of the transmission resonance associated with an ABS can explain the enhanced $2e$ periodic Cooper-pair tunneling. Resolution of this puzzling brightness paradox in the CB experiments is one of the major conceptual achievements of our theory. Our explanation, however, further reinforces the dominance of trivial ABS over topological MBS in the existing Majorana nanowire experiments.

4.6.2 Suppression of Normal Coulomb Blockade Peak Relative to ABS and MBS

The results for the CB conductance in Figs. 4.3, 4.5-4.8 in Sec. 4.5 show $1e$ periodic conductance both from MBSs in the topological region (i.e., $V_{\text{TQPT}} < V_z < V_c$) as well as normal metallic CB for $V_z > V_c$. In all these cases, the MBS conductance peak, being resonant follows Eq. (4.46) and is higher than the normal-state CB conductance described by Eq. (4.48). In principle, this makes the bright $1e$ periodic conductance from MBS even brighter relative to the $2e$ periodic conductance mentioned in the previous subsection. Additionally, such a difference in brightness between the MBS and normal conductance is not seen in experiments [91, 113]. Both these issues get resolved in Fig. 4.2, where we have included the effect of a soft-gap. Such a soft-gap arises from the interplay of disorder and magnetic field on the parent SC [138]. Interestingly, the presence of large oscillations from the ABS states prior to the TQPT suggests the absence of disorder-induced subgap states below the TQPT.

4.7 Summary

We have developed a theory for and numerically calculated the two-terminal conductance of a Majorana nanowire in the CB regime, including all the important realistic effects, such as the soft-gap, SC proximity effect, temperature, nanowire length, SC collapsing field, chemical potential, QDs, self-energy, SC states, and metallic states. The realistic model for the wire used in our work, in certain parameter regimes such as near the TQPT or beyond the critical Zeeman field V_c, contains a large number of low-energy states. In order to compute CB conductance in

this region, we have derived a generalized Meir-Wingreen formula, which is based on assuming the tunneling rate is lower than the equilibration rate in the nanowire. This assumption reduces the complexity of the rate equation formalism from the exponential [116] to linear in the number of low-energy levels. However, the assumption requires an equilibration process that might not be very efficient in the limit of a few levels. We have discussed the resulting differences in Sec. 4.3.2. Our calculation also entirely focuses on the $1e$ tunneling regime and we have only provided analytic estimates for the Cooper-pair tunneling regime relative to the normal-state conductance. The normal-state conductance seen in the high Zeeman field regime of our numerical results thus provides a calibration scale to compare the experimental results.

Our optimal results are summarized by Fig. 4.2(a), which shows an example of the CB conductance that is closest to the experimental results. While this plot excludes the $2e$ periodic Cooper-pair tunneling part of the transport seen at low Zeeman fields as the brightest feature in the experiments [91, 113, 114], our CB conductance plot shows a range of Zeeman field, which starts with darkness followed by a bright region, similar to experiments [91, 113, 114]. By comparing with the energy spectrum shown in Fig. 4.2(c), the dark region in our simulations arises from ABSs, in contrast to the mechanisms studied in earlier works [115]. The CB conductance becomes visible when the ABSs approach zero energy and remains bright in the topological region, where the conductance is due to MBSs, except for a dark patch near the TQPT. At large enough Zeeman field, the SC is driven to normal-state and the CB conductance peak from MBSs crosses over to the $1e$ periodic CB peak of a normal metal. While the normal-metal CB peak is higher than the dark region from ABSs, it is substantially (in all results, except for Fig. 4.2) weaker than the resonant CB peaks for MBSs. We have verified that resonant CB peaks, such as those from MBSs and ABSs, can be distinguished from normal-metal and TQPT-related CB peaks by their

temperature dependence. The difference in intensities between the MBS and normal CB regime, which is not seen in experiments [91, 113], is suppressed in Fig. 4.2 by the introduction of a soft gap, i.e., subgap density of states in the SC that is introduced by semiconductor disorder. The complete bright-dark-bright feature is not naturally included in our numerical simulations since the first bright feature in the experiments results from $2e$ periodic Cooper-pair tunneling. However, we have argued in Sec. 4.3.1 that resonant transmission features associated with the barrier potential can suppress the normal CB conductance (at high Zeeman field) relative to the $2e$ periodic Cooper-pair conductance (at low Zeeman field). Thus, we find that the intensity pattern seen in experiments can be matched by a specific nanowire model in our generalized Meir-Wingreen formalism.

Aside from the intensity fluctuations, the positions of the CB peaks that deviate from $1e$ periodicity provide interesting spectroscopic information, such as MBS splitting [91, 115]. In fact, the observation of such breaking of $1e$ periodicity allows one to verify the absence of quasiparticle poisoning by low-energy subgap states [139]. Following Albrecht *et al.* [91], we have characterized the positions of the peaks through the OCPS [plotted in panel (d) of Figs. 4.2-4.14, except Figs. 4.4 and 4.7]. We find that in the case of ABSs at both ends of the wire, the first lobes of the OCPS result from a combination of both ABSs. This is distinct from tunneling conductance at a single end, which is sensitive to the spectrum only at one end. We find that this model of ABSs at both ends produces OCPS that decreases with increasing Zeeman field. The OCPS arising from MBSs [91, 115, 116], which increases in amplitude with increasing Zeeman field, is suppressed by the inclusion of self-energy from the proximity-inducing SC. By comparing OCPS from models with and without QDs, we find that QDs are necessary to obtain oscillations that decrease with increasing Zeeman field.

We emphasize that the experimentally claimed "exponential protection" in Refs. [91, 114] may be a misleading artifact of the data being taken at very few samples with each sample having its own set of ABS dominating the CB transport. Our work shows that because of the non-universal nature of ABS dominating CB tunneling transport in the currently available SC-SM-QD nanowire samples, there is no universal length dependence in the CB physics. We believe that the strong length dependence in the claimed experimental data can be an artifact of the few samples considered in each of the systems [91, 114]. Since each sample has a totally different parameter set (and not just different length), such experiments can tell us absolutely nothing about the intrinsic length dependence of Majorana physics since all system parameters are varied along with the wire length in such experiments.

To sum up, the qualitative features, i.e., bright-dark-bright intensity patterns as well as decreasing OCPS of CB oscillations in Majorana nanowires, can be understood in terms of our semi-realistic model for the superconductor-semiconductor structure. We found that ABSs at both ends, self-energy and soft gap are all necessary ingredients to explain the features of the experiment. We find that the CB conductance has certain distinct advantages over direct tunneling conductance. Specifically, the CB conductance is sensitive to the lowest-energy states, unlike single-end tunneling conductance which picks up signal from all states. Furthermore, the CB conductance is sensitive to the delocalization of states. Away from zero energy, conductance through localized states is suppressed. An experimental characterization of the temperature dependence of the CB peak intensities would be important to verify the characters of the states contributing to the conductance. An important point to keep in mind in this context is, however, the fact that our current zero-bias conductance theory indicates that CB conductance measurements may not be particularly useful in distinguishing topological MBS signatures from trivial ABS signatures.

Chapter 5: **Conclusion**

Over the last decade, the one-dimensional nanowire of superconductor-semiconductor hybrid structure has attracted a lot of condensed matter physicists because the fault-tolerant Majorana zero modes (MZMs) existing in this nanowire can facilitate the development of topological quantum computer. Since the theoretical model was proposed in 2010, a deluge of experiments has been reported in search of MZMs. While this field is active, and Microsoft Corporation also invests in the Majorana nanowire research, the current experimental results are not solid enough to prove the existence of MZMs as feasible topological qubits. This thesis intends to provide several methods through theoretical calculations and arguments to help the experiments distinguish the topological MZMs.

In Chapter 1, we introduced the Majorana zero modes from the famous toy model, Kitaev chain, to show the properties of MZMs. We also introduced the one-dimensional superconductor-semiconductor nanowire model, which is the main focus of this thesis. Later, we elaborated on the MZM signatures one should observe when the Majorana bound states exist in the nanowire. Finally, three topic-related experiments, i.e., earliest observed ZBCP, quantized conductance, and Coulomb blockade experiments, that motivate the theoretical works in this thesis are also presented.

In Chapter 2, we carried out the standard QPC tunneling conductance simulations with

various potentials that lead to "good", "bad", and "ugly" ZBCPs. Only the "good" ZBCPs arise from the genuine MZMs, but the other two kinds of trivial ZBCPs can still resemble the quantization of MZM-induced ZBCPs. We proposed a new quality factor F to quantify the robustness of quantized ZBCP over the normal-state conductance G_N. This quality factor F is useful to the conductance data because G_z (zero-bias peak) versus G_N is the typical way to show the experimentally-measured data. Since the quantization of ZBCPs is intrinsic for MZMs at low temperatures, small values of F should quantitatively reflect those fine-tuned quantization induced by trivial subgap bound states. The conclusion of this work is that we can use this metric F to distinguish the MZM-induced ZBCPs ($F \geq 2$) from other topologically-trivial ZBCPs, with large SC gaps at low-temperature limits.

In Chapter 3, we demonstrated the numerical results of local conductance from each end of the wire in a Majorana nanowire with one QD embedded near the wire end. Comparing the conductance data obtained from both ends, the one that shows the end-to-end ZBCP correlation, meaning ZBCPs are showing up on both ends, indicates a pair of MZMs is present in the nanowire. In contrast, the one that does not show end-to-end ZBCP correlation, meaning there could be a ZBCP from one end but not the other, indicates this ZBCP does not come from MZMs. In the model we studied, this one-end ZBCP comes from the quantum dot located at the same end. Apart from comparing local tunneling conductance, the same three-terminal system can support cross conductance measurements, which should help identify the TQPT field with the bulk gap closing and reopening signature if the external QD is absent. We suggest the experimentalists carry out the end-to-end conductance correlation measurements and cross conductance measurements together as cross checks for the appearance of MZMs.

In Chapter 4, we studied the Majorana nanowire in the Coulomb-blockade limit by deriv-

ing the generalized version of the Meir-Wingreen formula that applies to a two-terminal system and numerically calculating the CB conductance with all the important realistic effects such as soft gap, self-energy, QDs...etc. Assuming the tunneling rate is below the equilibrium rate of the nanowire, the Meir-Wingreen formula is reduced from exponential complexity to linear complexity, which is at the same level as the QPC tunneling conductance calculation. This computational advantage allows us to include thousands of states in the normal-metal regime or above the SC gap, which should contribute to the CB conductance realistically. With this new theoretical tool, we simulated the experimental features [91, 113, 114], including the "bright-dark-bright" pattern and the "decreasing OCPS as a function of Zeeman field", and explained the mechanisms behind these features. At the same time, we argued that the length-dependent OCPS, which indicates topological protection from MZMs [91], is not consistent with the decreasing OCPS as the Zeeman field increases. In the model we studied, the decreasing OCPS with increasing Zeeman field comes from the multiple subgap Andreev bound states, with self-energy, long wire, and early SC collapsing field suppressing the Majorana oscillations. Since the QD-induced ABSs do not have length dependence, the first amplitude of OCPS should be wire length-independent.

To sum up, we have investigated the non-local transport signatures (i.e., end-to-end conductance correlation and CB conductance) and the robustness of ZBCPs (i.e., quality factors) by simulating the one-dimensional SC-SM model with various realistic effects. Given that topologically-trivial ABSs and disorder-induced subgap states can mimic several signatures of MZMs, we particularly compare the numerical results coming from purely MZMs and results from ABSs or disorder-induced subgap states. We are sure these comparisons can provide realistic references to the experiments, and our theoretical proposals should help experiments anchor the Majorana zero modes in the near future.

Appendix A: **Detailed Derivations for Coulomb Blockade Transport**

A.1 Microscopic Tunneling Rates

The rate of absorption of electrons from lead $\alpha = L, R$ is given by

$$\begin{aligned}\Gamma_N^\alpha &= \tau_\alpha \sum_{i,j} P_N(E_i) \int d\epsilon f(\epsilon - \mu_\alpha)\delta(E_j - E_i - \epsilon) \left|\langle\psi_j|c_\alpha^\dagger|\psi_i\rangle\right|^2 \\ &= \tau_\alpha \sum_{i,j} P_N(E_i) f(E_j - E_i - \mu_\alpha) \left|\langle\psi_j|c_\alpha^\dagger|\psi_i\rangle\right|^2,\end{aligned} \tag{A.1}$$

where $f(\epsilon) = (1 + e^{\beta\epsilon})^{-1}$ is the Fermi function.

Similarly, the rate of emission of electrons into lead α is given by

$$\begin{aligned}\Lambda_N^\alpha &= \tau_\alpha \sum_{i,j} P_N(E_i) \int d\epsilon \left[1 - f(\epsilon - \mu_\alpha)\right] \delta(E_j + \epsilon - E_i) \left|\langle\psi_j|c_\alpha|\psi_i\rangle\right|^2 \\ &= \tau_\alpha \sum_{i,j} P_N(E_i) \left[1 - f(E_i - E_j - \mu_\alpha)\right] \left|\langle\psi_j|c_\alpha|\psi_i\rangle\right|^2.\end{aligned} \tag{A.2}$$

This equation can be simplified and related to the coefficient Γ_N^α by interchanging the indices i, j

and considering the charge state $(N+1)$ as

$$\begin{aligned}
\Lambda^{\alpha}_{N+1} &= \tau_\alpha \sum_{i,j} P_{N+1}(E_j)\left[1 - f(E_j - E_i - \mu_\alpha)\right] \left|\langle\psi_j|c^\dagger_\alpha|\psi_i\rangle\right|^2 \\
&= \tau_\alpha \sum_{i,j} P_{N+1}(E_j) f(E_i - E_j + \mu_\alpha) \left|\langle\psi_j|c^\dagger_\alpha|\psi_i\rangle\right|^2 \\
&= \tau_\alpha e^{-\beta\mu_\alpha} \frac{Z_N}{Z_{N+1}} \sum_{i,j} P_N(E_i) e^{-\beta(E_j - E_i - \mu_\alpha)} f(E_i - E_j + \mu_\alpha) \left|\langle\psi_j|c^\dagger_\alpha|\psi_i\rangle\right|^2 \qquad \text{(A.3)} \\
&= \tau_\alpha e^{-\beta\mu_\alpha} \frac{Z_N}{Z_{N+1}} \sum_{i,j} P_N(E_i) f(-E_i + E_j - \mu_\alpha) \left|\langle\psi_j|c^\dagger_\alpha|\psi_i\rangle\right|^2 \\
&= e^{-\beta\mu_\alpha} \frac{Z_N}{Z_{N+1}} \Gamma^{\alpha}_N.
\end{aligned}$$

A.2 Steady-state Probabilities

The rate of the system leaving the state N must match the rate that is entering into the state N. This leads to the equation

$$P_{0,N} \sum_\alpha (\Gamma^\alpha_N + \Lambda^\alpha_N) = \sum_\alpha (P_{0,N-1}\Gamma^\alpha_{N-1} + P_{0,N+1}\Lambda^\alpha_{N+1}). \qquad \text{(A.4)}$$

Substituting Λ in terms of Γ, the equilibrium condition becomes,

$$P_{0,N} \sum_\alpha (\Gamma^\alpha_N + e^{-\beta\mu_\alpha} \frac{Z_{N-1}}{Z_N} \Gamma^\alpha_{N-1}) = \sum_\alpha (P_{0,N-1}\Gamma^\alpha_{N-1} + P_{0,N+1} e^{-\beta\mu_\alpha} \frac{Z_N}{Z_{N+1}} \Gamma^\alpha_N). \qquad \text{(A.5)}$$

Collecting the rates Γ^α_N, the equilibrium condition becomes

$$\sum_\alpha \Gamma^\alpha_N \left[P_{0,N} - P_{0,N+1} e^{-\beta\mu_\alpha} \frac{Z_N}{Z_{N+1}}\right] = \sum_\alpha \Gamma^\alpha_{N-1} \left[P_{0,N-1} - P_{0,N} e^{-\beta\mu_\alpha} \frac{Z_{N-1}}{Z_N}\right]. \qquad \text{(A.6)}$$

Defining $\Gamma_N^\alpha Z_N = \tilde{\Gamma}_N^\alpha$ and $P_{0,N}/Z_N = \tilde{P}_{0,N}$, the steady-state condition simplifies to

$$\sum_\alpha \tilde{\Gamma}_N^\alpha \left[\tilde{P}_{0,N} - \tilde{P}_{0,N+1} e^{-\beta\mu_\alpha}\right] = \sum_\alpha \tilde{\Gamma}_{N-1}^\alpha \left[\tilde{P}_{0,N-1} - \tilde{P}_{0,N} e^{-\beta\mu_\alpha}\right]. \tag{A.7}$$

The above equation is solved by the detailed balance condition, where both sides of the above equation vanish so that

$$\tilde{P}_{0,N+1} = \tilde{P}_{0,N} \left(\frac{\sum_\alpha \tilde{\Gamma}_N^\alpha e^{-\beta\mu_\alpha}}{\sum_\alpha \tilde{\Gamma}_N^\alpha}\right)^{-1} = \tilde{P}_{0,N} e^{\beta\mu} \left(1 + \frac{\sum_\alpha \tilde{\Gamma}_N^\alpha \left[e^{-\beta(\mu_\alpha - \mu)} - 1\right]}{\sum_\alpha \tilde{\Gamma}_N^\alpha}\right)^{-1}. \tag{A.8}$$

In the limit of a small applied voltage $\mu_\alpha = \mu + V_\alpha$ and expanding to linear order in V_α,

$$\tilde{P}_{0,N+1} = \tilde{P}_{0,N} e^{\beta\mu} \left(1 + \beta \frac{\sum_\alpha \tilde{\Gamma}_N^\alpha V_\alpha}{\sum_\alpha \tilde{\Gamma}_N^\alpha}\right). \tag{A.9}$$

Solving the recursion, we get

$$\tilde{P}_{0,N} = Z_{tot}^{-1} e^{\beta N\mu} \left(1 + \beta \sum_{j<N} \frac{\sum_\alpha \tilde{\Gamma}_j^\alpha V_\alpha}{\sum_\alpha \tilde{\Gamma}_j^\alpha}\right). \tag{A.10}$$

In equilibrium, if $V_\alpha = 0$, the above equations become

$$\tilde{P}_{0,N}^{(eq)} = Z_{tot}^{-1} e^{N\beta\mu}, \tag{A.11}$$

where $Z_{tot} = \sum_N Z_N e^{-N\beta\mu}$ (noting that $\sum_N Z_N \tilde{P}_{0,N}^{(eq)} = 1$).

A.3 Current and Conductance

The current at the left lead is given by

$$\begin{aligned} I &= \sum_N P_{0,N}(\Gamma_N^L - \Lambda_N^L) \\ &= \sum_N P_{0,N}\left(\Gamma_N^L - e^{-\beta\mu_L}\frac{Z_{N-1}}{Z_N}\Gamma_{N-1}^L\right) \\ &= \sum_N \tilde{P}_{0,N}\left(\tilde{\Gamma}_N^L - e^{-\beta\mu_L}\tilde{\Gamma}_{N-1}^L\right) \\ &= \sum_N \tilde{\Gamma}_N^L\left(\tilde{P}_{0,N} - e^{-\beta\mu_L}\tilde{P}_{0,N+1}\right). \end{aligned} \tag{A.12}$$

This current vanished at $V_\alpha = 0$ because the combination of probability factors vanishes. Since the probability factor vanishes to linear order, the conductance can be extracted by expanding this factor to linear order in V_α:

$$\begin{aligned} \tilde{P}_{0,N} - e^{-\beta\mu_L}\tilde{P}_{0,N+1} &= \tilde{P}_{0,N} - (1-\beta V_L)e^{-\beta\mu}\tilde{P}_{0,N+1} \\ &= \tilde{P}_{0,N}\left[1 - (1-\beta V_L)\left(1 + \beta\frac{\sum_\alpha \tilde{\Gamma}_N^\alpha V_\alpha}{\sum_\alpha \tilde{\Gamma}_N^\alpha}\right)\right] \\ &\approx \tilde{P}_{0,N}\left(V_L - \frac{\sum_\alpha \tilde{\Gamma}_N^\alpha V_\alpha}{\sum_\alpha \tilde{\Gamma}_N^\alpha}\right) \\ &\quad - \beta\tilde{P}_{0,N}\left(\frac{\sum_\alpha \tilde{\Gamma}_N^\alpha (V_\alpha - V_L)}{\sum_\alpha \tilde{\Gamma}_N^\alpha}\right) \\ &= -\beta\tilde{P}_{0,N}\left(\frac{\tilde{\Gamma}_N^R (V_R - V_L)}{\sum_\alpha \tilde{\Gamma}_N^\alpha}\right) \end{aligned} \tag{A.13}$$

Writing $V = V_R - V_L$, the conductance is written as

$$\begin{aligned} G = \frac{dI}{dV}|_{V=0} &= -\beta \sum_N \tilde{P}_{0,N} \frac{\tilde{\Gamma}_N^R \tilde{\Gamma}_N^L}{\tilde{\Gamma}_N^R + \tilde{\Gamma}_N^L} \\ &= -\beta \sum_N P_{0,N} \frac{\Gamma_N^R \Gamma_N^L}{\Gamma_N^R + \Gamma_N^L} \\ &= \sum_N \frac{\gamma_N^R \gamma_N^L}{\gamma_N^R + \gamma_N^L}, \end{aligned} \tag{A.14}$$

where $\gamma_N^\alpha = -\beta P_{0,N} \Gamma_N^\alpha$.

In the above expression, we use the equilibrium tunneling rate

$$\begin{aligned} \gamma_N^\alpha &= -\beta \tau_\alpha Z_{tot}^{-1} \sum_{i,j} e^{\beta N \mu} Z_N P_N(E_i) f(E_j - E_i - \mu) \left| \langle \psi_j | c_\alpha^\dagger | \psi_i \rangle \right|^2 \\ &= -\beta \tau_\alpha \sum_{i,j} P(E_i) f(E_j - E_i - \mu) \left| \langle \psi_j | c_\alpha^\dagger | \psi_i \rangle \right|^2 . \end{aligned} \tag{A.15}$$

Here we have used the identity we showed earlier, i.e.,

$$P(E_i) = P_N(E_i) P_{0,N} = P_N(E_i) Z_N \frac{e^{\beta N \mu}}{Z_{tot}} = \frac{e^{-\beta(E_i - N\mu)}}{Z_{tot}}. \tag{A.16}$$

Using the identity

$$\begin{aligned} e^{-\beta N \mu} P(E_i) f(E_j - E_i - \mu) &= \frac{e^{-\beta E_i}}{1 + e^{\beta(E_j - E_i - \mu)}} \\ &= \frac{1}{e^{\beta E_i} + e^{\beta(E_j - \mu)}} \\ &= -\beta^{-1} \left[e^{-\beta E_i} + e^{-\beta(E_j - \mu)} \right] f'(E_j - E_i - \mu) \\ &= -\beta^{-1} e^{-\beta N \mu} \left[P(E_i) + P(E_j) \right] f'(E_j - E_i - \mu), \end{aligned} \tag{A.17}$$

the above conductance can be written in the Meir-Wingreen form

$$\gamma_N^\alpha = \tau_\alpha \sum_{i,j} \left[P(E_i) + P(E_j)\right] f'(E_j - E_i - \mu) \left|\langle\psi_j|c_\alpha^\dagger|\psi_i\rangle\right|^2. \tag{A.18}$$

A.4 Meir-Wingreen Formula for One-terminal CB Majorana nanowire

The original Meir-Wingreen's formula is the Landauer formula, when we consider the transport through an interacting region, with one terminal connecting the system and the environment [126]. The general Hamiltonian is of this form

$$H = \sum_{k,\alpha\in L,R} \epsilon_{k\alpha} a_{k\alpha}^\dagger a_{k\alpha} + H_{int}(\{c_n^\dagger\};\{c_n\}) + \sum_{k,n,\alpha\in L,R} (V_{k\alpha,n} a_{k\alpha}^\dagger c_n + \text{H.c.}), \tag{A.19}$$

where $a_{k\alpha}^\dagger$ ($a_{k\alpha}$) creates (destroys) an electron with momentum k in channel α from either left (L) or the right (R) lead, and $\{c_n^\dagger\}$ and $\{c_n\}$ form a complete and orthonormal set of single-electron creation and annihilation operators in the interacting region. The channel index includes spin and all other quantum numbers which, in addition to k, are necessary to define uniquely a state in the leads.

Through the Keldysh formalism, one can get the linear-response conductance G in the form

$$G = \frac{e^2}{\hbar} \sum_{m,n} \Gamma_{n,m}(E_j - E_i) \sum_{i,j} (P_i + P_j) \left[-\frac{\partial f_{eq}(E_j - E_i)}{\partial\epsilon}\right] \langle\psi_j|c_n^\dagger|\psi_i\rangle\langle\psi_i|c_m|\psi_j\rangle, \tag{A.20}$$

where the ψ_i are eigenstates, with energies E_i, of the uncoupled interacting region, and P_i is the equilibrium probability of state ψ_i. For non-interacting electrons, one can choose the c's to correspond to single-particle eigenstates of the uncoupled system, and the overlap factor in each

term, $\langle\psi_j|c_n^\dagger|\psi_i\rangle\langle\psi_i|c_m|\psi_j\rangle$, is trivially 0 or 1.

Now we apply our system to the Meir-Wingreen's formula in Eq. (A.20). In our case, we consider only $m = n = \{L, R\} \otimes \{\uparrow, \downarrow\}$, where the transmission only occurs on the left and right ends of the nanowire, and the tunneling factor is independent of the energy (setting $\Gamma_{n,m} = 1$), then Eq. (A.20) becomes

$$G = \frac{e^2}{\hbar} \sum_{x=L,R} \sum_{\sigma=\uparrow,\downarrow} \sum_{i,j} (P_i + P_j) \left[-\frac{\partial f_{eq}(E_j - E_i)}{\partial \epsilon} \right] |\langle\psi_j|c_{x,\sigma}^\dagger|\psi_i\rangle|^2, \tag{A.21}$$

where $|\psi_i\rangle = |\{n_i\}\rangle$ is the state with some quasi-electron configuration over N_l energy levels, and

$$E_i = \sum_s n_s \epsilon_s + U(N) \tag{A.22}$$

is the energy of configuration $\{n_i\}$ with electrostatic energy $U(N) = E_c(N - n_g)^2$. n_s is the occupation number of s state of the quasiparticle, i.e., n_s is the eigenvalue of the operator $d_s^\dagger d_s$ while $d_s^\dagger$ and d_s are creation and annihilation operators for the quasi-particles. (Note that $N = \sum_s n_s + 2N_c$ is the total electron number and N_c is the additional number of the Cooper pairs away from the charge-neutral point as the gate voltage of the nanowire is zero, and n_g is the number of electrons corresponding to the gate voltage.) ϵ_s is the eigen-energy of s state of the Hamiltonian as Eq.(4.54). The probability for quasi-particle distribution configuration $\{n_i\}$ is described by the Gibbs distribution

$$P_i = e^{-\beta E_i}/Z = Z^{-1} \exp\left[-\beta \left(\sum_s n_s \epsilon_s + U(N) \right) \right], \tag{A.23}$$

where the canonical partition function is given by

$$Z = \sum_i e^{-\beta E_i} = \sum_i \exp\left[-\beta\left(\sum_s n_s\epsilon_s + U(N)\right)\right]. \tag{A.24}$$

Due to fermion parity conservation, we only need to separate the total electron number N into even and odd groups. The superconductor ground state favors the even number of electrons due to the condensate. If one more electron adds in the superconductor and overcomes the superconducting gap, then there will be one extra quasiparticle besides the condensate. Otherwise, the condensate ground state will remain and only allow $2e$ transport. Therefore, the behaviors of even parity and odd parity for this superconductor-induced nanowire are different. We only need to discuss the parity of the total electron number N, i.e., we discuss only the two values from (N mod 2). To simplify the formula later, we can rewrite Eqs. (A.23) and (A.24) as

$$P_i = Z^{-1}\exp\left[-\beta\left(\sum_s n_s\epsilon_s + \frac{1}{2}Q_i\cdot\Delta U\right)\right] \tag{A.25}$$

and

$$Z = \sum_i \exp\left[-\beta\left(\sum_s n_s\epsilon_s + \frac{1}{2}Q_i\cdot\Delta U\right)\right], \tag{A.26}$$

where $Q_i = Q_0\cdot(-1)^{\sum_s n_s}$ is the fermion parity (note that $Q_0 = \pm 1$ is the ground-state fermion parity, and the subscript i means the quasi-particle distribution configuration.), and $\Delta U = U(N) - U(N-1)$. The parity of N and $(N-1)$ is opposite. Therefore, we can shift $U(N)$ and $U(N-1)$ by the mean value $[U(N-1)+U(N)]/2$ and express them with the parity Q_i and the electrostatic energy difference ΔU. Equation (A.26) can be further simplified

as

$$
\begin{aligned}
Z &= \sum_{\{n_i\}} \exp\left[-\beta\left(\sum_s n_s\epsilon_s + \frac{1}{2}Q_i\Delta U\right)\right] \\
&= \sum_{Q}\sum_{\{n_i\}} \delta(Q-Q_i)\exp\left[-\beta\left(\sum_s n_s\epsilon_s + \frac{1}{2}Q\Delta U\right)\right] \\
&= \sum_{Q=\pm 1}\sum_{\{n_i\}} \frac{1}{2}\left[1+Q\cdot Q_0(-1)^{\sum_s n_s}\right]\exp\left[-\beta\left(\sum_s n_s\epsilon_s + \frac{1}{2}Q\Delta U\right)\right] \\
&= \sum_{Q=\pm 1} \frac{1}{2}\exp\left(-\frac{\beta Q\cdot\Delta U}{2}\right)\left[\prod_s\left(1+e^{-\beta\epsilon_s}\right) + Q\cdot Q_0\cdot\prod_s\left(1-e^{-\beta\epsilon_s}\right)\right] \\
&= \sum_{Q=\pm 1} \frac{1}{2}e^{-\beta(Q\cdot\Delta U/2)}\cdot\prod_s(1+e^{-\beta\epsilon_s})\left[1+Q\cdot Q_0\cdot\prod_s\tanh\left(\frac{\beta\epsilon_s}{2}\right)\right].
\end{aligned}
\tag{A.27}
$$

The energy of configuration $\{n_i\}$, i.e., E_i [the original definition is in Eq. (A.22)], can also be shifted and redefined as

$$
E_i = \sum_s n_s\epsilon_s + \frac{Q_i\Delta U}{2}. \tag{A.28}
$$

Since the electron operator is of the form as Eqs. (4.56) and (4.57), the quasi-particle creation and annihilation operators can only change the orbital occupation number by one, say in the pth orbital. Hence, the eligible final transition state can only be the same configuration with one orbital occupation changed, i.e.,

$$
|\psi_j\rangle = |\{n_{j\neq p}, \bar{n}_p\}\rangle = (1-n_p)(d_p^\dagger|\{n_i\}\rangle) + n_p(d_p|\{n_i\}\rangle), \tag{A.29}
$$

with $n_p = 1$ ($n_p = 0$) if the pth orbital is occupied (empty) in the configuration $\{n_i\}$. Then the

energy difference between these two states is

$$E_p = E_j - E_i = (1 - 2n_p)\epsilon_p - Q_i \Delta U. \tag{A.30}$$

The transition matrix element is therefore $\langle \psi_j | c^\dagger_{x\sigma} | \psi_i \rangle \equiv \langle \{n_j\} | c^\dagger_{x\sigma} | \{n_i\} \rangle = \langle \{n_{i \neq p}, \bar{n}_p\} | c^\dagger_{x\sigma} | \{n_i\} \rangle = \left((1 - n_p) \langle \{n_i\} | d_p + n_p \langle \{n_i\} | d^\dagger_p \right) c^\dagger_{x\sigma} | \{n_i\} \rangle$. With Eqs. (4.56) and (4.57),

$$\langle \psi_j | c^\dagger_{x\sigma} | \psi_i \rangle = (1 - n_p) u^*_{p,x\alpha} + n_p v_{p,x\alpha}. \tag{A.31}$$

Hence,

$$|\langle \psi_i | c^\dagger_{x\sigma} | \psi_j \rangle|^2 = (1 - n_p) \Gamma^{x,\sigma}_p + n_p \Lambda^{x,\sigma}_p, \tag{A.32}$$

where

$$A^{x,\sigma}_p = |u_{p,x\sigma}|^2 \tag{A.33}$$

is the tunneling rate for the electron to tunnel from the lead at x to the nanowire (same for the opposite direction), and

$$B^{x,\sigma}_p = |v_{p,x\sigma}|^2 \tag{A.34}$$

is the tunneling rate for the hole to tunnel from the lead at x to the nanowire (same for the opposite direction). Note that $A^x_p = \sum_{\sigma=\uparrow,\downarrow} A^{x,\sigma}_p$ and $B^x_p = \sum_{\sigma=\uparrow,\downarrow} B^{x,\sigma}_p$ as defined in Eqs. (4.35) and (4.36).

With the ingredients above, we can rewrite Eq. (A.21) as

$$
\begin{aligned}
G &= \frac{e^2}{\hbar} \sum_{x=L,R} \sum_{\sigma=\uparrow,\downarrow} \sum_i P_i \sum_p \left(1+\frac{P_j}{P_i}\right) \left[-\frac{\partial f_{eq}\left((1-2n_p)\epsilon_p - Q_i \Delta U\right)}{\partial \epsilon}\right] \cdot \left[(1-n_p)A_p^{x,\sigma} + n_p B_p^{x,\sigma}\right] \\
&= \frac{e^2}{\hbar} \sum_{x=L,R} \sum_i P_i \sum_p \left(1+\exp\left[-\beta\left((1-2n_p)\epsilon_p - Q_i\Delta U\right)\right]\right) \\
&\quad \times \left\{-f'_{eq}\left((1-2n_p)\epsilon_p - Q_i\Delta U\right)\right\} \left[(1-n_p)A_p^x + n_p B_p^x\right] \\
&= \frac{e^2}{\hbar} \sum_{x=L,R} \sum_p \sum_{n=0,1} \sum_{Q=-1,1} \underbrace{\left(Z^{-1} \cdot \sum_{\substack{i:n=n_p \\ Q=Q_0\cdot(-1)^{\sum n_s}}} \exp\left[-\beta\left(\sum_s n_s\epsilon_s + \frac{1}{2}Q\Delta U\right)\right]\right)}_{F_p(n,Q)} \\
&\quad \times \underbrace{\left(1+\exp\left[-\beta\left((1-2n)\epsilon_p - Q\Delta U\right)\right]\right) \cdot \left[-f'_{eq}\left((1-2n)\epsilon_p - Q\Delta U\right)\right]}_{=\beta\cdot f_{eq}((1-2n)\epsilon_p - Q\Delta U)} \cdot \left[(1-n)A_p^x + nB_p^x\right] \\
&= \beta\frac{e^2}{\hbar} \sum_{x=L,R} \sum_p \sum_{n=0,1} \sum_{Q=-1,1} \underbrace{f_{eq}((1-2n)\epsilon_p - Q\Delta U)\cdot F_p(n,Q)}_{\tilde{F}_p(n,Q)} \cdot \left[(1-n)A_p^x + nB_p^x\right].
\end{aligned}
\tag{A.35}
$$

$F_p(n,Q)$ sums over all the possible configurations, but with the constriction that $n = n_p$ and

$Q = Q_0(-1)^{\sum_s n_s}$ being selected properly, i.e.,

$$
\begin{aligned}
F_p(n,Q) &= Z^{-1}e^{-\beta Q\Delta U/2}\sum_{\{n_s\}}\delta(n-n_p)\delta\left(Q-Q_0(-1)^{\sum n_s}\right)\exp\left(-\beta\sum_s n_s\epsilon_s\right)\\
&= Z^{-1}e^{-\beta Q\Delta U/2}e^{-\beta n\epsilon_p}\sum_{\{n_{s\neq p}\}}\underbrace{\frac{1}{2}\left[1+QQ_0-1)^{\sum_{s\neq p}n_s}(-1)^{n_p}\right]}_{\star}\exp\left(-\beta\sum_{s\neq p}n_s\epsilon_s\right)\\
&= \frac{1}{2Z}e^{-\beta Q\Delta U/2}e^{-\beta n\epsilon_p}\left[\prod_{s\neq p}\left(1+e^{-\beta\epsilon_s}\right)+QQ_0(-1)^{n_p}\prod_{s\neq p}\left(1-e^{-\beta\epsilon_s}\right)\right]\\
&= \frac{1}{2Z}e^{-\beta(Q\Delta U/2+n\epsilon_p)}\left[\frac{\prod_s(1+e^{-\beta\epsilon_s})}{(1+e^{-\beta\epsilon_p})}+QQ_0(-1)^n\frac{\prod_s(1-e^{-\beta\epsilon_s})}{(1-e^{-\beta\epsilon_p})}\right]\\
&= \frac{1}{2Z}e^{-\beta(Q\Delta U/2+n\epsilon_p)}\prod_s(1+e^{-\beta\epsilon_s})\left[\frac{1}{1+e^{-\beta\epsilon_p}}+QQ_0(-1)^n\frac{\prod_s\tanh\left(\beta\epsilon_s/2\right)}{1-e^{-\beta\epsilon_p}}\right]\\
&= \frac{e^{-\beta(Q\Delta U/2+n\epsilon_p)}\left[\frac{1}{(1+e^{-\beta\epsilon_p})}+QQ_0(-1)^n\frac{\prod_s\tanh(\beta\epsilon_s/2)}{(1-e^{-\beta\epsilon_p})}\right]}{\sum_{Q=\pm1}e^{-\beta(Q\Delta U/2)}\left[1+QQ_0\prod_s\tanh\left(\frac{\beta\epsilon_s}{2}\right)\right]}
\end{aligned}
\tag{A.36}
$$

Note that the star $\star$ part in Eq. (A.36) is technically a delta function for Q when we sum over (-1) and 1.

$$
f \equiv \frac{1}{2}\left[1+QQ_0(-1)^{\sum_{s\neq p}n_s}(-1)^{n_p}\right]. \tag{A.37}
$$

If Q is the correct parity, i.e.,

$$
Q = Q_0(-1)^{\sum_s n_s} = Q_0(-1)^{\sum_{s\neq p}n_s}(-1)^{n_p}, \tag{A.38}
$$

then $f = (1+1)/2 = 1$. On the contrary, if $Q = -Q_0(-1)^{\sum_s n_s}$ (not correct parity), then $f = (1-1) = 0$. So only Q that represents the correct fermion parity is picked and evaluated.

We can actually simplify Eq. (A.36) further.

$$\begin{aligned}
\frac{\prod_s \tanh\left(\frac{\beta\epsilon_s}{2}\right)}{1-e^{-\beta\epsilon_p}} &= \frac{\tanh\left(\beta\epsilon_p/2\right)}{e^{-\beta\epsilon_p/2}\left(e^{\beta\epsilon_p/2}-e^{-\beta\epsilon_p/2}\right)}\prod_{s\neq p}\tanh\left(\frac{\beta\epsilon_s}{2}\right) \\
&= e^{\beta\epsilon_p/2}\frac{\tanh\left(\beta\epsilon_p/2\right)}{2\sinh\left(\beta\epsilon_p/2\right)}\prod_{s\neq p}\tanh\left(\frac{\beta\epsilon_s}{2}\right) \\
&= \frac{e^{\beta\epsilon_p/2}}{2\cosh\left(\beta\epsilon_p/2\right)}\prod_{s\neq p}\tanh\left(\frac{\beta\epsilon_s}{2}\right) \\
&= \frac{e^{\beta\epsilon_p/2}}{e^{\beta\epsilon_p/2}+e^{-\beta\epsilon_p/2}}\prod_{s\neq p}\tanh\left(\frac{\beta\epsilon_s}{2}\right) \\
&= \frac{1}{1+e^{-\beta\epsilon_p}}\prod_{s\neq p}\tanh\left(\frac{\beta\epsilon_s}{2}\right)
\end{aligned} \tag{A.39}$$

Then, the $F_p(n,Q)$ factor is simplified to be

$$\begin{aligned}
F_p(n,Q) &= \frac{e^{-\beta(Q\Delta U/2+n\epsilon_p)}\left[\frac{1}{(1+e^{-\beta\epsilon_p})}+QQ_0(-1)^n\frac{1}{(1+e^{-\beta\epsilon_p})}\prod_{s\neq p}\tanh\left(\frac{\beta\epsilon_s}{2}\right)\right]}{\sum_{Q=\pm1}e^{-\beta(Q\Delta U/2)}\left[1+QQ_0\prod_s\tanh\left(\frac{\beta\epsilon_s}{2}\right)\right]} \\
&= \frac{\frac{e^{-\beta(Q\Delta U/2+n\epsilon_p)}}{(1+e^{-\beta\epsilon_p})}\left[1+QQ_0(-1)^n\prod_{s\neq p}\tanh\left(\frac{\beta\epsilon_s}{2}\right)\right]}{\sum_{Q=\pm1}e^{-\beta(Q\Delta U/2)}\left[1+QQ_0\prod_s\tanh\left(\frac{\beta\epsilon_s}{2}\right)\right]} \\
&= \frac{e^{-\beta(Q\Delta U/2+n\epsilon_p)}\left[1+QQ_0-1)^n\prod_{s\neq p}\tanh\left(\frac{\beta\epsilon_s}{2}\right)\right]}{\sum_{Q=\pm1}\sum_{n=0,1}e^{-\beta(Q\Delta U/2+n\epsilon_p)}\left[1+QQ_0\prod_s\tanh\left(\frac{\beta\epsilon_s}{2}\right)\right]}.
\end{aligned} \tag{A.40}$$

For numerical evaluation [in MATLAB, $\tanh(x)$ gives 1, when x is above some threshold, and this causes the conductance computation unable], it is necessary to replace $\prod_s \tanh(\beta\epsilon_s/2)$ with $(1-e^{-y})$, where

$$y = -\log\left(1-\prod_s\tanh(\frac{\beta\epsilon_s}{2})\right) \tag{A.41}$$

is evaluated by the identity

$$\tanh(x) = 1 - 2e^{-\left[2x+\log(1+e^{-2x})\right]}. \tag{A.42}$$

Bibliography

[1] Majorana, E. (1937) Il Nuovo Cimento, 5, 171-184. - References - Scientific Research Publishing. https://www.scirp.org/(S(lz5mqp453edsnp55rrgjct55.))/reference/referencespapers.aspx?referenceid=2196980.

[2] A. Yu Kitaev. Unpaired Majorana fermions in quantum wires. *Phys.-Usp.*, 44(10S):131, 2001. http://stacks.iop.org/1063-7869/44/i=10S/a=S29.

[3] A. Yu. Kitaev. Fault-tolerant quantum computation by anyons. *Annals of Physics*, 303(1):2–30, January 2003. https://www.sciencedirect.com/science/article/pii/S0003491602000180.

[4] Michael Freedman, Alexei Kitaev, Michael Larsen, and Zhenghan Wang. Topological quantum computation. *Bull. Amer. Math. Soc.*, 40(1):31–38, 2003. https://www.ams.org/bull/2003-40-01/S0273-0979-02-00964-3/.

[5] Sankar Das Sarma, Michael Freedman, and Chetan Nayak. Topologically Protected Qubits from a Possible Non-Abelian Fractional Quantum Hall State. *Phys. Rev. Lett.*, 94(16):166802, April 2005. https://link.aps.org/doi/10.1103/PhysRevLett.94.166802.

[6] Chetan Nayak, Steven H. Simon, Ady Stern, Michael Freedman, and Sankar Das Sarma. Non-Abelian anyons and topological quantum computation. *Rev. Mod. Phys.*, 80(3):1083–1159, September 2008. https://link.aps.org/doi/10.1103/RevModPhys.80.1083.

[7] Parsa Bonderson, Michael Freedman, and Chetan Nayak. Measurement-Only Topological Quantum Computation. *Phys. Rev. Lett.*, 101(1):010501, June 2008. https://link.aps.org/doi/10.1103/PhysRevLett.101.010501.

[8] Parsa Bonderson, Michael Freedman, and Chetan Nayak. Measurement-only topological quantum computation via anyonic interferometry. *Annals of Physics*, 324(4):787–826, April 2009. https://www.sciencedirect.com/science/article/pii/S0003491608001577.

[9] Jay D. Sau, Sumanta Tewari, and S. Das Sarma. Universal quantum computation in a semiconductor quantum wire network. *Phys. Rev. A*, 82(5):052322, November 2010. https://link.aps.org/doi/10.1103/PhysRevA.82.052322.

[10] L. Mazza, M. Rizzi, M. D. Lukin, and J. I. Cirac. Robustness of quantum memories based on Majorana zero modes. *Phys. Rev. B*, 88(20):205142, November 2013. https://link.aps.org/doi/10.1103/PhysRevB.88.205142.

[11] T. Hyart, B. van Heck, I. C. Fulga, M. Burrello, A. R. Akhmerov, and C. W. J. Beenakker. Flux-controlled quantum computation with Majorana fermions. *Phys. Rev. B*, 88(3):035121, July 2013. https://link.aps.org/doi/10.1103/PhysRevB.88.035121.

[12] Parsa Bonderson. Measurement-only topological quantum computation via tunable interactions. *Phys. Rev. B*, 87(3):035113, January 2013. https://link.aps.org/doi/10.1103/PhysRevB.87.035113.

[13] David Aasen, Michael Hell, Ryan V. Mishmash, Andrew Higginbotham, Jeroen Danon, Martin Leijnse, Thomas S. Jespersen, Joshua A. Folk, Charles M. Marcus, Karsten Flensberg, and Jason Alicea. Milestones Toward Majorana-Based Quantum Computing. *Phys. Rev. X*, 6(3):031016, August 2016. https://link.aps.org/doi/10.1103/PhysRevX.6.031016.

[14] David J. Clarke, Jay D. Sau, and Sankar Das Sarma. A Practical Phase Gate for Producing Bell Violations in Majorana Wires. *Phys. Rev. X*, 6(2):021005, April 2016. https://link.aps.org/doi/10.1103/PhysRevX.6.021005.

[15] Matteo Ippoliti, Matteo Rizzi, Vittorio Giovannetti, and Leonardo Mazza. Quantum memories with zero-energy Majorana modes and experimental constraints. *Phys. Rev. A*, 93(6):062325, June 2016. https://link.aps.org/doi/10.1103/PhysRevA.93.062325.

[16] Grigory E. Volovik. *The Universe in a Helium Droplet*. International Series of Monographs on Physics. Oxford University Press, Oxford, 2009. https://oxford.universitypressscholarship.com/10.1093/acprof:oso/9780199564842.001.0001/acprof-9780199564842.

[17] Eduardo Fradkin, Chetan Nayak, Alexei Tsvelik, and Frank Wilczek. A Chern-Simons effective field theory for the Pfaffian quantum Hall state. *Nuclear Physics B*, 516(3):704–718, April 1998. https://www.sciencedirect.com/science/article/pii/S0550321398001114.

[18] R. H. Morf. Transition from Quantum Hall to Compressible States in the Second Landau Level: New Light on the $\ensuremath{\nu}\phantom{\rule{0ex}{0ex}}=\phantom{\rule{0ex}{0ex}}5/2$ Enigma. *Phys. Rev. Lett.*, 80(7):1505–1508, February 1998. https://link.aps.org/doi/10.1103/PhysRevLett.80.1505.

[19] N. Read and Dmitry Green. Paired states of fermions in two dimensions with breaking of parity and time-reversal symmetries and the fractional quantum Hall effect. *Phys. Rev. B*, 61(15):10267–10297, April 2000. https://link.aps.org/doi/10.1103/PhysRevB.61.10267.

[20] N. B. Kopnin and M. M. Salomaa. Mutual friction in superfluid ${\hat{3}}\mathrm{He}$: Effects of bound states in the vortex core. *Phys. Rev. B*, 44(17):9667–9677, November 1991. https://link.aps.org/doi/10.1103/PhysRevB.44.9667.

[21] G. E. Volovik. Fermion zero modes on vortices in chiral superconductors. *Jetp Lett.*, 70(9):609–614, November 1999. https://doi.org/10.1134/1.568223.

[22] T. Senthil and Matthew P. A. Fisher. Quasiparticle localization in superconductors with spin-orbit scattering. *Phys. Rev. B*, 61(14):9690–9698, April 2000. https://link.aps.org/doi/10.1103/PhysRevB.61.9690.

[23] D. A. Ivanov. Non-Abelian Statistics of Half-Quantum Vortices in p-Wave Superconductors. *Phys. Rev. Lett.*, 86(2):268–271, January 2001. https://link.aps.org/doi/10.1103/PhysRevLett.86.268.

[24] Sankar Das Sarma, Chetan Nayak, and Sumanta Tewari. Proposal to stabilize and detect half-quantum vortices in strontium ruthenate thin films: Non-Abelian braiding statistics of vortices in a ${p}_{x}+i{p}_{y}$ superconductor. *Phys. Rev. B*, 73(22):220502, June 2006. https://link.aps.org/doi/10.1103/PhysRevB.73.220502.

[25] Liang Fu and C. L. Kane. Superconducting Proximity Effect and Majorana Fermions at the Surface of a Topological Insulator. *Phys. Rev. Lett.*, 100(9):096407, March 2008. https://link.aps.org/doi/10.1103/PhysRevLett.100.096407.

[26] Jay D. Sau, Roman M. Lutchyn, Sumanta Tewari, and S. Das Sarma. Generic New Platform for Topological Quantum Computation Using Semiconductor Heterostructures. *Phys. Rev. Lett.*, 104(4):040502, January 2010. https://link.aps.org/doi/10.1103/PhysRevLett.104.040502.

[27] Jay D. Sau, Sumanta Tewari, Roman M. Lutchyn, Tudor D. Stanescu, and S. Das Sarma. Non-Abelian quantum order in spin-orbit-coupled semiconductors: Search for topological Majorana particles in solid-state systems. *Phys. Rev. B*, 82(21):214509, December 2010. https://link.aps.org/doi/10.1103/PhysRevB.82.214509.

[28] Roman M. Lutchyn, Jay D. Sau, and S. Das Sarma. Majorana Fermions and a Topological Phase Transition in Semiconductor-Superconductor Heterostructures. *Phys. Rev. Lett.*, 105(7):077001, August 2010. https://link.aps.org/doi/10.1103/PhysRevLett.105.077001.

[29] Yuval Oreg, Gil Refael, and Felix von Oppen. Helical Liquids and Majorana Bound States in Quantum Wires. *Phys. Rev. Lett.*, 105(17):177002, October 2010. https://link.aps.org/doi/10.1103/PhysRevLett.105.177002.

[30] Jason Alicea. Majorana fermions in a tunable semiconductor device. *Phys. Rev. B*, 81(12):125318, March 2010. https://link.aps.org/doi/10.1103/PhysRevB.81.125318.

[31] V. Mourik, K. Zuo, S. M. Frolov, S. R. Plissard, E. P. a. M. Bakkers, and L. P. Kouwenhoven. Signatures of Majorana Fermions in Hybrid Superconductor-Semiconductor Nanowire Devices. *Science*, 336(6084):1003–1007, May 2012. http://science.sciencemag.org/content/336/6084/1003.

[32] M. T. Deng, C. L. Yu, G. Y. Huang, M. Larsson, P. Caroff, and H. Q. Xu. Anomalous Zero-Bias Conductance Peak in a Nb–InSb Nanowire–Nb Hybrid Device. *Nano Lett.*, 12(12):6414–6419, December 2012. https://doi.org/10.1021/nl303758w.

[33] Anindya Das, Yuval Ronen, Yonatan Most, Yuval Oreg, Moty Heiblum, and Hadas Shtrikman. Zero-bias peaks and splitting in an Al–InAs nanowire topological superconductor as a signature of Majorana fermions. *Nature Physics*, 8(12):887–895, December 2012. https://www.nature.com/articles/nphys2479.

[34] H. O. H. Churchill, V. Fatemi, K. Grove-Rasmussen, M. T. Deng, P. Caroff, H. Q. Xu, and C. M. Marcus. Superconductor-nanowire devices from tunneling to the multichannel regime: Zero-bias oscillations and magnetoconductance crossover. *Phys. Rev. B*, 87(24):241401, June 2013. https://link.aps.org/doi/10.1103/PhysRevB.87.241401.

[35] A. D. K. Finck, D. J. Van Harlingen, P. K. Mohseni, K. Jung, and X. Li. Anomalous Modulation of a Zero-Bias Peak in a Hybrid Nanowire-Superconductor Device. *Phys. Rev. Lett.*, 110(12):126406, March 2013. https://link.aps.org/doi/10.1103/PhysRevLett.110.126406.

[36] M. T. Deng, S. Vaitiekėnas, E. B. Hansen, J. Danon, M. Leijnse, K. Flensberg, J. Nygård, P. Krogstrup, and C. M. Marcus. Majorana bound state in a coupled quantum-dot hybrid-nanowire system. *Science*, 354(6319):1557–1562, December 2016. http://science.sciencemag.org/content/354/6319/1557.

[37] Jun Chen, Peng Yu, John Stenger, Moïra Hocevar, Diana Car, Sébastien R. Plissard, Erik P. A. M. Bakkers, Tudor D. Stanescu, and Sergey M. Frolov. Experimental phase diagram of zero-bias conductance peaks in superconductor/semiconductor nanowire devices. *Science Advances*, 3(9):e1701476, September 2017. http://advances.sciencemag.org/content/3/9/e1701476.

[38] Fabrizio Nichele, Asbjørn C. C. Drachmann, Alexander M. Whiticar, Eoin C. T. O'Farrell, Henri J. Suominen, Antonio Fornieri, Tian Wang, Geoffrey C. Gardner, Candice Thomas, Anthony T. Hatke, Peter Krogstrup, Michael J. Manfra, Karsten Flensberg, and Charles M. Marcus. Scaling of Majorana Zero-Bias Conductance Peaks. *Phys. Rev. Lett.*, 119(13):136803, September 2017. https://link.aps.org/doi/10.1103/PhysRevLett.119.136803.

[39] Hao Zhang, Önder Gül, Sonia Conesa-Boj, Michał P. Nowak, Michael Wimmer, Kun Zuo, Vincent Mourik, Folkert K. de Vries, Jasper van Veen, Michiel W. A. de Moor, Jouri D. S. Bommer, David J. van Woerkom, Diana Car, Sébastien R. Plissard, Erik P. A. M. Bakkers, Marina Quintero-Pérez, Maja C. Cassidy, Sebastian Koelling, Srijit Goswami,

Kenji Watanabe, Takashi Taniguchi, and Leo P. Kouwenhoven. Ballistic superconductivity in semiconductor nanowires. *Nature Communications*, 8:16025, July 2017. https://www.nature.com/articles/ncomms16025.

[40] J. Kammhuber, M. C. Cassidy, F. Pei, M. P. Nowak, A. Vuik, Ö Gül, D. Car, S. R. Plissard, E. P. a. M. Bakkers, M. Wimmer, and L. P. Kouwenhoven. Conductance through a helical state in an Indium antimonide nanowire. *Nat Commun*, 8(1):478, September 2017. http://www.nature.com/articles/s41467-017-00315-y.

[41] S. Vaitiekėnas, M.-T. Deng, J. Nygård, P. Krogstrup, and C. M. Marcus. Effective g Factor of Subgap States in Hybrid Nanowires. *Phys. Rev. Lett.*, 121(3):037703, July 2018. https://link.aps.org/doi/10.1103/PhysRevLett.121.037703.

[42] Michiel W. A. de Moor, Jouri D. S. Bommer, Di Xu, Georg W. Winkler, Andrey E. Antipov, Arno Bargerbos, Guanzhong Wang, Nick van Loo, Roy L. M. Op het Veld, Sasa Gazibegovic, Diana Car, John A. Logan, Mihir Pendharkar, Joon Sue Lee, Erik P. A. M. Bakkers, Chris J. Palmstrøm, Roman M. Lutchyn, Leo P. Kouwenhoven, and Hao Zhang. Electric field tunable superconductor-semiconductor coupling in Majorana nanowires. *New J. Phys.*, 20(10):103049, October 2018. https://doi.org/10.1088/1367-2630/aae61d.

[43] Önder Gül, Hao Zhang, Jouri D. S. Bommer, Michiel W. A. de Moor, Diana Car, Sébastien R. Plissard, Erik P. A. M. Bakkers, Attila Geresdi, Kenji Watanabe, Takashi Taniguchi, and Leo P. Kouwenhoven. Ballistic Majorana nanowire devices. *Nature Nanotechnology*, 13(3):192, March 2018. https://www.nature.com/articles/s41565-017-0032-8.

[44] Hao Zhang, Chun-Xiao Liu, Sasa Gazibegovic, Di Xu, John A. Logan, Guanzhong Wang, Nick van Loo, Jouri D. S. Bommer, Michiel W. A. de Moor, Diana Car, Roy L. M. Op het Veld, Petrus J. van Veldhoven, Sebastian Koelling, Marcel A. Verheijen, Mihir Pendharkar, Daniel J. Pennachio, Borzoyeh Shojaei, Joon Sue Lee, Chris J. Palmstrøm, Erik P. A. M. Bakkers, S. Das Sarma, and Leo P. Kouwenhoven. Quantized Majorana conductance. *Nature*, 556(7699):74–79, April 2018. https://www.nature.com/articles/nature26142.

[45] Jouri D. S. Bommer, Hao Zhang, Önder Gül, Bas Nijholt, Michael Wimmer, Filipp N. Rybakov, Julien Garaud, Donjan Rodic, Egor Babaev, Matthias Troyer, Diana Car, Sébastien R. Plissard, Erik P. A. M. Bakkers, Kenji Watanabe, Takashi Taniguchi, and Leo P. Kouwenhoven. Spin-Orbit Protection of Induced Superconductivity in Majorana Nanowires. *Phys. Rev. Lett.*, 122(18):187702, May 2019. https://link.aps.org/doi/10.1103/PhysRevLett.122.187702.

[46] Anna Grivnin, Ella Bor, Moty Heiblum, Yuval Oreg, and Hadas Shtrikman. Concomitant opening of a bulk-gap with an emerging possible Majorana zero mode. *Nature Communications*, 10(1):1940, April 2019. https://www.nature.com/articles/s41467-019-09771-0.

[47] J. Chen, B. D. Woods, P. Yu, M. Hocevar, D. Car, S. R. Plissard, E. P. A. M. Bakkers, T. D. Stanescu, and S. M. Frolov. Ubiquitous Non-Majorana Zero-Bias Conductance Peaks in Nanowire Devices. *Phys. Rev. Lett.*, 123(10):107703, September 2019. https://link.aps.org/doi/10.1103/PhysRevLett.123.107703.

[48] G. L. R. Anselmetti, E. A. Martinez, G. C. Ménard, D. Puglia, F. K. Malinowski, J. S. Lee, S. Choi, M. Pendharkar, C. J. Palmstrøm, C. M. Marcus, L. Casparis, and A. P. Higginbotham. End-to-end correlated subgap states in hybrid nanowires. *Phys. Rev. B*, 100(20):205412, November 2019. https://link.aps.org/doi/10.1103/PhysRevB.100.205412.

[49] G. C. Ménard, G. L. R. Anselmetti, E. A. Martinez, D. Puglia, F. K. Malinowski, J. S. Lee, S. Choi, M. Pendharkar, C. J. Palmstrøm, K. Flensberg, C. M. Marcus, L. Casparis, and A. P. Higginbotham. Conductance-Matrix Symmetries of a Three-Terminal Hybrid Device. *Phys. Rev. Lett.*, 124(3):036802, January 2020. https://link.aps.org/doi/10.1103/PhysRevLett.124.036802.

[50] D. Puglia, E. A. Martinez, G. C. Ménard, A. Pöschl, S. Gronin, G. C. Gardner, R. Kallaher, M. J. Manfra, C. M. Marcus, A. P. Higginbotham, and L. Casparis. Closing of the induced gap in a hybrid superconductor-semiconductor nanowire. *Phys. Rev. B*, 103(23):235201, June 2021. https://link.aps.org/doi/10.1103/PhysRevB.103.235201.

[51] P. Yu, J. Chen, M. Gomanko, G. Badawy, E. P. a. M. Bakkers, K. Zuo, V. Mourik, and S. M. Frolov. Non-Majorana states yield nearly quantized conductance in proximatized nanowires. *Nat. Phys.*, 17(4):482–488, April 2021. https://www.nature.com/articles/s41567-020-01107-w.

[52] Hao Zhang, Michiel W. A. de Moor, Jouri D. S. Bommer, Di Xu, Guanzhong Wang, Nick van Loo, Chun-Xiao Liu, Sasa Gazibegovic, John A. Logan, Diana Car, Roy L. M. Op het Veld, Petrus J. van Veldhoven, Sebastian Koelling, Marcel A. Verheijen, Mihir Pendharkar, Daniel J. Pennachio, Borzoyeh Shojaei, Joon Sue Lee, Chris J. Palmstrøm, Erik P. A. M. Bakkers, S. Das Sarma, and Leo P. Kouwenhoven. Large zero-bias peaks in InSb-Al hybrid semiconductor-superconductor nanowire devices. *arXiv:2101.11456 [cond-mat]*, January 2021. http://arxiv.org/abs/2101.11456.

[53] K. Sengupta, Igor Žutić, Hyok-Jon Kwon, Victor M. Yakovenko, and S. Das Sarma. Midgap edge states and pairing symmetry of quasi-one-dimensional organic superconductors. *Phys. Rev. B*, 63(14):144531, March 2001. https://link.aps.org/doi/10.1103/PhysRevB.63.144531.

[54] K. T. Law, Patrick A. Lee, and T. K. Ng. Majorana Fermion Induced Resonant Andreev Reflection. *Phys. Rev. Lett.*, 103(23):237001, December 2009. https://link.aps.org/doi/10.1103/PhysRevLett.103.237001.

[55] Karsten Flensberg. Tunneling characteristics of a chain of Majorana bound states. *Phys. Rev. B*, 82(18):180516, November 2010. https://link.aps.org/doi/10.1103/PhysRevB.82.180516.

[56] M. Wimmer, A. R. Akhmerov, J. P. Dahlhaus, and C. W. J. Beenakker. Quantum point contact as a probe of a topological superconductor. *New J. Phys.*, 13(5):053016, May 2011. https://doi.org/10.1088/1367-2630/13/5/053016.

[57] F. Setiawan, P. M. R. Brydon, Jay D. Sau, and S. Das Sarma. Conductance spectroscopy of topological superconductor wire junctions. *Phys. Rev. B*, 91(21):214513, June 2015. https://link.aps.org/doi/10.1103/PhysRevB.91.214513.

[58] Haining Pan and S. Das Sarma. Physical mechanisms for zero-bias conductance peaks in Majorana nanowires. *Phys. Rev. Research*, 2(1):013377, March 2020. https://link.aps.org/doi/10.1103/PhysRevResearch.2.013377.

[59] G. Kells, D. Meidan, and P. W. Brouwer. Near-zero-energy end states in topologically trivial spin-orbit coupled superconducting nanowires with a smooth confinement. *Phys. Rev. B*, 86(10):100503, September 2012. https://link.aps.org/doi/10.1103/PhysRevB.86.100503.

[60] Jie Liu, Andrew C. Potter, K. T. Law, and Patrick A. Lee. Zero-Bias Peaks in the Tunneling Conductance of Spin-Orbit-Coupled Superconducting Wires with and without Majorana End-States. *Phys. Rev. Lett.*, 109(26):267002, December 2012. https://link.aps.org/doi/10.1103/PhysRevLett.109.267002.

[61] Elsa Prada, Pablo San-Jose, and Ramón Aguado. Transport spectroscopy of NS nanowire junctions with Majorana fermions. *Phys. Rev. B*, 86(18):180503, November 2012. https://link.aps.org/doi/10.1103/PhysRevB.86.180503.

[62] Chun-Xiao Liu, Jay D. Sau, Tudor D. Stanescu, and S. Das Sarma. Andreev bound states versus Majorana bound states in quantum dot-nanowire-superconductor hybrid structures: Trivial versus topological zero-bias conductance peaks. *Phys. Rev. B*, 96(7):075161, August 2017. https://link.aps.org/doi/10.1103/PhysRevB.96.075161.

[63] Christopher Moore, Chuanchang Zeng, Tudor D. Stanescu, and Sumanta Tewari. Quantized zero-bias conductance plateau in semiconductor-superconductor heterostructures without topological Majorana zero modes. *Phys. Rev. B*, 98(15):155314, October 2018. https://link.aps.org/doi/10.1103/PhysRevB.98.155314.

[64] Christopher Moore, Tudor D. Stanescu, and Sumanta Tewari. Two-terminal charge tunneling: Disentangling Majorana zero modes from partially separated Andreev bound states in semiconductor-superconductor heterostructures. *Phys. Rev. B*, 97(16):165302, April 2018. https://link.aps.org/doi/10.1103/PhysRevB.97.165302.

[65] Adriaan Vuik, Bas Nijholt, Anton Akhmerov, and Michael Wimmer. Reproducing topological properties with quasi-Majorana states. *SciPost Physics*, 7(5):061, November 2019. https://scipost.org/SciPostPhys.7.5.061.

[66] Dmitry Bagrets and Alexander Altland. Class D Spectral Peak in Majorana Quantum Wires. *Phys. Rev. Lett.*, 109(22):227005, November 2012. https://link.aps.org/doi/10.1103/PhysRevLett.109.227005.

[67] D. I. Pikulin, J. P. Dahlhaus, M. Wimmer, H. Schomerus, and C. W. J. Beenakker. A zero-voltage conductance peak from weak antilocalization in a Majorana nanowire. *New J. Phys.*, 14(12):125011, 2012. http://stacks.iop.org/1367-2630/14/i=12/a=125011.

[68] Jay D. Sau and S. Das Sarma. Density of states of disordered topological superconductor-semiconductor hybrid nanowires. *Phys. Rev. B*, 88(6):064506, August 2013. https://link.aps.org/doi/10.1103/PhysRevB.88.064506.

[69] Shuo Mi, D. I. Pikulin, M. Marciani, and C. W. J. Beenakker. X-shaped and Y-shaped Andreev resonance profiles in a superconducting quantum dot. *J. Exp. Theor. Phys.*, 119(6):1018–1027, December 2014. https://doi.org/10.1134/S1063776114120176.

[70] Frank Wilczek. Majorana returns. *Nature Phys*, 5(9):614–618, September 2009. http://www.nature.com/articles/nphys1380.

[71] T.-P. Choy, J. M. Edge, A. R. Akhmerov, and C. W. J. Beenakker. Majorana fermions emerging from magnetic nanoparticles on a superconductor without spin-orbit coupling. *Phys. Rev. B*, 84(19):195442, November 2011. https://link.aps.org/doi/10.1103/PhysRevB.84.195442.

[72] Mathias Duckheim and Piet W. Brouwer. Andreev reflection from noncentrosymmetric superconductors and Majorana bound-state generation in half-metallic ferromagnets. *Phys. Rev. B*, 83(5):054513, February 2011. https://link.aps.org/doi/10.1103/PhysRevB.83.054513.

[73] S. Nadj-Perge, I. K. Drozdov, B. A. Bernevig, and Ali Yazdani. Proposal for realizing Majorana fermions in chains of magnetic atoms on a superconductor. *Phys. Rev. B*, 88(2):020407, July 2013. https://link.aps.org/doi/10.1103/PhysRevB.88.020407.

[74] Suk Bum Chung, Hai-Jun Zhang, Xiao-Liang Qi, and Shou-Cheng Zhang. Topological superconducting phase and Majorana fermions in half-metal/superconductor heterostructures. *Phys. Rev. B*, 84(6):060510, August 2011. https://link.aps.org/doi/10.1103/PhysRevB.84.060510.

[75] Li Mao, Ming Gong, E. Dumitrescu, Sumanta Tewari, and Chuanwei Zhang. Hole-Doped Semiconductor Nanowire on Top of an s-Wave Superconductor: A New and Experimentally Accessible System for Majorana Fermions. *Phys. Rev. Lett.*, 108(17):177001, April 2012. https://link.aps.org/doi/10.1103/PhysRevLett.108.177001.

[76] Jay D. Sau and S. Das Sarma. Realizing a robust practical Majorana chain in a quantum-dot-superconductor linear array. *Nat Commun*, 3(1):964, July 2012. http://www.nature.com/articles/ncomms1966.

[77] Younghyun Kim, Meng Cheng, Bela Bauer, Roman M. Lutchyn, and S. Das Sarma. Helical order in one-dimensional magnetic atom chains and possible emergence of Majorana

bound states. *Phys. Rev. B*, 90(6):060401, August 2014. https://link.aps.org/doi/10.1103/PhysRevB.90.060401.

[78] P. M. R. Brydon, S. Das Sarma, Hoi-Yin Hui, and Jay D. Sau. Topological Yu-Shiba-Rusinov chain from spin-orbit coupling. *Phys. Rev. B*, 91(6):064505, February 2015. https://link.aps.org/doi/10.1103/PhysRevB.91.064505.

[79] Hoi-Yin Hui, P. M. R. Brydon, Jay D. Sau, S. Tewari, and S. Das Sarma. Majorana fermions in ferromagnetic chains on the surface of bulk spin-orbit coupled s-wave superconductors. *Sci Rep*, 5(1):8880, March 2015. http://www.nature.com/articles/srep08880.

[80] Martin Leijnse and Karsten Flensberg. Introduction to topological superconductivity and Majorana fermions. *Semicond. Sci. Technol.*, 27(12):124003, November 2012. https://doi.org/10.1088/0268-1242/27/12/124003.

[81] S. Das Sarma, Jay D. Sau, and Tudor D. Stanescu. Splitting of the zero-bias conductance peak as smoking gun evidence for the existence of the Majorana mode in a superconductor-semiconductor nanowire. *Phys. Rev. B*, 86(22):220506, December 2012. https://link.aps.org/doi/10.1103/PhysRevB.86.220506.

[82] T. Ö. Rosdahl, A. Vuik, M. Kjaergaard, and A. R. Akhmerov. Andreev rectifier: A nonlocal conductance signature of topological phase transitions. *Phys. Rev. B*, 97(4):045421, January 2018. https://link.aps.org/doi/10.1103/PhysRevB.97.045421.

[83] Yi-Hua Lai, Jay D. Sau, and Sankar Das Sarma. Presence versus absence of end-to-end nonlocal conductance correlations in Majorana nanowires: Majorana bound states versus Andreev bound states. *Phys. Rev. B*, 100(4):045302, July 2019. https://link.aps.org/doi/10.1103/PhysRevB.100.045302.

[84] Tudor D. Stanescu, Sumanta Tewari, Jay D. Sau, and S. Das Sarma. To Close or Not to Close: The Fate of the Superconducting Gap Across the Topological Quantum Phase Transition in Majorana-Carrying Semiconductor Nanowires. *Phys. Rev. Lett.*, 109(26):266402, December 2012. https://link.aps.org/doi/10.1103/PhysRevLett.109.266402.

[85] Yingyi Huang, Haining Pan, Chun-Xiao Liu, Jay D. Sau, Tudor D. Stanescu, and S. Das Sarma. Metamorphosis of Andreev bound states into Majorana bound states in pristine nanowires. *Phys. Rev. B*, 98(14):144511, October 2018. https://link.aps.org/doi/10.1103/PhysRevB.98.144511.

[86] Haining Pan, Chun-Xiao Liu, Michael Wimmer, and Sankar Das Sarma. Quantized and unquantized zero-bias tunneling conductance peaks in Majorana nanowires: Conductance below and above \$2{e}{\hat{2}}/h\$. *Phys. Rev. B*, 103(21):214502, June 2021. https://link.aps.org/doi/10.1103/PhysRevB.103.214502.

[87] Haining Pan, Jay D. Sau, and S. Das Sarma. Three-terminal nonlocal conductance in Majorana nanowires: Distinguishing topological and trivial in realistic systems with

disorder and inhomogeneous potential. *Phys. Rev. B*, 103(1):014513, January 2021. https://link.aps.org/doi/10.1103/PhysRevB.103.014513.

[88] G. E. Blonder, M. Tinkham, and T. M. Klapwijk. Transition from metallic to tunneling regimes in superconducting microconstrictions: Excess current, charge imbalance, and supercurrent conversion. *Phys. Rev. B*, 25(7):4515–4532, April 1982. https://link.aps.org/doi/10.1103/PhysRevB.25.4515.

[89] Leonid P. Rokhinson, Xinyu Liu, and Jacek K. Furdyna. The fractional a.c. Josephson effect in a semiconductor–superconductor nanowire as a signature of Majorana particles. *Nature Phys*, 8(11):795–799, November 2012. http://www.nature.com/articles/nphys2429.

[90] Yi-Hua Lai, Sankar Das Sarma, and Jay D. Sau. Quality factor for zero-bias conductance peaks in Majorana nanowire. *arXiv:2111.01178 [cond-mat]*, November 2021. http://arxiv.org/abs/2111.01178.

[91] S. M. Albrecht, A. P. Higginbotham, M. Madsen, F. Kuemmeth, T. S. Jespersen, J. Nygård, P. Krogstrup, and C. M. Marcus. Exponential protection of zero modes in Majorana islands. *Nature*, 531(7593):206–209, March 2016. http://www.nature.com/articles/nature17162.

[92] C. W. J. Beenakker. Theory of Coulomb-blockade oscillations in the conductance of a quantum dot. *Phys. Rev. B*, 44(4):1646–1656, July 1991. https://link.aps.org/doi/10.1103/PhysRevB.44.1646.

[93] Yi-Hua Lai, Sankar Das Sarma, and Jay D. Sau. Theory of Coulomb blockaded transport in realistic Majorana nanowires. *Phys. Rev. B*, 104(8):085403, August 2021. https://link.aps.org/doi/10.1103/PhysRevB.104.085403.

[94] Haining Pan, William S. Cole, Jay D. Sau, and S. Das Sarma. Generic quantized zero-bias conductance peaks in superconductor-semiconductor hybrid structures. *Phys. Rev. B*, 101(2):024506, January 2020. https://link.aps.org/doi/10.1103/PhysRevB.101.024506.

[95] Sankar Das Sarma and Haining Pan. Disorder-induced zero-bias peaks in Majorana nanowires. *Phys. Rev. B*, 103(19):195158, May 2021. https://link.aps.org/doi/10.1103/PhysRevB.103.195158.

[96] Haining Pan and Sankar Das Sarma. Crossover between trivial zero modes in Majorana nanowires. *Phys. Rev. B*, 104(5):054510, August 2021. https://link.aps.org/doi/10.1103/PhysRevB.104.054510.

[97] Haining Pan and Sankar Das Sarma. On-demand large-conductance in trivial zero-bias tunneling peaks in Majorana nanowires. *arXiv:2110.07536 [cond-mat]*, October 2021. http://arxiv.org/abs/2110.07536.

[98] Yu A. Bychkov and E. I. Rashba. Oscillatory effects and the magnetic susceptibility of carriers in inversion layers. *J. Phys. C: Solid State Phys.*, 17(33):6039–6045, November 1984. https://doi.org/10.1088/0022-3719/17/33/015.

[99] Tudor D. Stanescu, Jay D. Sau, Roman M. Lutchyn, and S. Das Sarma. Proximity effect at the superconductor–topological insulator interface. *Phys. Rev. B*, 81(24):241310, June 2010. https://link.aps.org/doi/10.1103/PhysRevB.81.241310.

[100] Jay D. Sau, Roman M. Lutchyn, Sumanta Tewari, and S. Das Sarma. Robustness of Majorana fermions in proximity-induced superconductors. *Phys. Rev. B*, 82(9):094522, September 2010. https://link.aps.org/doi/10.1103/PhysRevB.82.094522.

[101] S. Das Sarma, Amit Nag, and Jay D. Sau. How to infer non-Abelian statistics and topological visibility from tunneling conductance properties of realistic Majorana nanowires. *Phys. Rev. B*, 94(3):035143, July 2016. https://link.aps.org/doi/10.1103/PhysRevB.94.035143.

[102] Seongjin Ahn, Haining Pan, Benjamin Woods, Tudor D. Stanescu, and Sankar Das Sarma. Estimating disorder and its adverse effects in semiconductor Majorana nanowires. *Phys. Rev. Materials*, 5(12):124602, December 2021. https://link.aps.org/doi/10.1103/PhysRevMaterials.5.124602.

[103] Christoph W. Groth, Michael Wimmer, Anton R. Akhmerov, and Xavier Waintal. Kwant: A software package for quantum transport. *New J. Phys.*, 16(6):063065, 2014. http://stacks.iop.org/1367-2630/16/i=6/a=063065.

[104] Tudor D. Stanescu and Sumanta Tewari. Robust low-energy Andreev bound states in semiconductor-superconductor structures: Importance of partial separation of component Majorana bound states. *Phys. Rev. B*, 100(15):155429, October 2019. https://link.aps.org/doi/10.1103/PhysRevB.100.155429.

[105] I. C. Fulga, F. Hassler, and A. R. Akhmerov. Scattering theory of topological insulators and superconductors. *Phys. Rev. B*, 85(16):165409, April 2012. https://link.aps.org/doi/10.1103/PhysRevB.85.165409.

[106] Hongyu Tian and Chongdan Ren. Distinguishing Majorana and quasi-Majorana bound states in a hybrid superconductor-semiconductor nanowire with inhomogeneous potential barriers. *Results in Physics*, 26:104273, July 2021. https://www.sciencedirect.com/science/article/pii/S2211379721004101.

[107] Shiyu Zhu, Lingyuan Kong, Lu Cao, Hui Chen, Michał Papaj, Shixuan Du, Yuqing Xing, Wenyao Liu, Dongfei Wang, Chengmin Shen, Fazhi Yang, John Schneeloch, Ruidan Zhong, Genda Gu, Liang Fu, Yu-Yang Zhang, Hong Ding, and Hong-Jun Gao. Nearly quantized conductance plateau of vortex zero mode in an iron-based superconductor. *Science*, 367(6474):189–192, January 2020. http://www.science.org/doi/full/10.1126/science.aax0274.

[108] İ. Adagideli, M. Wimmer, and A. Teker. Effects of electron scattering on the topological properties of nanowires: Majorana fermions from disorder and superlattices. *Phys. Rev. B*, 89(14):144506, April 2014. https://link.aps.org/doi/10.1103/PhysRevB.89.144506.

[109] David M. T. van Zanten, Deividas Sabonis, Judith Suter, Jukka I. Väyrynen, Torsten Karzig, Dmitry I. Pikulin, Eoin C. T. O'Farrell, Davydas Razmadze, Karl D. Petersson, Peter Krogstrup, and Charles M. Marcus. Photon-assisted tunnelling of zero modes in a Majorana wire. *Nat. Phys.*, 16(6):663–668, June 2020. https://www.nature.com/articles/s41567-020-0858-0.

[110] F. Setiawan, Chun-Xiao Liu, Jay D. Sau, and S. Das Sarma. Electron temperature and tunnel coupling dependence of zero-bias and almost-zero-bias conductance peaks in Majorana nanowires. *Phys. Rev. B*, 96(18):184520, November 2017. https://link.aps.org/doi/10.1103/PhysRevB.96.184520.

[111] Fanming Qu, Jasper van Veen, Folkert K. de Vries, Arjan J. A. Beukman, Michael Wimmer, Wei Yi, Andrey A. Kiselev, Binh-Minh Nguyen, Marko Sokolich, Michael J. Manfra, Fabrizio Nichele, Charles M. Marcus, and Leo P. Kouwenhoven. Quantized Conductance and Large g-Factor Anisotropy in InSb Quantum Point Contacts. *Nano Lett.*, 16(12):7509–7513, December 2016. https://doi.org/10.1021/acs.nanolett.6b03297.

[112] Ilse van Weperen, Sébastien R. Plissard, Erik P. A. M. Bakkers, Sergey M. Frolov, and Leo P. Kouwenhoven. Quantized Conductance in an InSb Nanowire. *Nano Lett.*, 13(2):387–391, February 2013. https://doi.org/10.1021/nl3035256.

[113] Jie Shen, Sebastian Heedt, Francesco Borsoi, Bernard van Heck, Sasa Gazibegovic, Roy L. M. Op het Veld, Diana Car, John A. Logan, Mihir Pendharkar, Senja J. J. Ramakers, Guanzhong Wang, Di Xu, Daniël Bouman, Attila Geresdi, Chris J. Palmstrøm, Erik P. A. M. Bakkers, and Leo P. Kouwenhoven. Parity transitions in the superconducting ground state of hybrid InSb–Al Coulomb islands. *Nature Communications*, 9(1):4801, November 2018. http://www.nature.com/articles/s41467-018-07279-7.

[114] S. Vaitiekėnas, G. W. Winkler, B. van Heck, T. Karzig, M.-T. Deng, K. Flensberg, L. I. Glazman, C. Nayak, P. Krogstrup, R. M. Lutchyn, and C. M. Marcus. Flux-induced topological superconductivity in full-shell nanowires. *Science*, 367(6485), March 2020. http://science.sciencemag.org/content/367/6485/eaav3392.

[115] B. van Heck, R. M. Lutchyn, and L. I. Glazman. Conductance of a proximitized nanowire in the Coulomb blockade regime. *Phys. Rev. B*, 93(23):235431, June 2016. https://link.aps.org/doi/10.1103/PhysRevB.93.235431.

[116] Ching-Kai Chiu, Jay D. Sau, and S. Das Sarma. Conductance of a superconducting Coulomb-blockaded Majorana nanowire. *Phys. Rev. B*, 96(5):054504, August 2017. https://link.aps.org/doi/10.1103/PhysRevB.96.054504.

[117] Yingyi Huang, Jay D. Sau, Tudor D. Stanescu, and S. Das Sarma. Quasiparticle gaps in multiprobe Majorana nanowires. *Phys. Rev. B*, 98(22):224512, December 2018. https://link.aps.org/doi/10.1103/PhysRevB.98.224512.

[118] B. Béri and N. R. Cooper. Topological Kondo Effect with Majorana Fermions. *Phys. Rev. Lett.*, 109(15):156803, October 2012. https://link.aps.org/doi/10.1103/PhysRevLett.109.156803.

[119] A. Altland, B. Béri, R. Egger, and A. M. Tsvelik. Multichannel Kondo Impurity Dynamics in a Majorana Device. *Phys. Rev. Lett.*, 113(7):076401, August 2014. https://link.aps.org/doi/10.1103/PhysRevLett.113.076401.

[120] Meng Cheng, Michael Becker, Bela Bauer, and Roman M. Lutchyn. Interplay between Kondo and Majorana Interactions in Quantum Dots. *Phys. Rev. X*, 4(3):031051, September 2014. https://link.aps.org/doi/10.1103/PhysRevX.4.031051.

[121] Zhi-qiang Bao and Fan Zhang. Topological Majorana Two-Channel Kondo Effect. *Phys. Rev. Lett.*, 119(18):187701, October 2017. https://link.aps.org/doi/10.1103/PhysRevLett.119.187701.

[122] Karen Michaeli, L. Aviad Landau, Eran Sela, and Liang Fu. Electron teleportation and statistical transmutation in multiterminal Majorana islands. *Phys. Rev. B*, 96(20):205403, November 2017. https://link.aps.org/doi/10.1103/PhysRevB.96.205403.

[123] P. Krogstrup, N. L. B. Ziino, W. Chang, S. M. Albrecht, M. H. Madsen, E. Johnson, J. Nygård, C. M. Marcus, and T. S. Jespersen. Epitaxy of semiconductor–superconductor nanowires. *Nature Materials*, 14(4):400–406, April 2015. http://www.nature.com/articles/nmat4176.

[124] Chun-Xiao Liu, Jay D. Sau, and S. Das Sarma. Distinguishing topological Majorana bound states from trivial Andreev bound states: Proposed tests through differential tunneling conductance spectroscopy. *Phys. Rev. B*, 97(21):214502, June 2018. https://link.aps.org/doi/10.1103/PhysRevB.97.214502.

[125] Krishnanand Mallayya, Marcos Rigol, and Wojciech De Roeck. Prethermalization and Thermalization in Isolated Quantum Systems. *Phys. Rev. X*, 9(2):021027, May 2019. https://link.aps.org/doi/10.1103/PhysRevX.9.021027.

[126] Yigal Meir and Ned S. Wingreen. Landauer formula for the current through an interacting electron region. *Phys. Rev. Lett.*, 68(16):2512–2515, April 1992. https://link.aps.org/doi/10.1103/PhysRevLett.68.2512.

[127] I. L. Aleiner, P. W. Brouwer, and L. I. Glazman. Quantum effects in Coulomb blockade. *Physics Reports*, 358(5):309–440, March 2002. http://www.sciencedirect.com/science/article/pii/S0370157301000631.

[128] C. W. J. Beenakker. Quantum transport in semiconductor-superconductor microjunctions. *Phys. Rev. B*, 46(19):12841–12844, November 1992. https://link.aps.org/doi/10.1103/PhysRevB.46.12841.

[129] Jay D. Sau, Brian Swingle, and Sumanta Tewari. Proposal to probe quantum nonlocality of Majorana fermions in tunneling experiments. *Phys. Rev. B*, 92(2):020511, July 2015. https://link.aps.org/doi/10.1103/PhysRevB.92.020511.

[130] Leo P. Kouwenhoven, Charles M. Marcus, Paul L. McEuen, Seigo Tarucha, Robert M. Westervelt, and Ned S. Wingreen. Electron Transport in Quantum Dots. In Lydia L. Sohn, Leo P. Kouwenhoven, and Gerd Schön, editors, *Mesoscopic Electron Transport*, NATO ASI Series, pages 105–214. Springer Netherlands, Dordrecht, 1997. https://doi.org/10.1007/978-94-015-8839-3_4.

[131] J. H. F. Scott-Thomas, Stuart B. Field, M. A. Kastner, Henry I. Smith, and D. A. Antoniadis. Conductance Oscillations Periodic in the Density of a One-Dimensional Electron Gas. *Phys. Rev. Lett.*, 62(5):583–586, January 1989. https://link.aps.org/doi/10.1103/PhysRevLett.62.583.

[132] H. van Houten and C. W. J. Beenakker. Comment on "Conductance oscillations periodic in the density of a one-dimensional electron gas". *Phys. Rev. Lett.*, 63(17):1893–1893, October 1989. https://link.aps.org/doi/10.1103/PhysRevLett.63.1893.

[133] L. I. Glazman and R. I. Shekhter. Coulomb oscillations of the conductance in a laterally confined heterostructure. *J. Phys.: Condens. Matter*, 1(33):5811–5815, August 1989. https://doi.org/10.1088/0953-8984/1/33/027.

[134] U. Meirav, M. A. Kastner, M. Heiblum, and S. J. Wind. One-dimensional electron gas in GaAs: Periodic conductance oscillations as a function of density. *Phys. Rev. B*, 40(8):5871–5874, September 1989. https://link.aps.org/doi/10.1103/PhysRevB.40.5871.

[135] U. Meirav, M. A. Kastner, and S. J. Wind. Single-electron charging and periodic conductance resonances in GaAs nanostructures. *Phys. Rev. Lett.*, 65(6):771–774, August 1990. https://link.aps.org/doi/10.1103/PhysRevLett.65.771.

[136] Meng Cheng, Roman M. Lutchyn, Victor Galitski, and S. Das Sarma. Splitting of Majorana-Fermion Modes due to Intervortex Tunneling in a ${p}_{x}+i{p}_{y}$ Superconductor. *Phys. Rev. Lett.*, 103(10):107001, August 2009. https://link.aps.org/doi/10.1103/PhysRevLett.103.107001.

[137] Yang Peng, Falko Pientka, Leonid I. Glazman, and Felix von Oppen. Strong Localization of Majorana End States in Chains of Magnetic Adatoms. *Phys. Rev. Lett.*, 114(10):106801, March 2015. https://link.aps.org/doi/10.1103/PhysRevLett.114.106801.

[138] So Takei, Benjamin M. Fregoso, Hoi-Yin Hui, Alejandro M. Lobos, and S. Das Sarma. Soft Superconducting Gap in Semiconductor Majorana Nanowires. *Phys. Rev.*

Lett., 110(18):186803, April 2013. https://link.aps.org/doi/10.1103/PhysRevLett.110.186803.

[139] A. P. Higginbotham, S. M. Albrecht, G. Kiršanskas, W. Chang, F. Kuemmeth, P. Krogstrup, T. S. Jespersen, J. Nygård, K. Flensberg, and C. M. Marcus. Parity lifetime of bound states in a proximitized semiconductor nanowire. *Nature Physics*, 11(12):1017–1021, December 2015. http://www.nature.com/articles/nphys3461.